

Exploring Π -conjugated carbon nanomaterials for biomedical applications

Prasad, Kenath Priyanka

2016

Prasad, K. P. (2016). Exploring Π -conjugated carbon nanomaterials for biomedical applications. Doctoral thesis, Nanyang Technological University, Singapore.

<https://hdl.handle.net/10356/69314>

<https://doi.org/10.32657/10356/69314>



**EXPLORING π -CONJUGATED CARBON
NANOMATERIALS FOR BIOMEDICAL
APPLICATIONS**

KENATH PRIYANKA PRASAD

SCHOOL OF CHEMICAL & BIOMEDICAL ENGINEERING

NANYANG TECHNOLOGICAL UNIVERSITY

2016

Exploring Π -Conjugated Carbon Nanomaterials for Biomedical Applications

KENATH PRIYANKA PRASAD

School of Chemical and Biomedical Engineering

A thesis submitted to Nanyang Technological University in partial fulfillment of the
requirements for the degree of Doctor of Philosophy

2016

Acknowledgements

This thesis is dedicated to my late grandfather, Kesavan Nair.

A culmination of my 4-year journey through graduate school, I'd like to take a moment to thank everyone who has been a part of shaping me into the person I am today.

I would like to begin with expressing my sincere gratitude to my supervisor Professor Chen Peng for his constant guidance, encouragement and support. Since the inception of my doctoral studies, he has provided me with invaluable advice, an independent research environment and supported me in all my endeavors to develop my potential. Outside of guiding me in developing my potential as a researcher, Prof Chen has been extremely supportive of my extracurricular endeavors in graduate student leadership and entrepreneurship.

Furthermore, I would like to extend my thanks to all my current and previous lab members for their constant advice, encouragement and assistance over the years. I am especially indebted to Dr. Chen Yun who helped me gain my footing when I first started my doctorate studies. He has been a constant source of invaluable counsel, and more importantly a friend since I began working with him. Additionally, I am also thankful to Dr. Than Aung, Dr. Mahasin Alam SK, Dr. Parimal Routh, Ms. Arundithi Ananthanarayanan, and many others from my research group for their help and advice on my research. More importantly, I am thankful for their friendship and all the fun times spent during work and after. I also extend my thanks to Associate Professor Kwok Kian Woon and Ms. Alison Ng for all their help and support during my tenure in the as a graduate student leader.

Most importantly, my heartfelt love, gratitude and sincere thanks to my family. Without them, my successes would have been incomplete. To my parents Hari and Prasanthi, the thanks I say would not be enough to show you my gratefulness. To my husband Kris, thank you for catching me all the times I stumbled over the last 4 years. To my grandparents, thank you for your limitless faith and belief in my capabilities.

Table of Contents

| | |
|--|-----------|
| Acknowledgements | 2 |
| Table of Contents | 3 |
| Summary | 6 |
| 1. Background and Overview | 9 |
| 1.1 Background | 9 |
| 1.2 Research Objectives | 11 |
| 1.3 Overview | 13 |
| 2. Literature Review | 15 |
| 2.1 Introduction | 15 |
| 2.2 Semiconducting Polymer Dots | 17 |
| 2.2.1 Conventional Inorganic QDs (Semiconductor Quantum Dots)..... | 17 |
| 2.2.2 A Conjugated Carbon Alternative: Semiconducting Polymer Dots..... | 17 |
| 2.2.3 Synthesis Strategies..... | 20 |
| 2.2.4 Functionalization Strategies | 25 |
| 2.2.5 Properties..... | 28 |
| 2.2.6 Biomedical Applications..... | 37 |
| 2.3 Carbon Nanotubes..... | 44 |
| 2.3.1 Properties..... | 44 |
| 2.3.2 Carbon Nanotubes in Enzymatic Biofuel Cells..... | 45 |
| 2.4 Graphene | 48 |
| 2.4.1 Synthesis of 3D Graphene..... | 49 |
| 2.4.2 Properties..... | 55 |
| 2.4.3 Biomedical Applications of 3D Graphene as Catalyst Support..... | 55 |
| 3. Polymer Dots Derived from Poly (3,4-Ethylenedioxythiophene) and their Applications for Optical Imaging and Sensing | 59 |
| 3.1 Materials & Methods | 60 |
| 3.1.1 Preparation of the fibrous PEDOT film | 60 |
| 3.1.2 Preparation of PEDOT-Pdots..... | 60 |
| 3.1.3 Characterization..... | 61 |
| 3.1.4 Cell imaging | 61 |
| 3.1.5 Cell Viability & Proliferation Assay..... | 62 |
| 3.1.6 Optical detection of Hg ²⁺ ions..... | 62 |
| 3.2 Results and Discussion | 62 |

| | | |
|-----------|---|------------|
| 3.2.1 | <i>Synthesis and Morphology of PEDOT-Pdots</i> | 63 |
| 3.2.2 | <i>Chemical Characterization</i> | 64 |
| 3.2.3 | <i>Optical Characterizations</i> | 66 |
| 3.2.4 | <i>Cellular imaging using PEDOT-Pdots</i> | 73 |
| 3.2.5 | <i>Optical detection of mercury ions (Hg²⁺) using PEDOT-Pdots</i> | 74 |
| 3.3 | <i>Conclusion</i> | 76 |
| 4. | Synthesis of Polymer Dots from Polythiophene for Imaging Endocytic Compartments in Live Cells | 78 |
| 4.1 | <i>Materials & Methods</i> | 79 |
| 4.1.1 | <i>Preparation of Polythiophene (pTh) film</i> | 79 |
| 4.1.2 | <i>Preparation of polymer dots (Pdots)</i> | 79 |
| 4.1.3 | <i>Characterization</i> | 80 |
| 4.1.4 | <i>Cell imaging</i> | 80 |
| 4.1.5 | <i>Viability Assay</i> | 81 |
| 4.1.6 | <i>Liposome Preparation</i> | 81 |
| 4.2 | <i>Results and Discussion</i> | 82 |
| 4.2.1 | <i>Synthesis and characterizations</i> | 82 |
| 4.2.2 | <i>pTh-Pdots for cellular imaging</i> | 89 |
| 4.3 | <i>Conclusion</i> | 93 |
| 5. | Polymer dots as Broad Spectrum Antibacterial agents | 94 |
| 5.1 | <i>Materials & Methods</i> | 95 |
| 5.1.1 | <i>Synthesis and Characterization of pTh-Pdots</i> | 95 |
| 5.1.2 | <i>Bacteria Inhibition Studies</i> | 95 |
| 5.1.3 | <i>Peroxidase Activity Studies</i> | 96 |
| 5.1.4 | <i>Viability Studies</i> | 96 |
| 5.1.5 | <i>FESEM Imaging</i> | 97 |
| 5.2 | <i>Results & Discussion</i> | 97 |
| 5.2.1 | <i>Anti-Bacterial Activity</i> | 97 |
| 5.2.2 | <i>pTh-Pdots as Peroxidase Mimics</i> | 100 |
| 5.2.3 | <i>Antibacterial Mechanism of pTh-Pdots</i> | 101 |
| 5.3 | <i>Conclusion</i> | 103 |
| 6. | Three-Dimensional Graphene - Carbon Nanotube Hybrid Bioelectrodes for High Performance Enzymatic Biofuel Cells | 104 |
| 6.1 | <i>Materials & Methods</i> | 105 |
| 6.1.1 | <i>Materials</i> | 105 |
| 6.1.2 | <i>Characterization and Measurements</i> | 106 |
| 6.1.3 | <i>Preparation of 3D Graphene Composite Electrodes</i> | 106 |

| | | |
|-------|---|------------|
| 6.1.4 | <i>Biofuel Cell Design</i> | 106 |
| 6.1.5 | <i>Biodesign Test</i> | 107 |
| 6.2 | Results and Discussion | 107 |
| 6.2.1 | <i>Material Characterization</i> | 108 |
| 6.2.2 | <i>Anodic Properties</i> | 110 |
| 6.2.3 | <i>Cathodic Properties</i> | 115 |
| 6.2.4 | <i>Enzymatic Biofuel Cell Performance</i> | 119 |
| 6.3 | Conclusion | 120 |
| 7. | Conclusions and Outlook | 122 |
| 7.1 | Conclusions..... | 122 |
| 7.2 | Outlook | 125 |
| | Appendix I – Publications | 129 |
| | Appendix II – Common Abbreviations | 130 |
| | Appendix III – Table of Figures | 131 |
| | REFERENCES | 136 |

Summary

In the changing landscape of nanobiotechnology and nanomedicine research, there has been a sharp increase in the different types and categories of nanostructured modalities available for diverse biomedical applications like fluorescent labeling, biosensing, therapeutics, enhancing biocatalyst performances and biomolecular detection. Tailoring π -conjugated materials such as semiconducting polymers and graphene generates novel carbon-based nanomaterials with customized physicochemical (e.g. optical, electrical, surface, electrochemical, mechanical and morphological) properties for these applications. Currently the field of conjugated carbon nanomaterials is in its infancy, and is filled with many challenges and opportunities. This thesis work aims to contribute to this field by engineering novel conjugated carbon-based nanomaterials with tailored properties for versatile applications in biomedicine.

Firstly, an electropolymerization-ultrasonication based facile and high-throughput synthesis strategy was conceived to synthesize polymer quantum dots from one-dimensional semiconducting polymers. Using this strategy polymer dots with small sizes, high brightness, tunable photoluminescence, excellent photostability and superb biocompatibility were derived from a non-fluorescent semiconducting polymer poly(3,4-ethylenedioxythiophene) (PEDOT). The developed strategy was easily modifiable and could be used to develop other polymer dots with versatile properties. The small sized, fluorescent PEDOT-Pdots showed good quantum yields ($\sim 13\%$) and were utilized as bioimaging probes and optical sensors for toxic metals. The PEDOT-Pdots were used to image early endosomes and demonstrated sensitive optical detection of toxic mercury (Hg^{2+}) ions with a detection limit of $0.87 \mu\text{M}$ (with $\text{S/N} = 3$) and the linear response upto $10 \mu\text{M}$.

Subsequently, the thus developed synthesis route was modified and used to tailor polymer dots with improved brightness and small sizes from another 1D semiconducting polymer, poly(2,2'-bithiophene). The synthesized pTh-Pdots were small, showed high brightness and demonstrated excellent biocompatibility. Furthermore, the pTh-Pdots were observed to demonstrate negative solvatochromism, and showed promise as robust cellular imaging fluorophores and trackers. They were subsequently utilized to label and differentiate early endosomes and lysosomes, due to their unique ability to fluoresce different colors in the two compartments. This additionally highlights their use for tracking the endocytic pathway.

Identifying new antibacterial alternatives is increasingly becoming more urgent. The aqueous suspensions of the amphiphilic pTh-Pdots were found to be potent antibacterial agents and showed promise as synthetic antibacterial alternatives. With low minimum inhibitory concentrations, the pTh-Pdots showed activity against both gram-negative bacteria (*E. coli* - 45 $\mu\text{g/ml}$, *P. aeruginosa* -100 $\mu\text{g/ml}$) and gram-positive bacteria (*S. aureus* - 60 $\mu\text{g/ml}$), including drug resistant strains. Additionally, they demonstrated excellent peroxidase mimicking activity resulting from their good electron transport property. Subsequently, through a synergistic use of their ability to disrupt bacterial membranes and mimic peroxidase, the pTh-Pdots demonstrated a dramatic increase in their antibacterial potency (MIC - 10 $\mu\text{g/ml}$) against both gram-positive and gram-negative strains. To the best of our knowledge the antibacterial ability of polymer dots was studied for the first time in this work.

The last segment of this work further utilizes the synergistic effect between two π -conjugated carbon allotropes to enhance the performance properties of an alternative bio-power device for power generation (biofuel cells) for use in implantable medical devices. A one-dimensional (1D) π -conjugated carbon allotrope, single walled carbon nanotubes (SWCNT) were composited with freestanding graphene (a three-

dimensional architecture of 2D graphene) to fabricate bioelectrodes for a glucose/O₂ powered enzymatic biofuel cell (EBFC). The novel 3D graphene-SWCNT-enzyme based bio-electrodes demonstrated a synergistic integration between two conjugated carbon allotropes (graphene and carbon nanotubes), to enhance a bio-power device performance to new limits. With the highest performance till date due to extensive electrochemically active surface areas, excellent anchoring of enzymes by SWCNTs, efficient direct electron transfer and superb conductivity, the EBFC approached the theoretical open circuit voltage limit at 1.2 V and showed superb power densities at $2.27 \pm 0.11 \text{ mW cm}^{-2}$.

Chapter 1

1. Background and Overview

1.1 Background

An increase in availability of advanced healthcare has seen an overall improvement in the average lifespan of an individual. However, the world of today has conversely seen a sharp rise in the severity and incidence of medical problems, wherein diseases like cancer have been projected to be the leading cause of deaths in the future.¹ With an increase in occurrence of life threatening conditions such as cancer, multiple drug resistant microbial infections, heart attacks, toxic metal poisoning the need and urgency for managing these conditions has concurrently risen. While impressive work and biomedical advancements such as organic fluorophores for imaging cancer cells, multidrug treatments for infections, chemical sensors and pacemakers have been developed over the past decades, with their increased use several concerns have been recognized.

For example, conventional organic fluorophores suffer from rapid photobleaching, which makes long-term imaging and tracking extremely difficult.² This makes monitoring biological processes and detecting cancerous cells highly challenging. Similarly, whilst antibiotic combinations are popular solutions against microbial infections, an increase in the expression of multiple drug resistance has resulted in the rising ineffectiveness of these drugs.³ Additionally, increasing drug dosages intermittently for treatment adversely affects the patients. Furthermore, whilst pacemakers are one of the most important biomedical devices in recent history, like any other device they require batteries with functioning.⁴ However, batteries possess a finite life. This translates into replacing the device via surgical routes once the battery

lifetime expires, which is expensive. This can also be highly invasive and challenging for elderly users. The urgent need of the hour is to find and investigate alternative materials/technology to overcome these challenges.

Current advances in nanotechnology have led to nanomaterials being recognized as promising candidates for diverse biomedical applications. Semiconductor quantum dots (semi-QDs) have been developed in the past decades and have seen increasing applications as alternative fluorescent reporters, optical sensors, energy generators, super-capacitors, fuel cells and other biomedical applications.⁵⁻⁸ However with their rising prominence as biomedical agents, several innate limitations, including heavy metal ion leaching induced toxicity, significant blinking which induces intermittent signal loss during tracking, bulky sizes which result in steric hindrances, tendency to form non-specific physiological clusters reduces their desirability for biomedical applications.

The need to develop alternative nanomaterials that can overcome these disadvantages has spurred researchers to look towards alternate sources. π -Conjugated carbon based nanomaterials have garnered interest due to several factors including the high abundance of carbon and its self-bonding ability⁹/ catenation properties¹⁰ leading to versatile organic structures like semiconducting polymers, carbon nanotubes and graphene. Furthermore, carbon being a primary building block in humans makes it relatively simpler for its derivatives to assuage biocompatibility concerns. As a result they exhibit unique characteristics that include high conductivity, tunable bandgap, high photostability, superb biocompatibility, mechanical strength and immense surface area, making them highly desirable for versatile applications.¹¹ Effective utilization of these π -conjugated nanostructures requires the development of high-throughput strategies and properties for desirable applications. Currently the field of π -conjugated carbon nanomaterials is in its infancy and filled with abundant opportunities. This

thesis work attempts to contribute to the growing field of conjugated carbon nanomaterials by developing nanomaterials and nanocomposites for applications in imaging, therapeutics and biomedical devices.

1.2 Research Objectives

The aim behind this work is to conceive sustainable strategies to develop and utilize π -conjugated semiconducting polymeric nanostructures for imaging and therapeutic applications. Following development of a general synthesis strategy to produce nanostructures with customizable physicochemical/surface properties, we explore their suitability for intracellular live cell imaging, fluorescent sensing and therapeutic applications. Present day biomedical applications are not just constrained to diagnostics, sensing and therapeutics. Active implantable medical devices like cochlear implants, pacemakers are biomedical devices that require power sources such as batteries. But the existing power-sources suffer from limited lifetime. Fabrication of bioelectrodes using π -conjugated carbon nanocomposites is an alternative strategy, to develop power sources with enhanced properties capable of using physiological sugars as fuels. Theoretically in an implantable setting such devices would translate into self-sustained power sources for lifelong use.

Specific objectives:

- I. To design a general bottom-up strategy for the synthesis of polymer quantum dots from a π -conjugated carbon nanomaterials.**

This aim pertains the development of a general and facile synthesis strategy for polymer quantum dots (or polymer dots) from linear 1D semiconducting polymers. A simple, facile and easily modifiable electropolymerization - ultrasonication based synthesis strategy is developed to synthesize fluorescent polymer quantum dots from

an intrinsically non-fluorescent semiconducting polythiophene poly (3,4-ethylenedioxythiophene) (PEDOT). Subsequently, the physical, chemical, optical and biocompatibility properties of the synthesized polymer dots are studied. Theoretical simulations are conducted to elucidate the absorption and fluorescence emission mechanisms of the synthesized 0D polymeric nanostructures.

II. To perform live cell imaging applications using the fluorescence behavior of the electrochemically synthesized polymer dots.

This objective pertains to the study and application of the fluorescence properties of the synthesized polymer dots for optical applications in biology. Utilizing their fluorescence properties, PEDOT-Pdots developed in Chapter 3 are used as photostable, biocompatible and specific fluorescent reporters for cellular imaging applications. Furthermore by virtue of their optical properties and specificity, the polymer dots are developed into sensitive optical sensors for the detection of toxic mercury ions. Subsequently, the synthesis strategy is modified to increase the yield and brightness and develop a new type of polymer dots derived from Poly (2,2'-bithiophene) (pTh-Pdots). Following various characterizations studies, these polymer dots are also investigated for their intracellular live cell imaging behavior. Detailed studies are conducted to further elucidate their cellular imaging mechanism.

III. To investigate the efficacy of polymer dots as therapeutics.

This segment pertains to the exploration of new biomedical applications for the versatile polymer dots. The pTh-Pdots developed in Chapter 4 are investigated for therapeutic abilities, wherein their potential as antibacterial agents is realized for the first time. Studies are conducted to probe the antibacterial activities of the polymer dots against both gram (+) and gram (-) bacterial strains, including drug resistant bacteria. The minimum inhibitory concentrations against the different bacteria are

calculated. Subsequent investigations reveal the peroxidase mimicking behavior of the polymer dots. The behavior is subsequently utilized to improve their potency as antibacterial agents against strong bacterial strains like *Bacillus subtilis*. Studies are conducted to elucidate the killing mechanism of the polymer dots.

IV. To induce a synergistic interaction between two π -conjugated carbon nanomaterials for enhancing the performance of an alternative biomedical power device.

This aim pertains to the tandem utilization of two π -conjugated carbon nanomaterials to enhance the performance of a bio-device for power generation from physiological fuels such as glucose. A synergistic association between single-walled carbon nanotubes (SWCNT) and freestanding graphene is demonstrated by the fabrication of novel 3D graphene-SWCNT-enzyme bioelectrodes. The fabricated hybrid electrodes are functionalized and utilized to fabricate enzymatic glucose based biofuel cells capable of generating power using glucose as a power source. The thus, fabricated biofuel cells are subsequently, tested for the open circuit voltage (E_{cell}^{ocv}), power output density and long-term stability. Subsequently, as a proof-of-concept study LEDs are lit up using the enzymatic biofuel fuel cell where glucose and oxygen, are utilized as the fuel and oxidizer, respectively.

1.3 Overview

In brief, Chapter 1 highlights the need for alternative materials in biology/biomedicine. The reason behind the exploration of π -conjugated carbon nanomaterials is established. Chapter 2 summarizes the current developments in this field of conjugated nanocarbons. Synthesis strategies, properties and biomedical applications of prominent π -conjugated carbon based nanostructures namely semiconducting polymer dots, carbon nanotubes and three-dimensional graphene are discussed in detail. In Chapter 3,

a high throughput and general strategy for the production of semiconducting polymer dots is discussed. Various characterization studies including theoretical studies are performed to understand their properties and mechanism. Their utility as a fluorophore reporter and optical turn-off sensors are further investigated. Chapter 4 aims to subsequently, improve and modify polymer dots for cell labeling and tracking applications. To this end, new polymer dots with unique properties are synthesized by modifying the previously developed strategy. A study to elucidate their imaging mechanism is performed. Following this, Chapter 5 explores new therapeutic applications by revealing the antimicrobial potential of polymer dots to develop new antibacterial agents. A detailed study on the antibacterial behavior of an embodiment of polymer dots developed in the previous chapter is followed by an investigation of their killing mechanism. In Chapter 6, two π -conjugated carbons are composited together to enhance the performance of a bio-power device used to generate power from a biofuel, glucose. Detailed characterization and performance studies are conducted, following which a light emitting diode is powered as a proof-of-concept demonstration for the biofuel cell. Chapter 7 summarizes the conclusions that contributed to this thesis and includes a brief discussion on the future outlook of π -conjugated carbons nanomaterials.

Chapter 2

2. Literature Review

2.1 Introduction

Carbon with atomic number 6 has six electrons, which occupy $1s^2$, $2s^2$, and $2p^2$ atomic orbitals and can hybridize in sp , sp^2 , or sp^3 forms.¹² The self-bonding or catenation property is predominantly unique to carbon, in that most other elements including silicon mostly experience strong steric effects which in turn prevents p-orbital overlaps.¹⁰ More importantly being an integral part of the human body, it is promising as a biocompatible element. Conjugated carbon nanomaterials form an important subclass of the carbon family consisting of sp^2 carbon bonded materials. Conjugated systems are structures containing overlapping p-orbitals, across interspersed sigma bonds that allows the pi-electrons across adjacent p-orbitals to be delocalized.¹³ These pi-electrons are shared by a group of atoms rather than belonging to a singular bond or atom. Some of the largest and most well known conjugated systems are those belonging to the conjugated carbon family such as semiconducting polymers, carbon nanotubes and graphene.¹³

Semiconducting polymers are linear 1D intrinsically conductive polymerized systems which, contain large π -conjugated backbones and delocalized electronic structures.¹⁴ The delocalized π -electrons result in these polymers exhibiting high conductivities. Based on their species doping (p- or n-) these polymers using oxidation or reduction results them in exhibiting band gaps, which in turn allows for emission & absorption at the band edges, generating desirable optical properties.¹⁵ Furthermore, functionalizing and modifying their size-dependent properties results in polymeric nanostructures with

unique physicochemical properties,¹⁶ thereby increasing their attractiveness for fluorescence labeling, tracking and therapeutic applications.

Other than semiconducting polymers, carbon nanotubes and graphene are two other embodiments of the π -conjugated carbon family. Being carbon allotropes both exhibit several unique properties including excellent biocompatibility, high carrier mobility, high electron transfer rate, high robustness, and large electrochemically active area with outstanding structural and mechanical properties.¹⁷⁻²⁰ Furthermore, a three dimensional (3D) architecture of graphene demonstrates several intrinsic advantages whilst avoiding the disadvantages of its two dimensional (2D) counterpart. These critical electrochemical properties such as high surface area, efficient electrolyte transport, increased conductivities and good biocompatibility demonstrate the immense potential of π -conjugated carbons in electrochemical bio-power devices such as such as biosensors and biofuel cells.²¹

Doubtless, an extensive knowledge of the synthesis, physicochemical and surface properties of these conjugated carbons are of significant importance for designing low dimensional nanostructures for diverse biomedical use. Given a particular application, the design of the π -conjugated carbon nanostructure is significantly influenced by the precursors, synthesis technique, functionalization, structure dimensions, and substrate. The following sections will briefly discuss about the various existing strategies to develop π -conjugated semiconducting polymer quantum dots, their properties and various applications in biomedicine. The last sections of this chapter will briefly discuss the properties and enzymatic biofuel cell applications of two other π -conjugated carbon nanomaterials (carbon nanotubes and graphene) utilized for the final work in this thesis.

2.2 Semiconducting Polymer Dots

2.2.1 Conventional Inorganic QDs (Semiconductor Quantum Dots)

It is well known that decrease in size of a macroscopic structure to nanometer (nm) dimensions, results in the material in exhibiting several unique properties. Semiconductor quantum dots (Semi-QDs) have over the past decades, become one of the best-known tools in nanotechnology especially for of bio-imaging and optical sensing.²² Their versatile colors, broad absorption bands, narrow symmetric emissions, high brightness and photo-stability compared to conventional fluorescent dyes make them attractive for cellular applications. As a result, some of the very first alternatives to conventional fluorophores developed were semiconductor quantum dots (semi-QDs), with the term quantum dots being indicative of < 30 nm sized particles.²² Several well known semi-QDs utilized extensively for biological imaging and optical sensing include CdSe,²³ CdTe²⁴ and other semiconductor QDs. However these semi-QDs possess certain intrinsic drawbacks such as high toxicity^{24,25} blinking,²⁶ steric hindrance,²⁶ relatively high time and cost of synthesis, which make them undesirable for permanent long term use.

2.2.2 A Conjugated Carbon Alternative: Semiconducting Polymer Dots

Developing alternatives capable of overcoming the disadvantages posed by the conventional inorganic nanomaterials for biomedical applications is imperative. Carbons based nanomaterials on the other hand, are readily available, non-toxic, and customizable. The low dimensional conjugated nanocarbons form a broad category of nanometer-sized structures called the carbon dots that are primarily comprised of graphene quantum dots, carbon nano-dots and polymer dots.²⁷ By virtue of their

extensive variety of properties, these nanocarbons have been found as suitable replacements for conventional organic & inorganic nanomaterials. Of these carbon dots, polymer dots despite being in its infancy have been found to be superior to its counterparts. Unlike graphene quantum dots and carbon dots suffer from disadvantages like decreased brightness in their bare forms, the polymer dots showed numerous advantages including high brightness, lack of blinking and unique properties resulting from heteroatomic abundance.

Semiconducting polymers: They are a class of one-dimensional (1D) π -conjugated carbon polymers that possess delocalized π electrons along their backbone, resulting in versatile electronic and optical properties.^{13,26} Often called as semi-metals, they possess a high degree of conductivity. Several well known semiconducting polymers such as polythiophenes and polyanilines have been widely used in optical applications such as active materials in thin film transistors,²⁸ organic LEDs,²⁹ photovoltaics³⁰ and a variety of other optoelectronic devices. Specifically, polythiophenes have always been considered desirable for optical applications due to their ease of large-scale synthesis and outstanding properties. The intrinsically conductive nature of polythiophene allows them to possess a small electronic band-gap. Various synthesis and functionalization strategies can be used to widen these electronic band-gaps and generate interesting physical, chemical and optical properties for diverse biomedical applications.

The phenomenon of fluorescence usually involves the photo-excitation of an electron from the highest occupied energy band (π band) to the lowest unoccupied energy band (π^* band), thus forming an electron-hole pair. On returning to its normal state to recombine with the hole, a fluorescent photon at a lower energy is generated. The absorbed wavelength is determined by the π - π^* band gap, and is usually tunable by

altering the polymeric molecular structure,²⁶ creating edge defects, functionalizing, doping or twisting the polymeric backbone.^{24, 31-32}

With their wide spread use in diverse applications including chemical sensors, organic light emitting diodes, photo-voltaic and so forth, the preparation of semiconducting polymer nanoparticles/quantum dots for optoelectronic applications started garnering extensive interest.³³ More recently, the synthesis and application of these low-dimensional semiconducting polymeric nanostructures for diverse biomedical applications including diagnostics, cellular imaging and therapy has accumulated some scrutiny.^{26, 33} However, not much investigation has been carried out regarding synthesis strategies as well their versatility for different biomedical applications.

Semiconducting Polymer Nanoparticles/Dots: Due to lack of precise definitions, polymer nanoparticles (pNP) are defined as nanometer-sized entities (particle sizes < 100nm), representing separate discontinuous phases, which are always surrounded by continuous free flowing mediums such as water.²⁶ Colloidal pNPs are predominantly hydrophobic, but hydrophilic or amphiphilic polyelectrolytes can form these NPs as well. On the other hand polymer quantum dots (Pdots), are nanostructures with particle sizes < 30 nm (comparable to that of semi-QDs).³⁴ Some existing semiconducting polymer dots have been derived from polyfluorenes (such as PDHF and PFO;), polyphenylenes (such as PPE), polyphenylene vinylenes (such as MEH-PPV and CN-PPV). PFBT (poly(fluorene-alt-benzothiadiazole)), a heavily substituted polyfluorene derivative is another commonly favored polymer dot for biomedical applications. Polythiophenes (and their derivatives) are linear 1D intrinsically conductive polymerized thiophene systems that contain large π -conjugated backbones and delocalized electronic structures resulting in an intrinsically conductive nature.¹⁴ While they are classified as some of the most conductive polymers, there is a significant gap in the investigation for their potential as polymer dot materials.

A relatively new field of research there limited strategies for the synthesis of these 0D structures and limited research into their potential as biomedical agents. An urgent need of the moment is to develop alternative but simpler strategies of polymer dot synthesis, design new types of polymer dots and gain a deeper insight on their versatility.

2.2.3 Synthesis Strategies

Often many applications in biology/biomedicine such as biomolecule sensing or cellular imaging have size constraints on the nanoparticle diameters but may require high brightness or working concentrations. Larger sized nanoparticles may experience the effects of limited uptake due to crowded cellular locations, steric hindrances from biomolecules and so-forth. This highlights the need for the development of new facile methods for the synthesis of small sized pNPs or Pdots with high brightness and excellent biocompatibility. Present synthesis strategies for these 0D nanoparticles/dots either involve direct polymerization methods (NPs synthesized from low weight monomers) or post polymerization techniques (precursors are already synthesized high weight polymers).³³

I. Direct Polymerization

1. Chemical Polymerization

The chemical polymerization approach involves techniques such as oxidative polymerization, and coupling reactions catalyzed by transition metals in multiphase systems.³⁵ This technique lends a greater degree of control on size and properties of the Pdots, and is not limited by the solubility of polymers in organic solvents, a primary bottleneck for the post-polymerization based methods.

Drawbacks: On the other hand, some of the drawbacks suffered by chemical polymerization based strategies include:

- ❖ Tedious & long polymer synthesis,
- ❖ Extensive pre/post polymerization processes (e.g. monomer pre-functionalization, polymer purification etc.),
- ❖ Extensive expertise in organic synthesis (making this extremely user unfriendly).

2. Electrochemical Polymerization

In contrast, electrochemical polymerization is a relatively easier, simpler and faster technique, which is superior to chemical polymerization due to several reasons.³⁶

- ❖ High purity polymer films can be easily acquired after synthesis,
- ❖ Limited post-polymerization processing and purification,
- ❖ No pre-functionalization of the monomer required,
- ❖ The amount of monomer required is limited,
- ❖ Synthesis parameters can be easily adjusted to achieve appropriate conditions in a time-effective manner,
- ❖ The infrastructure requirements are limited,
- ❖ The polymer can be easily switched between its oxidized, reduced and neutral state depending on necessity.

While polymer dots and nanoparticles have not been directly prepared using this technique, several semiconducting polymers like polythiophenes and polyanilines have been oxidatively electro-polymerized to form stable, homogenous and regular films.³⁷⁻

³⁸ Easily polymerized, the structure and quality of the polythiophene films are dependent on the nature of the monomer and the polymerization condition. With a highly regular and modifiable backbone, polythiophene and its derivatives can be promising candidates for a new generation of polymer dots. As a result of these advantages we make use of an electropolymerization-based approach using polythiophenes in this work.

II. Post-Polymerization Methods

The post polymerization technique is more simplistic by comparison. Capable of utilizing the commercially available polymers, this technique makes use of the mini-emulsion, re-precipitation, self-assembly and solvent exchange methods (Figure 2-1) for the synthesis of pNPs and Pdots. While the mini-emulsion/nano-precipitation techniques make use of hydrophobic polymer precursors (most commonly used for polymer dots synthesis), the self-assembly/solvent exchange techniques use hydrophilic polymers (commonly used for polymer nanoparticle synthesis).

1. Mini-emulsion

The preparation of pNPs and Pdots from emulsified droplet solutions using two opposing solutions (immiscible solvents) forms the heart of this technique. The two solutions containing a water immiscible solvent (containing the polymer) and water are initially mixed to form small sized droplets. The former is extracted subsequently; while strong shear forces are applied to the latter to form nanometer-sized particles. More often than not, a surfactant is used during preparation in order to preserve colloidal stability.³³ Landfester *et al.* used this method to develop fluorescent polymeric nanoparticles for use in light emitting devices (LEDs).³³ The particle size was found to be a factor of polymer concentration and surfactant nature. Particle sizes are usually within the diameter range of 40nm – 500nm.³⁹

2. Nano-precipitation:

Conversely, this procedure works using the miscibility of the solvent in water. Similar, to the mini-emulsion process this technique utilizes the polymer dissolved in an organic solution (water miscible) as the starting solution, following which it is rapidly injected into water under high shear stress. A sudden change (decrease) in solubility, combined with hydrophobic chain collapse of the polymer chains results in a suspension of highly fluorescent Pdots. First developed by Masuhara *et al.* to form 400

nm polythiophene pNPs, it was later modified by McNeill *et al.* to synthesize 5 – 30 nm Pdots.^{26, 39} This technique allows for particle size control by varying precursor polymer concentration. The resultant pNPs and Pdots are within 5 – 100 nm.

Drawbacks: However, both mini-emulsion and nano-precipitation suffer from several disadvantages.

- Dependence on initial polymer precursor concentration for controlling polymer dot sizes results in highly dilute polymer dot suspensions,
- Extremely low yield of polymer dots per cycle,
- Limited variety of commercially available fluorescent semiconducting polymers,
- Infrastructure expensive and sophisticated precursor polymer synthesis,
- Time-consuming precursor polymer purification and functionalization,
- Extensive functionalization required for synthesizing polymer dots with unique properties,
- Polymer dots are sometimes large in size, especially those from the mini-emulsion technique.

3. Self-Assembly:

The self-assembly method makes use of difference in charge between the conjugated polymers. Making use of electrostatic interactions, they are either dispersed in water or dissolved followed by mixing at specific ratios, followed by separation using high speed centrifugation. Antibacterial pNPs were prepared by this method, wherein the opposing charges between water-soluble polythiophene and cationic porphyrins (TPPN) were utilized⁴⁰. The pNPs usually had diameters in the range of ~100nm. The pNPs generated are usually large sized due to the hydrophilic nature of the precursors.

4. Solvent Exchange:

This technique is also utilized for the synthesis of pNPs and Pdots from exclusively hydrophilic precursors. pNPs between 10nm - 100nm can be prepared using a solvent exchange method, inclusive of sequential ultrafiltration. This method was applied for the preparation of acetic acid treated polymers.⁴¹⁻⁴³ Conjugated polyelectrolytes, being hydrophilic in nature can be synthesized using hyper-branched structures, to form 3D morphologies in water. The particle sizes here are dependent on segmental flexibility and generation number, which can result in uniform particle size distributions.⁴⁴

Drawbacks: However using hydrophilic polymers as precursors for the synthesis of Pdots/pNPs suffer several disadvantages which in turn make these synthesis protocols undesirable.²⁶

- Presence of heavily functionalized side-chains that lead to non-specific interactions,
- Lowered fluorescence quantum yields due to side chain modifications,
- Tedious synthesis & functionalization protocols,
- Increased difficulty in maintaining nanostructures morphology due to water-solubility resultant solvation & repulsive effects.

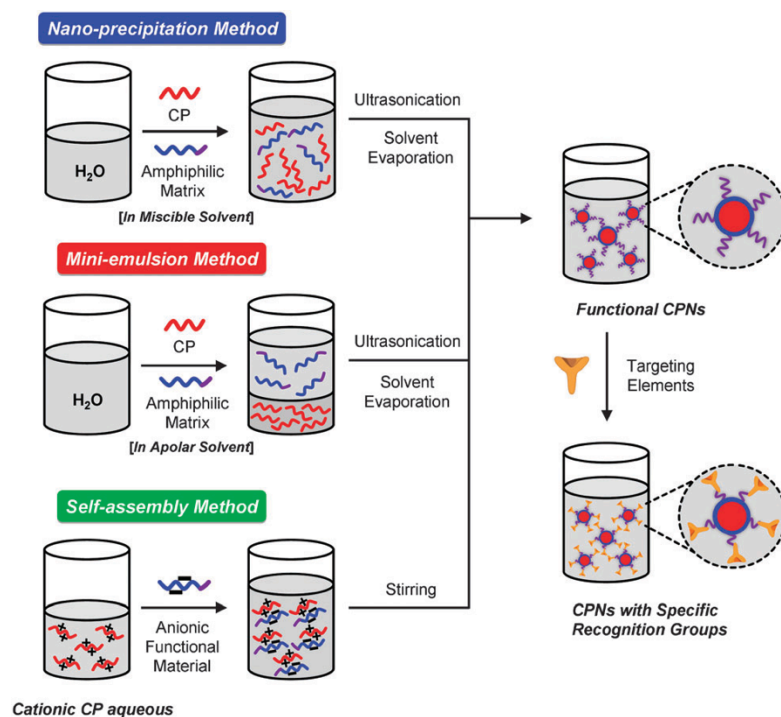


Figure 2-1: Schematic representation of various methods of preparation. Reproduced with permission from Reference ¹⁴. Copyright 2013, The Royal Society of Chemistry.

2.2.4 Functionalization Strategies

Modifying the surface chemistry is the first step in enabling the versatility of polymer dots/pNPs for various applications. As seen in Figure 2-2 functionalization is commonly done using encapsulation, co-precipitation of the nanoparticle or directly onto the precursor.

I. Encapsulation:

The encapsulation or embedding technique is one such method utilized for controlling the surface chemistry of these Pdots. The method makes use of materials such as silica, lipids and other moieties ^{45,46-47} to encapsulate the semiconducting polymer dots.

Drawbacks: While encapsulation with silica often results with a change of particle size by a few nm, coating materials like phospholipids invariably result in very large sizes (>100 nm). This restricts the use of these particles in majority of the size

sensitive biological applications, and only allows their use of size tolerant applications such as sensing and surface based antimicrobial applications.

II. Co-Precipitation:

Chiu *et al.* developed an alternative technique for functionalization involving amphiphilic polymers.⁴⁸ The technique works by co-precipitating functional groups bearing amphiphilic polymers alongside the semiconducting polymers to induce simultaneous integration of the functional group bearing polymer during particle formation itself. One such preparation made by the group involved an amphiphilic polystyrene polymer (PS-PEG-COOH), which was used to functionalize highly fluorescent PFBT Pdots.⁴⁹ Another study by the same group involved the co-precipitation of poly(styrene-co-maleic anhydride) (PSMA) besides PFBT to synthesize functionalized PFBT Pdots.⁵⁰

Drawbacks: The particle sizes in both the cases were ~15nm, indicating the particle size control that could be exhibited by this technique, however the throughput is extremely low. Additionally, this technique carries an inherent risk of possible functional group detachment due to dissociation.

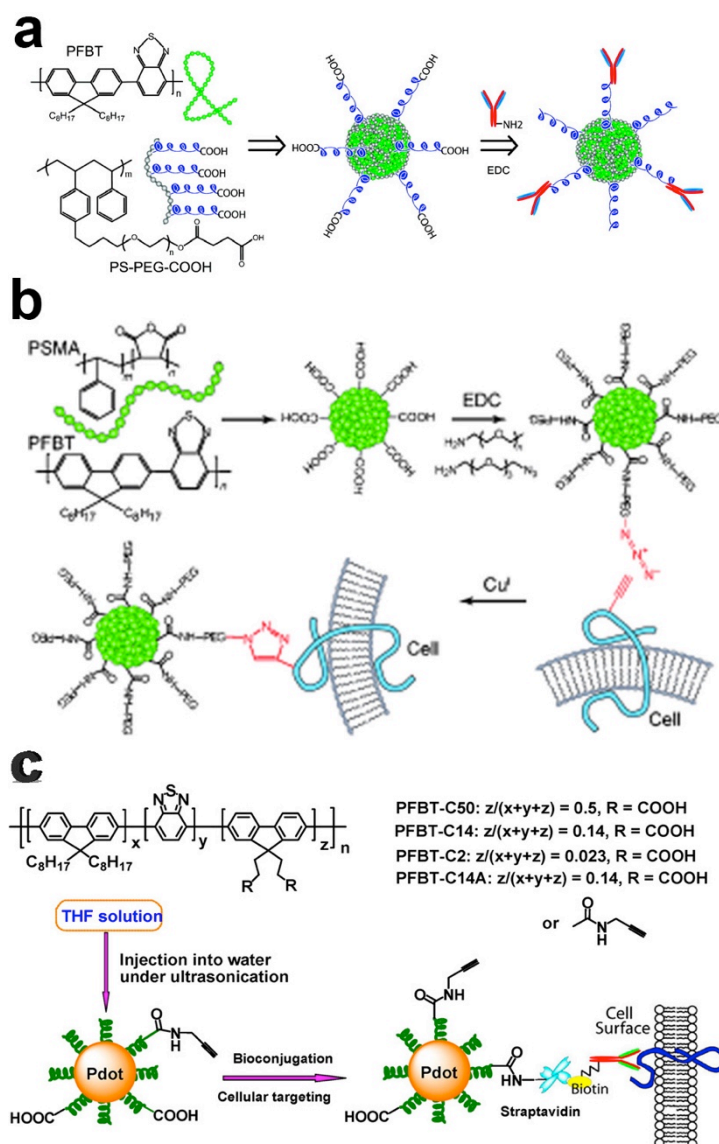


Figure 2-2: Functionalization using (a) Co-precipitation, Adapted with permission from Reference ⁴⁹. Copyright 2010, American Chemical Society (b) Click chemistry, Adapted with permission from Reference ⁵⁰, Copyright 2010, Wiley-VCH (c) Direct Functionalization, Adapted with permission from Reference ⁵¹, Copyright 2012, American Chemical Society

III. Direct Functionalization:

Another and infinitely simpler technique, simpler in many cases, is the direct attachment of relevant functional groups (e.g. Hydrophilic, proteins etc.) during the initial synthesis by covalent bonds, cross-linking chemistry, electrochemical functionalization etc.⁵¹ This technique doesn't have the inherent drawback of possible functional group detachment due to dissociation, as with the co-precipitation

technique. Additionally, Chiu *et al.* carried out a series of studies on PFBT Pdots with different molar fraction carboxyl side chains to study the dependence of low-density functional groups on the Pdot stability and fluorescence intensity.⁵¹ The same group also developed a cross linking strategy to form covalently linked functional molecules for direct functionalization of Pdots. Functional polymer poly(isobutylene-alt-maleic anhydride) (PIMA) or PSMA was used to cross link with the synthesized PFBT polymer via side-chain amine groups.⁵² The Pdots synthesized using this technique were 10 nm or less.

Drawbacks: Depending on this type of functionalization, based on covalent bond formation or cross-linking techniques may require a high degree of expertise in organic chemistry and is ultimately unfeasible in many cases due to complex synthesis requirements. In contrast, formation of non-covalent bonds during direct functionalization may be relatively simpler.

2.2.5 Properties

I. Physical Size and Morphology

Any biological utilization of Pdots is highly dependent on its physical characteristics such as their size and surface morphology. As discussed in the previous section the post-polymerization techniques result in particles of varying size distributions, ranging from 5 nm – 500 nm.^{26, 32-33}

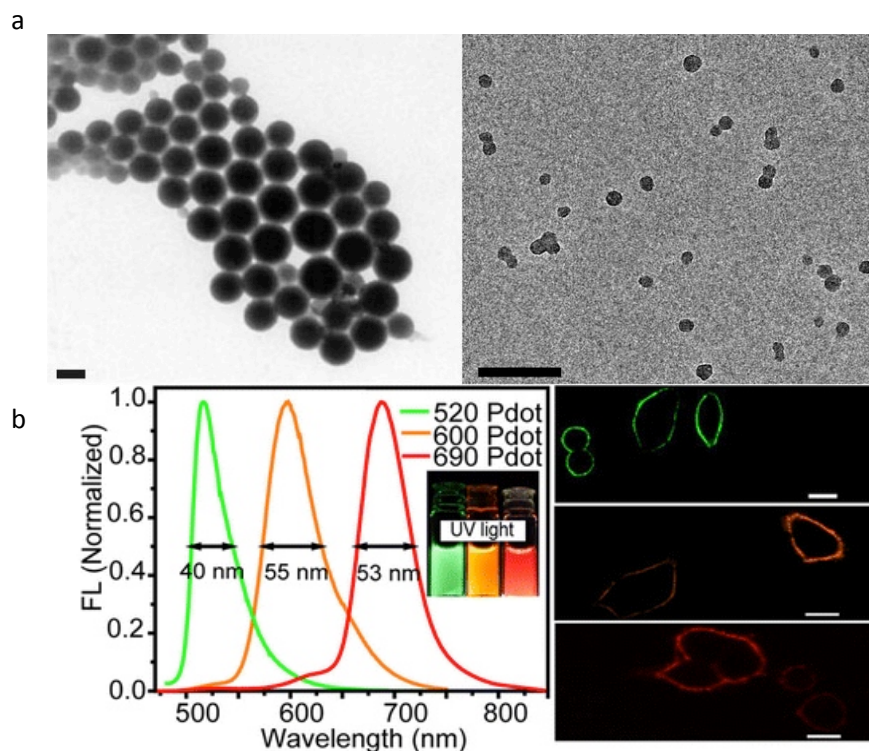


Figure 2-3: (a) TEM image of pNPs of poly (p-phenylene) prepared by microemulsion method and Pdots prepared from poly (fluorene) copolymer by nano-precipitation methods. Adapted with permission from Reference ^{26, 50, 53}, Copyright 2002, Wiley-VCH. Copyright 2010, Wiley-VCH. Copyright 2013, Wiley-VCH. (b) Multi-emission Pdots synthesized from different boron dipyrromethene (BODIPY) units, with (inset) showing absorption behavior - Confocal images of Pdots with MCF-7 cell. Adapted with permission from Reference ⁵⁴, Copyright 2013, American Chemical Society.

As shown in Figure 2-3a the mini-emulsion technique results in particle sizes of varying diameters upto 500 nm, while the Pdots synthesized from the nano-precipitation method are usually in the range of 5 nm – 50 nm. Varying polymer and surfactant concentrations in the starting solution controls the particle sizes and morphologies in the former, wherein extremely dilute polymeric concentrations resulted in smaller sized (~13 nm) Pdots.⁵⁵ The average size observed using mini-emulsion synthesis was seen to be ~75 nm to 250 nm, with the nanostructures being

surfactant stabilized.³³ The nano-precipitation method on the other hand results in smaller sized particle distributions, resultant from competing inter-chain and intra-chain collapse in a poor solvent.

The nanostructures form stable spherical suspensions in water. Investigation reveals the propensity of pNPs to collapse and form thermodynamically favorable spherical structures. This is most likely a result of strong hydrophobic interactions and large surface tension between the polymer chain and water.⁵⁶ The techniques result in densely packed, spherical shaped pNPs with high-energy transfer efficiency and is stabilized through electrostatic/steric interactions.³³

However a significant drawback with the post-polymerization methods is their dependence of precursor concentrations for size control. Using a highly concentrated precursor solution results in large sized pNPs. Masuhara *et al.* has reported nanoparticles ranging from 40 nm to 140 nm derived from a polymer poly(3-[2-(*N*-dodecylcarbamoyloxy)ethyl]thiophene-2,5-diyl), P3DDUT using these methods.⁵⁷ The pNPs formed are generally amorphous in nature, however some crystalline nanoparticles have also been reported. Both Landfester *et al.* and McNeill *et al.* have reported crystalline nanoparticles of polyanilines and polyfluorenes, respectively.⁵⁸⁻⁵⁹

II. Optical Properties

Studies have indicated superiority of Pdots over semiconductor quantum dots (Semi-QDs) of comparable sizes in terms of single particle and cell labeling brightness.⁴⁹ Extensive studies (of both nanostructures and bulk systems) have revealed the optical behavior of the Pdots to be strongly dependent on the chain conformations and the occurrence of aggregates of various types and sizes.³³ This behavior results from the intrinsic nature of the material wherein their conjugation lengths and particle distribution are influenced by inter- and intrachain interactions.³³ Additional factors

further influencing the conjugation lengths include its interaction with the surrounding environment such as additional compounds, solvents, and the preparation and intrinsic nature of the sample.³³

1. Absorption:

The Pdots very commonly exhibit a red or blue shifted absorption spectrum depending on their degrees of order in solution and their preparation conditions, with the highly ordered and crystalline structures exhibiting a red shifted spectrum. Nanoparticles synthesized using the post-polymerizations methods commonly exhibit broad, blue shifted absorption spectra with bands in the near-UV and visible range.³³ Attributable to the reduction in conjugation lengths due to kinks and twists as a consequence of the collapsed small size, the red shift remains linearly dependent on the size increase.⁶⁰ Furthermore, the Pdots usually contain multiple conformations with variable localized conformational changes that result in a commonly observed long red tail with an overall blue-shifted absorption spectrum.³³ Absorption studies reveal high absorption cross-section areas for single Pdot particles in the visible and near-UV ranges with high values in the range of 10^{-13} cm^2 . The reported values are considerably higher than Semi-QDs, and brighter than organic fluorphores.²⁶

2. Fluorescence:

The hydrophobic Pdots exhibit multicolor emissions (Figure 2-3b). Due to forces originally involved in their formation, the Pdots tend to exhibit red shifted fluorescence (PL) emission in organic solvents or good solvents.⁵⁷ This is particularly due to energy transfer to lower energy chromophores, with increasing chain interactions. An increase in the size has a linear effect on the red shift, with an approach towards the bulk material spectrum for sizes $> 10 \text{ nm}$ including nanoparticles of single layer thickness.^{26,60} Furthermore across all polymer dots, changes in the conjugation length due to bending, torsion or kinking along the polymer backbone

appear to be responsible for the modulation of most optical properties.⁴⁵

3. Two-Photon Emission:

Pdots interestingly possess good two-photon properties making them important for in multi-photon imaging applications. Absorption cross-section values upto 10^3 - 10^5 GM have been reported.⁶¹ Recently, using an alternative direct polymerization synthesis route Mecking *et al.* has reported >60 nm sized pNPs with high cross-sections of 10^7 GM.⁶² The reported two-photon absorption cross-sections are several orders higher than those of organic/semiconductor fluorophores of comparable size and volume. These properties become particular important in light of deep tissue or *in vivo* imaging applications wherein higher penetration and lesser background noise are critical.

4. Brightness:

Studies investigating the fluorescence brightness of the Pdot particles have revealed them to possess a remarkably degree of brightness as compared to both organic fluorophores and commercially available Semi-QDs. Chiu *et al.* synthesized Pdots derived from compositing PFBT and PF-DBT5 (red emitting polymers) that exhibited 15 times the brightness compared to a semi-qds.²⁶ The Pdots, especially those synthesized using the re-precipitation techniques form densely packed cores with high degrees of energy transfer and have reported a wide range of fluorescent quantum yields between 10 % - 70%.^{32, 63} Extensive studies have demonstrated a correlation between the decreasing quantum yields and increasing nanoparticles sizes.⁶⁴ The size dependence of the quantum yield has been correlated to the size dependent energy transfer efficiency to fluorescence quenching sites of the quantum dots.⁶⁴ This is more significant in terms of dye incorporation into quantum dots for enhanced energy transfer, however excessive dye amounts have been known to exhibit severe quenching behaviour.³³

5. *Fluorescence Lifetime & Photostability*

Time correlated single photon counting (TCSPC) studies have shown that the fluorescence lifetimes of the Pdots solutions range between 100ps to 1ns, with the values being dependent on the polymeric nature.⁶⁴ Further calculations conducted by Wu *et al.* revealed the fluorescence radiative rate constant values; a factor of quantum yield and fluorescence lifetime exhibited by Pdots to be between 10^7 - 10^9 s⁻¹.⁶⁴ With values comparable to those exhibited by organic fluorophores (10^8 s⁻¹), they show good potential as alternative fluorophores.²⁶ Furthermore, these parameters are generally critical for molecular imaging & real-time tracking studies.

The photostability of quantum dots or chromophores is characterized by the fluorescent quantum yield, which is defined as the number of molecules photo-bleached divided by the total number of photons absorbed over a given time interval. Extensive photobleaching kinetic studies performed to study the photostability of the Pdots indicate the photobleaching mechanism to be highly complex and not fully understood. While their mechanisms are not completely comparable to single dye molecules, studies speculate that these nanoparticles may possess longer triplet lifetimes due to hindered migrations across the backbone resulting in enhanced photostability.⁶⁵ Photobleaching quantum yields of typical chromophores (organic dyes) have been reported to be between 10^{-4} to 10^{-6} .⁶⁶ In comparison, Pdots demonstrate yields between 10^{-7} to 10^{-10} .^{26, 32, 49} These quantum yields were obtained from the rate constants obtained during photobleaching kinetics measurements. Several authors have demonstrated a lack of photobleaching by polymer dots over extended durations within biological systems making them good probes for cell imaging and tracking applications.³³

6. *Blinking*

Pdots were also observed to be superior to conventional fluorophores in terms of

blinking, with Pdots (>10nm) showing extremely steady fluorescence and the smaller (<10nm) Pdots being slightly dimmer or fluctuating in comparison.⁶⁷ The phenomenon of is attributed to a single photo-oxidation event, an irreversible change of the particle surface that induces a change in emission intensity whereby the extent of oxidation was dependent on the particle size.⁶⁰ The effect is significantly pronounced in smaller particles.⁶⁰ However, the amount of blinking was extremely insignificant compared to conventional dyes & semi-QDs, with both exhibiting pronounced blinking in extremely small timespans.⁶⁸ Furthermore, depending on their synthesis conditions and resultant chain conformations, the polymer nanoparticles have been known to behave as single photon sources.

III. Stability

Pdots show excellent colloidal stability without any aggregation upto months. Kee *et al.* speculated the formation of partially ionized defects due to oxidation during Pdots synthesis to be the reason for the excellent colloidal stability exhibited by Pdots in deionized water.⁶⁹ Supporting this Wu *et al.* demonstrated the possibility of induced minor chemical defects on the surface of Pdots during generation of hydrophilic properties as a cause for improved stability.²⁶ Additionally, surface modifications were shown to improve the colloidal stability of the Pdots as demonstrated by Chiu *et al.*⁵⁰⁻

51

For Pdots prepared using post-polymerization methods the particle stability is further dependent on the Pdots maintaining their structural integrity over time, i.e. since the formation is primarily driven by hydrophobic interactions, the presence of hydrophilic side chains causes differences in the association across the polymer backbone. However, the presence of hydrophilic side chains is a pre-requisite for water-solubility. Research by Chiu *et al.* indicates the possibility of decreasing the density of hydrophilic side chains, to increase particle stability.⁵¹ However, the side-chains still

allude to the possibility of formation of loose aggregates over long storage times. This clearly highlights the need of alternative preparation techniques to produce highly stable, yet non-bulky Pdots for biological applications

IV. Toxicity

Another key factor of consideration for biological applications is obviously the toxicity of the Pdots towards mammalian cells. While various π -conjugated semiconducting polymers have a history in tissue engineering as biomaterials,⁷⁰ as with any other nanomaterial the Pdots may exhibit different properties in the zero dimensional state. Thus, it is imperative to test the toxicity effects of the Pdots. Extensive research has shown the Pdots to possess extremely low degrees of cytotoxicity. Christensen *et al.* conducted several cytotoxicity studies on ~18nm PFBT Pdots on live J774A1 cells over 18 h and observed no discernible cytotoxic effects.⁶² Further studies performed on various cell lines by Moon *et al.* and others confirmed the non-toxic nature of the Pdots.^{47, 71}

| | Conventional Organic Fluorophore (Alexa 488) 26, a* | Conventional Inorganic Fluorophore (Qdot 565) 26, a* | PFBT Polymer Dots 26 |
|---|--|---|---------------------------------|
| Size | 1 nm | 15 nm | 10 nm |
| Toxicity | Highly Biocompatible | Contains Selenium | Biocompatible |
| Molar Absorptivity (M⁻¹ cm⁻¹) | 5.4 * 10 ⁴ | 2.9 * 10 ⁵ | 1.0 * 10 ⁷ |
| Quantum Yield | 0.9 | 0.3 - 0.5 | 0.3 – 0.6 |
| Fluorescence Lifetime (ns) | 4.2 | ~ 20 | 0.6 |
| Photostability | Poor Photostability | High photostability | High photostability |
| The data obtained are according to previously utilized specifications in Ref ²⁶ and a*. [a*- Data obtained from specifications of Alexa 488 & Qdot 565 provided by Invitrogen] | | | |

Table 2-1: Comparison between properties of conventional organic/inorganic fluorophores with semiconducting polymer dots

| Semiconductor Quantum Dots | | Semiconducting Polymer Dots | |
|---|---|--|---|
| Advantages | Disadvantages | Advantages | Disadvantages |
| Good Photostability | Toxic | High photo-stability | Low yield synthesis |
| Broad Absorption | Prone to aggregation in live cells | Chemically inert | Sometimes large sized polymer dots |
| Robust | Show extensive surface defects. | High brightness, tunable emission & high quantum yield | Sophisticated & expensive precursor polymer synthesis |
| Single light source for multiple color excitation | Poor clearance from the body | Heteroatom rich – results in unique properties | Extensive pre/post functionalization & purification |
| Bright & Tunable emission | Prone to steric hindrance following biomolecule functionalization | Biocompatible & good water solubility | Limited commercially available polymers |

Table 2-2: Comparison between conventional inorganic quantum dots and semiconducting polymer dots

2.2.6 Biomedical Applications

As mentioned previously the various merits of polymer nanoparticle (and polymer dots) including their extraordinary brightness, high surface area, tunable surface properties, immense photo-stability, adjustable bandgaps, low cytotoxicity, fast & stable emission rates makes them entirely suitable for a multitude of biological applications (Figure 2-3b and 2-4).

I. In Vitro Cellular Imaging:

It was observed that bare hydrophobic Pdots were stable in culture media, and preferred to undergo cellular uptake through cellular processes such as endocytosis.⁶⁴ Their high brightness and multiple fluorescence emissions allowed for their use for various *in vitro* imaging applications, such as labeling cells and organelles at extremely low working concentrations. Studies by Fernando *et al.* indicated the uptake of these Pdots to be dependent on macro-pinocytosis rather than clathrin or caveolin dependent cellular uptake mechanisms, with the final destination being the lysosomes.⁷² Liu *et al.* performed further studies, wherein Pdots loaded PLGA particles were incubated with MCF-7 cells. The studies indicated efficient endocytosis dependent cellular uptake, that was due to functionalization of the polymer dots with folic acid receptors.⁴⁷

Despite using Pdots as cellular probes for endocytic labeling, it is intrinsically non-specific. Chiu *et al.* conjugated immunoglobulin (IgG) & streptavidin to Pdots (diameter ~10-20 nm) to label a specific cellular marker EpCAM (epithelial cell surface marker) for detecting circulating tumor cells from live MCF-7²⁶ cells. The same group subsequently developed another set of bright orange Pdots ~10 nm diameter derived from CN-PPV, and conjugated it to streptavidin for specific labeling

of cell-surface markers and microtubule structures inside mammalian cells.⁶³ Fluorescent Pdots were modified by Chiu *et al.* using click chemistry with amino acids from metabolically labeled synthesized proteins, for *in vitro* cellular imaging using bio-orthogonal labeling. They were subsequently, utilized for the specific targeting and visualization of glycoproteins.⁵⁰

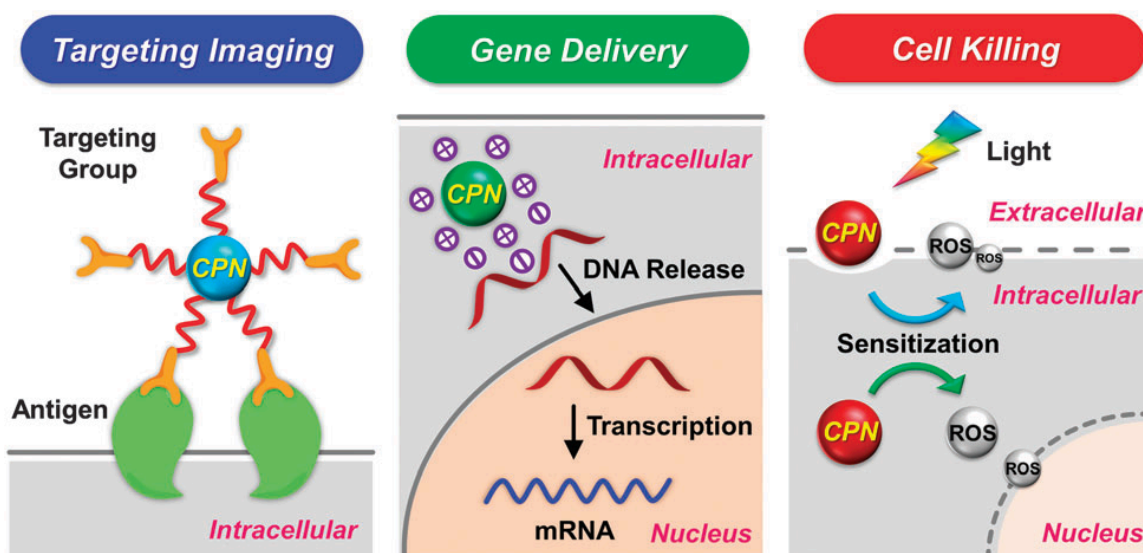


Figure 2-4: Schematic of various biological applications using conjugated polymer dots and nanoparticles. Reproduced with permission from Reference ¹⁴, Copyright 2013, The Royal Society of Chemistry.

II. In Vivo Imaging:

In vivo imaging becomes of great importance for imaging live models for various applications including tracking, therapy and diagnosis. Some major limitations for *in vivo* applications include tissue auto-fluorescence, limited penetrative depths of the visible range lasers, absorption and scattering. Using near-infrared (NIR) probes helps overcome some of these limitations, and the search for alternative stable nanomaterials capable of emitting in the NIR is ongoing. Pdots can be used as successful NIR probes for *in vivo* imaging as demonstrated by Kim *et al.* by their utilization of NIR emitting semiconducting polymer nanoparticles to map sentinel lymph nodes in mice.⁷³ The designed Pdots were cyanosubstitute derivatives of poly (p-phenylenevinylene), which

were synthesized using *in situ* colloidal polymerization. Bio-distribution studies indicated that the Pdots remained trapped within the lymph nodes, without escaping into the circulatory system over time.

Designing blood brain barrier (BBB) penetrating nanoparticles is a highly challenging task due multiple factors including size and surface property constraints. Chiu *et al.* developed *in vivo* tumor targeting Pdots having small diameters (~15nm), capable of binding to tumor specific peptide chlorotoxin after traversing the blood brain barrier.⁴⁸ Exhibiting a deep red emission the Pdot probes were used to target specific tumors in the brain of a transgenic mice model, ND2: SmoA1. Like other nanoparticles, the Pdots bio-distribution is dependent on the size and occurs primarily in the liver and spleen.⁷⁴

III. Particle Tracking:

Developing nanostructures capable of investigating cellular processes such as molecular transport, and motor proteins motions in real time is important.⁷⁵ Furthermore, tracking the movement of the nanostructured systems within the biological environment at real-time helps identify their behavior, action and efficacy within the system. McNeill *et al.* has investigated and developed a variety of Pdots capable of 2D/3D tracking using CCD equipped inverted fluorescence microscopes or video rate fluorescence microscopy.⁷⁶ Chiu *et al.* has conducted studies using Pdots as trackers to measure the motion of individual biomolecules and subcellular structures in a cell.²⁶

IV. Sensing:

With respect to sensing applications, conjugated polymers have widely garnered interest due to their high potential to form sensitive sensors as a result of efficient energy transfer, often characterized by extreme quenching.⁷⁷ Versatile Pdots based

sensors can be developed to sense changes in the testing environment such as optical sensors, temperature sensors, ionic sensors, FRET sensors and so forth. Hydrophobic Pdots represent a novel platform that exhibits energy transfer within its densely packed structure & high volume. Some Pdots have been incorporated with hydrophobic fluorescent dye molecules in order to build unique FRET based sensing systems. The intra-particle energy transfer between the donor polymer and acceptor dye results in environmental or analyte responsive emission changes.

Other bio-medically relevant sensors developed include Pdots doped with a phosphorescent dye platinum octaethylporphyrin (PtOEP) for oxygen sensing,⁷⁸ pH-sensitive polymer dot probes composed of a semiconducting polymer PPE and the pH-sensitive fluorescein dye,⁷⁹ and temperature-sensitive Pdots probes prepared using semiconducting polymers PFBT and PFPV alongwith a temperature-sensitive Rhodamine B (RhB) dye.⁸⁰ Similarly, Harbron *et al.* have developed photo-switchable Pdots based on photochromic dyes.⁸¹

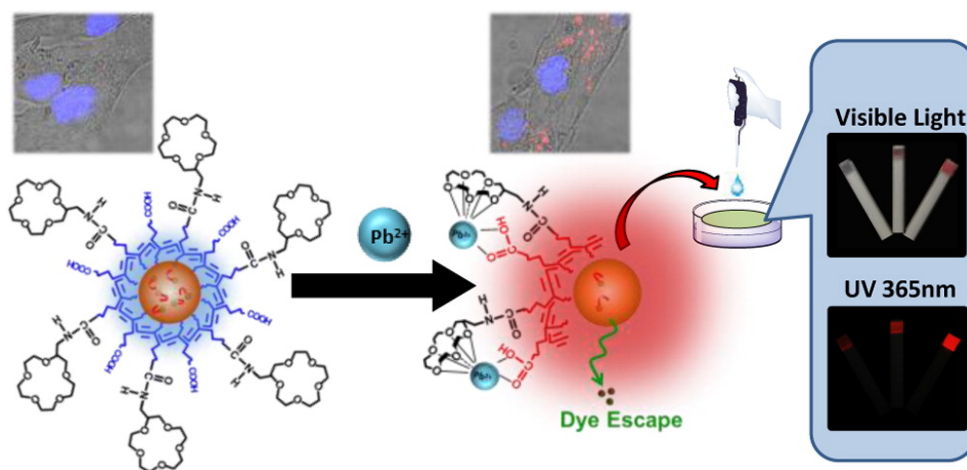


Figure 2-5: Dual Colorimetric and Fluorescent Sensor Based On Semiconducting Polymer Dots for Ratiometric Detection of Lead Ions in Living Cells. Reprinted with permission from Reference ⁸². Copyright 2015, American Chemical Society

Using nanoparticles to detect ions has always seen popularity due to their simple systems, selective nature, high sensitivity and reliable nature.⁸³ The nanoparticles predominantly undergo aggregation induced quenching (turn-off) or fluorescence 'turn-on' mechanisms in the presence of these ionic species. Various functionalized pNP based metal ion sensors for the detection of biologically relevant ionic species such as Cu^{2+} ,⁸⁴ Fe^{2+} , Pb^{2+} ⁸² (Figure 2-5) and Hg^{2+} ,⁸⁵ have been developed. Swager *et al.* designed a new type of energy transfer based 'turn-on' sensor for the biomolecules protease.⁸⁶

V. Drug and Gene Delivery:

The potential for utilizing pNPs/Pdots as drug delivery systems is immense due to their flexible polymer core (suitable for encapsulation), and intrinsic hydrophobic nature of the Pdots (functionalized to render water solubility). The latter property is particularly advantageous, since a significant number of anticancer drugs are poorly soluble in water. However, the amount of research done in this area is sparse. by Wang *et al* developed conjugated pNPs by electrostatically assembling a cationic conjugated fluorescent polymer PFO with a pre-doxorubicin (PG-Dox) conjugated anionic poly(l-glutamic acid) for targeting cancer cells.⁸⁷ Another system containing cisplatin loaded polyelectrolyte nanoparticles was developed by Liu *et al.* and used on nude mice for controlled intravenous drug release.²⁶ Additionally, some groups have researched into utilizing hydrophilic conjugated pNPs as gene delivery vehicles. While a lipid-modified cationic poly(fluorenylene phenylene) polymer (PFPL) has been utilized as a delivery vehicle for a green fluorescent protein (GFP) containing plasmid, another polymer comprising of hydrophilic PPEs has functioned as an small interfering RNA (siRNA) carrier.^{43, 88}

VI. Photodynamic and Photothermal Therapy:

Therapeutic applications such as photodynamic (PDT) or photo-thermal therapy (PTT) using nanoparticles are of considerable interest, due to increasing interest in non-invasive therapeutic alternatives to chemotherapy and surgery. Some strategies (Figure 2-6) developed using pNPs and Pdts as therapeutic alternatives include encapsulation of PDT dyes within the hydrophobic polymer matrix, conjugation of the dye on the surface or designing PDT/PTT inducing polymers.⁸⁹⁻⁹⁰ Huang *et al.* designed oxygen sensing phosphorescent conjugated polymer dots (Pdts) containing a photosensitizer Pt(II) porphyrin and demonstrated its use as a PDT agent on cancerous HepG2 cells.⁹¹ McNeill *et al.* on the other hand, developed Pdts doped with a singlet oxygen photosensitizer tetraphenylporphyrin (TPP) on the polymer backbone of the semiconducting polymer.⁹² Similarly, Liu *et al.* demonstrated multi-functional lipid-micelle complex incorporated with Pdts and a photosensitizer capable of exhibiting dual therapeutic effects of PDT and PTT.⁹³

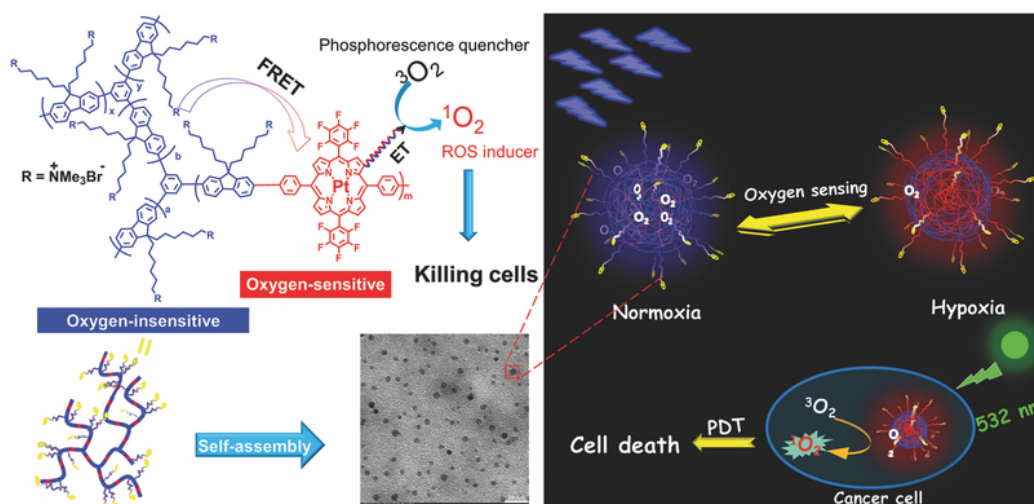


Figure 2-6: Self assembled phosphorescent Pdts for dual applications of O₂ sensing, and photodynamic therapy. Reproduced with permission from Reference ⁹¹, Copyright 2016, Wiley-VCH

VII. Photoacoustic Imaging

In the recent years, a hybrid imaging modality, photoacoustic imaging (PAI) has garnered considerable interest. This modality exploits the photoacoustic effect, wherein optical photons are absorbed and converted to thermal energy (heat), leading to acoustic waves emission from the transient thermoelastic expansion of the locally heated biological tissues.⁹⁴ This imaging modality is often applied as an *in vivo* label-free imaging modality for the high resolution imaging of saturated O₂ in the blood and cerebrovascular imaging through intact scalp and skull.⁹⁴ This signal is often enhanced by the use of external contrast agents. Recently research has revealed some semiconducting polymer dots capable of acting as excellent contrast agents for PAI, however limited research has been done in this area. Zhang *et al.* developed PIID-DTBT based semi-conducting polymer dots (Pdots) with strong NIR optical absorption, for multiscale and multispectral PAI.⁹⁵ The developed polymer dots exhibited superior photothermal conversion efficiency to gold nanoparticles and nanorods, both commonly used PAI contrast agents. In another work, Lyu *et al.* developed polymer dots as amplified theranostics for *in vivo* PAI and photothermal therapy of cancer.⁹⁶ The engineered polymer dots possessed a dual component structure composed of near-infrared absorbing semiconducting polymer and fullerene, that interacted with each other to induce photoinduced electron transfer. This resulted in a 2.6 and 1.3 fold enhancement of the PAI signal and maximum photothermal temperature.⁹⁶

VIII. Anti-microbial Agents:

The use of hydrophobic Pdots as potential anti-microbial agents has not been investigated. However, a few studies have been conducted using hydrophilic semiconducting polymers and polyelectrolytes. Wang *et al.* has designed cationic poly(*p*-phenylene vinylene) polyelectrolyte capable of selectively binding to and

damaging bacterial cells.⁹⁷ Several varieties of anti-microbial polymers have been developed over the years, some of which have seen utility as nanoparticles.⁹⁸ The most commonly existing antimicrobial polymers are either functionalized by microbial killing side chains or are used as delivery vehicles for anti-microbial agents.⁹⁹ However they are either expensive to synthesize or suffer high dosage requirements or both. There exists a significant dearth of investigation in the utilization of polymer dots as anti-microbial agents, as these zero-dimensional nanostructures may possess several unique properties.

2.3 Carbon Nanotubes

Carbon nanotubes are 1D rolled sheets of graphene built from sp^2 -hybridized carbon atoms that are single-walled (single tubes with diameters around 1 nm), or multi-walled (multiple concentric tubes with outer diameters ~ 30 nm).¹⁰⁰ These rolled up layers exhibit varying diameter, length and chirality resulting in unique physical, chemical and structural properties. The carbon nanotubes used in this work are commercially procured and thus, their synthesis strategies will not be discussed. Their properties will be briefly discussed followed by their application in biofuel cells.

2.3.1 Properties

Carbon nanotubes have sp^2 carbon bonds between individual atoms, lending them extraordinary mechanical strength.^{12, 100} Physically, single walled carbon nanotubes (SWCNTs) demonstrate diameters between 0.4 nm – 3 nm, with extremely long lengths (typically in micrometers).¹² They can easily form bundle like structures due to strong π - π interactions between individual SWCNTs.¹⁷ The multi-walled carbon nanotubes (MWCNTs) can form upto ~ 30 nm in diameter and demonstrate axial lengths upto a few centimeters.¹⁰⁰ The tips of the usually tend to be closed due to pentagonal defects and they rarely demonstrate good conductivity as compared to

SWCNTs.¹⁷

Single walled carbon nanotubes (SWCNTs) possess high degree of mechanical strength with a tensile strength higher than steel and Kevlar.¹⁷ Furthermore, they possess a high degree of elasticity, are lightweight and suffer from minimal structural damage on stretching to five times their original size.¹⁷ The SWCNTs can easily form bundles with high degrees of porosity and excellent surface areas. The diameter and chirality of the SWCNTs are described in the form of a unique vector (n,m) and together determine the specific structure of an individual nanowire.¹⁰⁰

Furthermore pristine metallic SWNTs also exhibit enhanced electronic properties, including ballistic electrical conduction whereby making this a suitable nanomaterial for enhancing electron transport in biocatalyst based electrochemical energy devices.¹⁸ In addition to their enhanced mechanical strengths and conductivity, SWCNTs possess high specific surface areas, excellent biocompatibility and good thermal conductivity.¹⁸

2.3.2 Carbon Nanotubes in Enzymatic Biofuel Cells

Healthcare of today makes use of many devices for diagnostics and treatment purposes. Of these, devices capable of operating within the human body in order to support, and monitor life, as we know it are termed as implantable devices (IMDs). Broadly divided into 2 categories based on power requirements, these devices either require power (Active IMDs: pacemakers, neuro-stimulators, defibrillators) or work without them (Passive IMDs: stents, valves).¹⁰¹ As expected, the active IMDs function by using power generated from external power sources (radio frequency pulses or wiring) or batteries present within the device.¹⁰¹ Consequently, this results in frequent replacement of the device, especially in case of battery operated ones (e.g. pacemaker) that often proves arduous on the patient.

The search for an alternative source for power generation is always ongoing, with an ideal implantable power source requiring the following; a continuous power supply, high performance, high biocompatibility, easily miniaturized, and being operable under physiological conditions.¹⁰¹ An old yet new area of research, biofuel cells (BFCs) have been widely researched into as power device alternatives capable of using biocatalysts (isolated enzymes or microbial enzymes) to generate electricity from various substrates and biofuels like glucose.¹⁰²⁻¹⁰³ However, enzymatic biofuels (EBFC) are superior to microbial fuel cells (MBFC) in their specificity, ease of enzyme production as well as lack of biocompatibility issues. Similar to conventional fuel cells, the BFC (Figure 2-7) comprises of two electrodes (anode and cathode) with the biocatalyst present on either one/both electrodes.

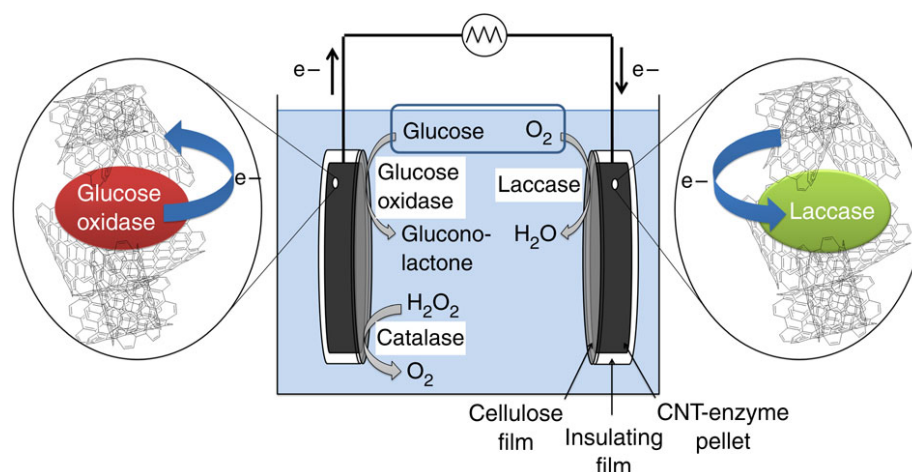


Figure 2-7: CNT based EBFC - At the anode, glucose is oxidized to gluconolactone, where the electrons are transferred from the GOX to CNT. Catalase decomposes hydrogen peroxide into oxygen and water. At the cathode, electrons are transferred from CNT to laccase where dioxygen is reduced to water. Reproduced with permission from Reference ¹⁰⁴. Copyright 2011, Nature Publishing Group (NPG).

While the fuel is oxidized on the bio-anode surface to generate electrons, the oxygen reduction occurs at the bio-cathode. A complete catalytic activity and proper immobilization of the biocatalysts is a pre-requisite for high power generation and

effective direct electron transfer with the electrode.¹⁰⁵ SWCNTs are highly desirable for use in these bio-power devices due to two following reasons:

- Their ability to access the embedded redox active centers of the biocatalysts (enzymes), thus establish a good enzyme-electrode connection for direct electron transfer.¹⁸
- Their high electrochemically active surface areas allows for high enzyme immobilization.¹⁸

Indeed the use of CNTs to immobilize enzymes for direct electron transfer in EBFCs has been recently gaining a lot of interest and extensive research has been done, some of which will be briefly reviewed here. Kim *et al.* reported separator free CNT yarn biofuel cells with high power densities of 2.18 mW cm^{-2} capable of functioning in human serum. However, the lifetime of the EBFC was extremely low with ~83% efficiency after 24 h.¹⁰⁶ On the other hand, Cosnier *et al.* reported highly stable mediatorless EBFCs based on compressed CNT-enzyme (Figure 2-7) electrodes with high power densities at 1.3 mW cm^{-2} and stability upto 1 month.¹⁰⁴ The electrodes were fabricated by the mechanical compression of the enzymes into the CNT matrix, resulting in enzymes being wired efficiently.¹⁰⁴ Similarly, Mano *et al.* fabricated osmium-CNT composite based EBFCs with power densities upto $740 \text{ } \mu\text{W cm}^{-2}$ and good circuit voltage of 0.57 V.¹⁰⁷ As seen in the above section, the potential for CNTs as connectors is immense and has potential to help develop the next generation of EBFCs.

| Material for Direct Enzyme Immobilization | Power Output of EBFC (μWcm^{-2}) | Reference |
|---|---|-----------|
| Graphite/Enzyme composite | 7 | 105 |
| Ketijen Black/Enzyme | 800 | 105, 108 |

| | | |
|--------------|------|-----|
| MWCNT/Enzyme | 126 | 105 |
| SWCNT/Enzyme | 1300 | 104 |

Table 2-3: Performance comparison between EBFCs fabricated using materials for enhancing direct electron transfer

2.4 Graphene

First isolated mechanically in 2004 by Novoselov *et al.*,¹⁰⁹ the interest in using graphene in biomedical applications became apparent only in the late 2000s.¹¹⁰ Another carbon allotrope, graphene is a single-atom thick planar sheet whose carbon atoms are packed in sp^2 -bonded hexagonal pattern.¹⁹ 2D graphene, similar to 1D semiconducting polymers has a large cloud of delocalized π -electrons. This makes it immensely suitable for energy transfer related applications, fluorescence quenching based biosensing and so forth.¹¹⁰ This two-dimensional (2D) monolayer of π -conjugated carbon exhibits several unique physical, chemical and optical properties such as high carrier mobility and capacity, high electron transfer rate, high robustness, flexibility, large specific area, size dependent fluorescence, and outstanding structural properties (e.g. single atom thickness).^{19-20, 110}

Due to these fascinating properties graphene shows potential as a catalyst support.¹¹¹ Generally, the catalyst support materials require properties such as:

- (a) High specific surface area,
- (b) Chemical stability under oxidative and reductive conditions,
- (c) High electrochemical stability under operating conditions,
- d) High conductivity,
- (f) Durability & support

The addition of various nanostructures onto the graphene surface to produces composites that improve on their intrinsic catalytic properties. Over the years, graphene has been paired with various materials such as inorganic nanostructures, organic crystals,¹¹² polymers,¹¹³ biomaterials (ex. biocatalysts),¹¹⁴ and carbon nanotubes (CNTs).²⁰

However, the 2D form of graphene has several inherent drawbacks such as reduced active areas, aggregation tendencies in solutions due to its high hydrophobicity, morphology of 2D electrodes leading to inefficient diffusion, charge/ionic transfer.¹¹⁵ The integration of these individual 2D sheets to form three-dimensional (3D) architectures is capable of improving on or eliminating these drawbacks. The porous nature of the resultant 3D architectures usually reflects significantly higher surface areas, flexibility, presence of pores, large pore volumes, higher electrical conductivity amongst other improved properties.¹¹⁵ The presence of these pores helps in the promotion of mass transport as well as improves its features for its use as excellent electrode materials for electrochemical biofuel cell applications.

2.4.1 Synthesis of 3D Graphene

Graphene, due to its versatile structure and unique properties is a prime candidate to assemble 3D structures by self-assembly, template driven synthesis or direct deposition methods.¹¹⁶⁻¹¹⁷ A number of 3D graphene structures such as honeycomb structures, graphene balls, porous films, graphene fibers and graphene tubes have been developed over the years.¹¹⁵ As mentioned previously, the 3D graphene architecture comprises of pores whose sizes vary from sub-micrometer ranges to several millimeters. This macro-porous structure in turn results in improved properties including extreme lightness, high mechanical strength, significant compressibility, superb conductivity, absence of aggregation/restacking of graphene sheets during

assembly, increased specific surface area, as well improved degree of interaction between electrodes and electrolytes.¹¹⁸ Additionally the 3D porous material provides for high transportation rates, multidimensional electron transport paths that are important for biofuel cell applications.¹¹⁹

I. Self-Assembly

Self-assembly is commonly used strategy to obtain 3D graphene structures. For example: gelation can be induced by varying the electrostatic repulsions between colloids is applied to graphene oxide (GO) aqueous dispersions to promote self-assembly into 3D structures.¹¹⁵ The assembled macrostructures have novel physiochemical properties that differ from their individual counterparts, and demonstrate improved properties for real-time applications. The process by itself is driven by various interactions such as *van der waal* forces, hydrogen bonding, electrostatic, hydrophilic/hydrophobic interactions, and dipole interactions (Figure 2-8).¹¹⁶

In brief, the various self-assembly based synthesis strategies include organo-gelation based synthesis wherein monolithic graphene architectures by the formation of physical or chemical cross-linkers.¹¹⁶ The process occurs between the various species including the GO and gelator molecules, monomers or polymers. Banerjee *et al.* produced transparent, stable and fluorescent organogels by incorporating inert graphene into N-terminal pyrene conjugated oligopeptides using the method.¹¹⁶ Hydrothermal synthesis is another self-assembly methodology where the assembly occurs due to merger or partial over-lapping of flexible graphene sheets with physical cross-linker sites (Figure 2-8a).¹²⁰ The arrangement into the 3D architecture is driven by the π - π interactions of the sheets, where the structure & morphology was dependent on parameters such as precursor concentration or hydrothermal reduction time.¹¹⁸ Architectures of various shapes (triangular, prisms, quadrangular prisms etc.)

have been designed using pH mediated hydrothermal reduction in the presence of ammonia or hydroxides.¹²¹

Another method for 3D architecture preparation utilizes the principles of sol-gel chemistry (Figure 2-8b) to form physical cross-links between graphene sheets. Zhang *et al.* developed graphene aerogels from graphene hydrogel precursors by chemically reducing GO in the presence of a reducing agent (L-ascorbic acid).¹¹⁶ An efficient separation based self-assembly technique wherein separation followed by drying is the flow-directed self-assembly of GO. This has been utilized to fabricate 3D graphene oxide (GO) & reduced graphene oxide (rGO) paper.¹¹⁶ Another self-assembly technique (Breath figure assembly) works by assembling graphene sheets into biologically mimicked honeycomb structures. It was used in order to attain ordered structures during chemical assembly processes.¹¹⁶ However while 3D graphene foams (GFs) can be prepared using hydrothermal, chemical reduction methods and other self-assembly processes they often suffer from drawbacks such as poor conductivity and structural defects.

II. Template directed growth

Template driven methods were observed to be highly effective for the fabrication of pristine, well defined 3D porous graphene networks (Figure 2-9). Compared to self-assembled growth (Figure 2-8), template directed growth results in highly controlled morphologies and properties.¹¹⁵

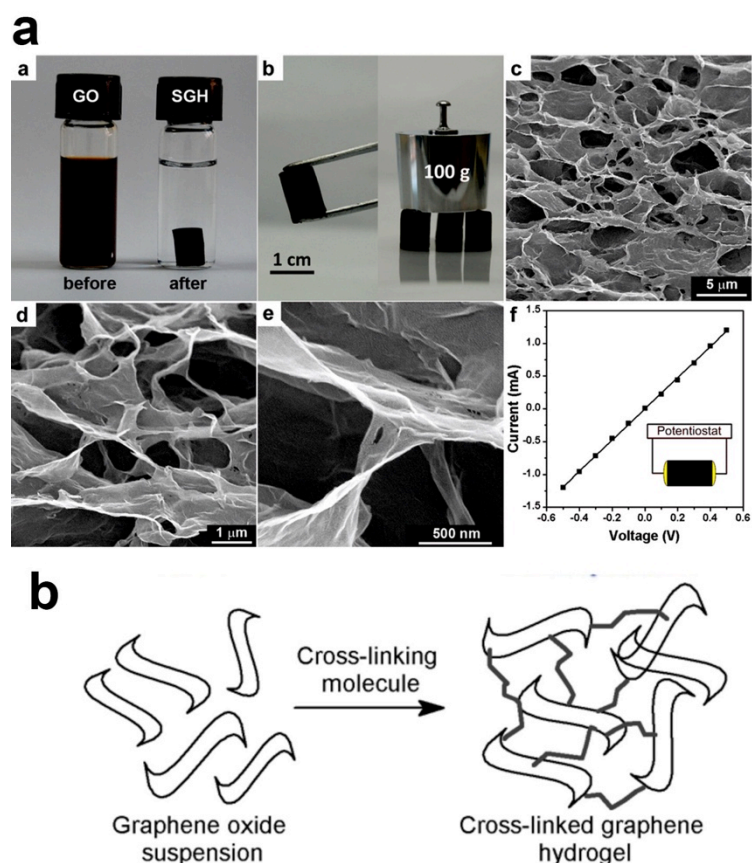


Figure 2-8: (a) Hydrothermal driven self-assembly of 3D graphene foam. Adapted with permission from Reference ¹²². Copyright 2015, American Chemical Society. (b) 3D Graphene hydrogel formation in the presence of cross-linkers. Adapted with permission from Reference ¹²³. Copyright 2014, One Central Press (OCP).

1. Chemical Vapor Deposition

High purity 3D graphene can be obtained under chemical vapor deposition (CVD) process using methane (CH_4) ¹¹⁷ or ethanol ¹²⁴⁻¹²⁵ at 1000 °C, under ambient pressure using porous nickel foam as a template (Figure 2-9a). The resultant freestanding graphene are macroporous, mechanically robust, show excellent conductivity, high electrochemical stability and can serve as good electrode materials capable of improving the performance of various biomedical devices including biofuel cells and biosensors.²¹ Currently, this method of template driven synthesis is the most commonly used method to synthesize pristine, high quality 3D graphene. Other than nickel foams, alternative templates (Figure 2-9b) such as copper ¹²⁶ and gold ¹²⁶ have

been used to synthesize graphene, albeit the 2D form. These CVD derived 3D graphene-foam monoliths exhibit superior behavior and quality as compared to the 3D graphene structures synthesized from chemically derived graphene sheets. The graphene sheets form continuous & well-interconnected 3D networks without any breaks or cracks and remains in direct contact with one another. Furthermore, they are of very high quality, show excellent electrical conductivity and demonstrate good biocompatibility.¹¹⁰⁻¹¹¹

2. Other Templates

Another template directed technique, wherein 3D porous graphene in aqueous solution was fabricated using a freeze-drying approach by Mann *et al.*¹¹⁶ The low temperatures used, were crucial for controlling the alignment and macroscale porosity of the fabricated structures. Similarly, the use of SiO₂ template (hydrophobic interaction driven hard templating) yields nanoporous 3D graphene with controlled pore sizes, large surface areas, & immense total pore volumes.¹¹⁶ Alternatively, the conversion of pre-defined 3D photoresist films into well-defined 3D porous graphene is yet another strategy. Developed by Polsky *et al.*, this method results in 3D graphene with significantly smaller dimensions compared to previously reported counterparts.¹²⁷

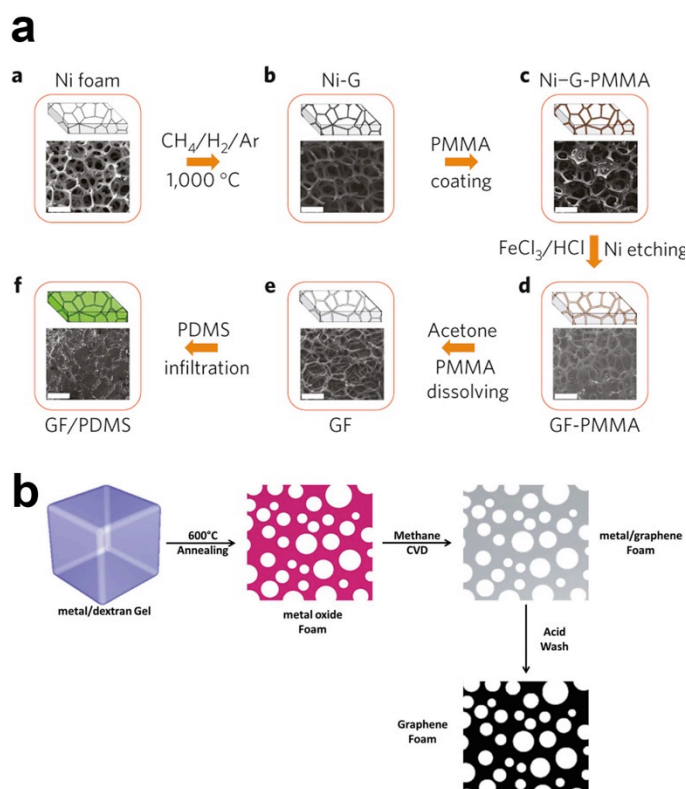


Figure 2-9: (a) Chemical vapor deposition grown macroporous 3D graphene on Nickel foam. Adapted by permission from Macmillan Publishers Ltd: Nature Materials Reference ¹¹⁷, Copyright 2011, Nature Publishing Group (NPG). (b) Schematic for gold and copper template driven synthesis. Reproduced with permission from Reference ¹²⁶. Copyright 2016, Published by The Royal Society of Chemistry.

| 2D Graphene | 3D Graphene |
|--|---|
| Poor morphology due to high hydrophobicity | High purity, pristine, superior quality & performance |
| Prone to aggregation in solution | Chemically inert |
| Reduced mass transfer & poor electrolyte diffusion | Porous & well interconnected networks |
| Difficult to obtain in pristine form | Excellent electrical conductivity & surface area |

Table 2-4: Advantages of 3D graphene over 2D graphene.

2.4.2 Properties

Graphene due to its π -conjugated nature shows a variety of unique and interesting properties. In addition to its large physical surface area, the sp^2 hybridized structure contributes to the high electron transport values, and improved electrical conductivities for graphene. Additionally its pristine nature results in a high degree of chemical inertness, making it a good potential electrode material. Furthermore the materials possess excellent electrochemical properties with respect to surface chemistry and structure, heterogeneous redox charge transfer rate constants, wide operating window, electrochemical stability and electro-catalysis of molecules.¹¹¹ A notable feature of graphene is its extremely large electrochemically active surface area, which demonstrates is large potential to form composites with various materials to improve performance.¹¹¹ Furthermore, when composited with nanomaterials such as carbon nanotubes (CNTs), transitional metal oxides, hydroxides and sulfides, the 3D graphene-composites show an enhancement in the intrinsic properties of the nanomaterials including improved conductivity and stability (derived from 3D graphene). The structure with its high surface area, porous structure and continuous backbone can easily promote rapid transmission of electrons and shorten transport path of the electrolyte during high rate processes.¹¹⁸

2.4.3 Biomedical Applications of 3D Graphene as Catalyst Support

The use of graphene based materials for biomedical applications can be divided into two categories. The first category uses nanostructured graphene (e.g. graphene quantum dots) and functionalized graphene derivatives (e.g. graphene oxide) for applications such as drug delivery, fluorescent sensing and therapy.¹²⁸⁻¹²⁹ On the other-hand, the second category uses larger macroscopic forms of graphene (e.g. 2D and 3D electrodes) as a catalyst support for biocatalysts such as enzymes for electrochemical

based biomedical applications including biosensing and enzymatic biofuel cells.¹¹¹ Only the latter category of applications, specifically those regarding enzymatic biofuel cells will be discussed here.

Graphene can also be used as a catalyst support material (electrodes) in fuel cells, improve various electrochemical properties on the whole system such as ionic transport, charge transport etc. In particular, from a biomedical perspective graphene was found to integrate very effectively with biocatalysts such as enzymes, microbes, and biomolecules. Owing to its ultra-high surface area and excellent electron mobility, graphene (2D and 3D) has been modified with various biocatalysts to fabricate electrodes for use in electrochemical biofuel cells and biosensors with high power densities and sensitivities, respectively.^{21, 119, 130}

1. Biofuel Cells:

EBFCs have already been briefly introduced in the previous section, only prior work regarding 3D graphene based enzymatic biofuel cells will be discussed here. Despite its rising popularity as an electrode material for biofuel cells, very few 3D graphene based systems have been reported. Due to their advantageous properties this material has been composited with various catalysts (e.g. metal oxides¹³¹) and catalyst support materials (e.g. semiconducting polymers,¹³² nanoparticles¹³³) to fabricate bio-electrodes for the biofuel cells. However, as a result of their specificity and biocompatibility the focus will be on enzymatic biofuel cells.

For instance, Liu *et al.* developed a graphene and silica sol-gel matrix based glucose EBFC which demonstrated power densities of $24.3 \pm 4 \mu\text{W cm}^{-2}$.¹³⁴ Another EBFC fabricated by Wang *et al.* based on integration of the graphene/enzyme composite into 3D micro-pillar arrays resulted in an increased enzyme loading. With an enhanced direct electron transfer, this translated into the EBFC realizing power densities of

$136.3 \mu\text{Wcm}^{-2}$.¹³⁵ Subsequently, Campbell *et al.* fabricated a membrane/mediator-free EBFC, which produced a power density of 0.19 mWcm^{-2} .¹³⁶ Clearly, the varying power densities were a factor of different immobilization strategies, diverse biocatalysts and electrode material properties. The use of 3D as graphene as a catalyst support in biofuel cells is yet largely unexplored and open to significant performance enhancements.

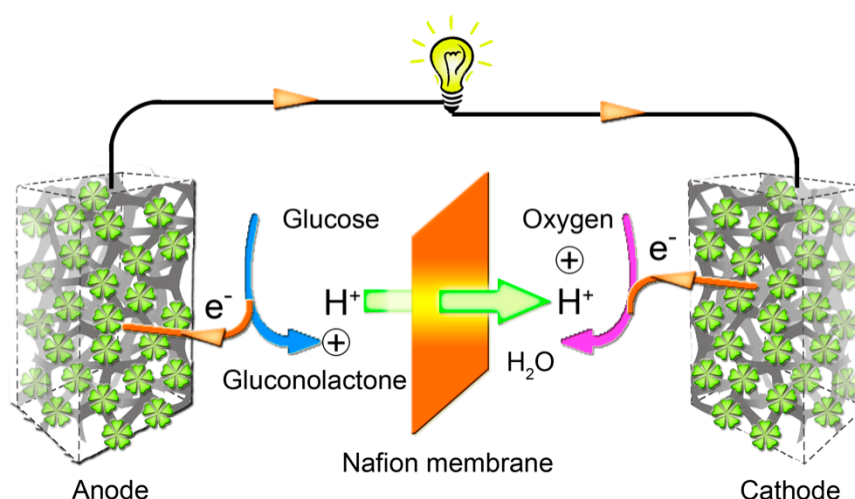


Figure 2-10: 3D graphene- CO_3O_4 based multi-sugar biofuel cell. Reproduced with permission of PCCP Owner Societies from Reference¹³¹, Copyright 2013, Royal Society of Chemistry.

| Electrode | Power Output (μWcm^{-2}) | Fuel Concentration (mM) |
|------------------------------------|---------------------------------------|-------------------------|
| Carbon Fibers Composite | 350 | 15 |
| Carbon Nanotubes Fibers Composites | 740 | 15 |
| Carbon Nanotube Composite | 1300 | 50 |
| 2D Graphene Composite | 24.3 ± 4 | 100 |
| 3D Graphene Composite | 2375 ± 170 | 200 |
| Carbon Fiber Sheet Composite | 1450 ± 240 | 400 |

Table 2-5: Different carbon based¹³¹ electrode materials and 3D graphene¹³¹ based electrodes in biofuel cells

2. Biosensing

A constant challenge in biosensing is its need for constant improvement with regards to selectivity, sensitivity and low costs of production. The high electrical conductivity of 3D graphene realized its potential as excellent material for the electrochemical sensing of various biomolecules, including glucose, DNA and proteins, with high sensitivities.^{110, 137-139} Chen *et al.* developed CVD grown 3D-CNT hybrid electrodes for the detection of dopamine. The hybrid electrodes exhibited a sensitivity of ($\sim 470.7 \text{ mA M}^{-1} \text{ cm}^{-2}$) and a low detection limit ($\sim 20 \text{ nM}$ with $S/N = 9.2$).¹⁴⁰ Further discussion regarding use of 3D graphene as catalyst supports for biosensors will not be added, as it is not in the context of this work. The use of 3D graphene based electrodes to push the performance boundaries of existing applications in biofuel cells and other biomedical devices is in its infancy, with more interesting and promising discoveries waiting to happen.

Chapter 3

3. Polymer Dots Derived from Poly (3,4-Ethylenedioxythiophene) and their Applications for Optical Imaging and Sensing

As seen in Chapter 2, Polymer dots (Pdots) from fluorescent semiconducting polymers show superior photo-stability along with other merits including high brightness, tunable photoluminescence properties, non-blinking property, and biocompatibility. As discussed in the previous chapter, bottom-up synthetic approaches provide better control over the yield, size and properties of the polymer dots. The most commonly used bottom up technique is chemical synthesis³³. However this technique is highly tedious and time-consuming and invariably requires a high degree of expertise. The limited post-polymerization preparation methods and tedious bottom-up synthesis techniques often result in large sized polymer nanoparticles (sometimes upto 100 nm) and highlight a need for alternative preparatory methods for these Pdots.

Electrochemical approaches are often desirable due to their sustainability, reduced cost of synthesis, facile, clean and green nature. Often electrochemical based synthesis strategies provide a higher degree of control with reduced byproducts.³⁶ Poly (3,4-Ethylenedioxythiophene) (PEDOT) is a chemically stable, low band-gap π -conjugated polymer that is non-fluorescent in its conducting state. A widely researched polythiophene derivative PEDOT due to its excellent electrical and optical properties has seen widespread use in LCDs, solar cells, and organic LEDs.¹⁴¹

In this chapter a facile approach to synthesize a new type of polymer dots derived from non-fluorescent poly(3,4-ethylenedioxythiophene) (PEDOT) is demonstrated. Various properties including the physical, chemical and biological properties of the PEDOT-Pdots are studied. We further elucidate on the optical properties of these PEDOT-Pdots

using theoretical calculations. Subsequently the application of these PEDOT-Pdots as cellular imaging fluorophores in rat neuroblastic cells (PC12), and selective optical sensors towards mercury ions (Hg^{2+}) is demonstrated.

3.1 Materials & Methods

3.1.1 Preparation of the fibrous PEDOT film

3,4-ethylenedioxythiophene (EDOT) monomer, ionic liquid (1-Butyl-3-methylimidazolium tetrafluoroborate - BMIMBF₄) and N,N-Dimethylformide (DMF) were purchased from Sigma Aldrich. With 0.1 M EDOT monomer in the ionic liquid, PEDOT film was polymerized on an ITO (Indium tin oxide) working electrode held at the constant potential of 1 V for 3 h. An electrochemical workstation (CHI 660D) was used for polymerization, in a three-electrode configuration consisting of a platinum plate counter electrode, silver wire reference electrode and an ITO working electrode. Thorough washing to eliminate excess ionic liquid and unreacted monomers, and overnight drying in a vacuum oven at 27 °C followed polymerization.

3.1.2 Preparation of PEDOT-Pdots

The polymer film was then gently scraped off the ITO electrode and suspended in DMF solvent (1 mg/ml), followed by ultrasonication (Branson 2510; 1.1 A, 230 W) at 27 °C for 4 h. After centrifugation at 10,000 rpm for 30 min, the supernatant was collected. This was repeated for 5 times to obtain the dispersion of PEDOT-Pdots in DMF, which was subsequently filtered using a WHATMAN 0.2 µm PTFE filter. To re-suspend PEDOT-Pdots in distilled water, DMF was completely extracted using rotary evaporation at 80 °C, and distilled water was added to the dried QD aggregates. The solution was then ultra-filtered (molecular cut-off weight of 3 kDa) to remove the

aggregates. PEDOT-Pdot suspensions in both DMF and water are highly stable (lasting for months without apparent aggregation).

3.1.3 Characterization

The samples were examined by Field emission scanning electron microscopy (FESEM, JMS-6700F), Atomic force microscopy (MFP-3D AFM microscope, Asylum research), Raman spectroscopy (WITec CRM200 using 633 nm laser), High-resolution transmission electron microscopy (HRTEM, JEOL 2010), X-ray photoelectron spectroscopy (XPS, ESCALAB MK-II), X-ray diffraction (XRD, Bruker D8 Avance diffractometer using Cu K α radiation) and Fourier transform infrared spectroscopy (FTIR, Perkin Elmer FTIR Spectrum GX 69233). The UV-Vis absorption and photoluminescence (PL) behavior of the QDs were characterized by UV-2450 spectrophotometer (Shimadzu), and LS-55 fluorescence spectrometer (PerkinElmer), respectively.

3.1.4 Cell imaging

The PC12 cells (American Type Culture Collection) were cultured in Dulbecco's modified Eagle's medium (DMEM, Gibco) supplemented with 10% (v/v) fetal bovine serum (Gibco) and 1% penicillin–streptomycin, at 37 °C under a humidified atmosphere containing 5% CO₂ and 95% air. Cells were incubated with 76.6 μ g/ml blue PEDOT-Pdots (dispersed in water) or 5.5 μ g/ml green PEDOT-Pdots (dispersed in DMF) for 24 h before being imaged with a confocal laser scanning microscope (LSM 510 Meta, Carl Zeiss GmbH, Germany). The blue (or green) PEDOT-Pdots were excited at 405 (or 488) nm and detected with an emission filter <480 nm (or >520 nm).

3.1.5 Cell Viability & Proliferation Assay

The cell viability was determined using a MTT (3-(4,5-dimethylthiazol-2-yl)-2,5-diphenyl tetrasodium bromide)-based cell growth determination kit (Sigma-Aldrich, USA). Briefly, after washing with phosphate buffer saline (PBS), the cells were incubated in a culture medium containing MTT reagent solution (5 mg/ml MTT in DMEM without phenol red) (10% v/v) for 4 h at 37 °C. Subsequently, MTT solvent (0.1 N HCl in anhydrous isopropanol) was added to the culturing well (50% v/v), followed by absorbance measurements of the MTT formazan crystals at 570 nm using a Victor3 plate reader (PerkinElmer Inc., USA).

3.1.6 Optical detection of Hg^{2+} ions

The photoluminescence of the green PEDOT-Pdots (200 $\mu\text{g/ml}$ in water) was measured before and following addition of various metal salts at defined concentrations, including Mercury (II) perchlorate, Lead(II) nitrate, Zinc nitratehexahydrate, Cadmium chloride, Cesium chloride, Magnesium sulphate, Cobalt nitratehexahydrate, Nickel nitratehexahydrate, Manganese nitratetetrahydrate, Gold(III) chloride trihydrate and Potassium chloride.

3.2 Results and Discussion

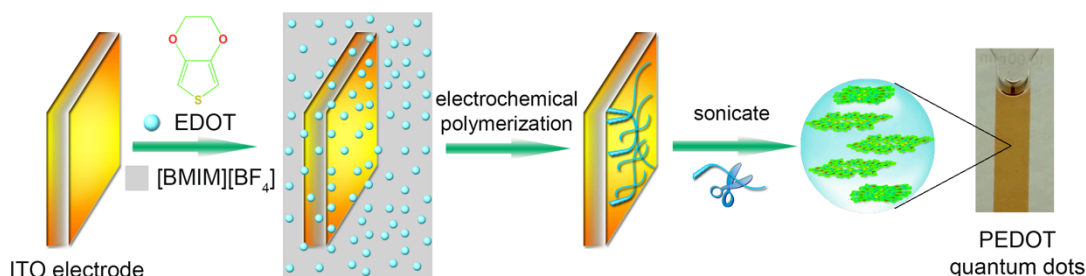


Figure 3-1: Schematic illustration for the preparation of PEDOT-Pdots.

3.2.1 Synthesis and Morphology of PEDOT-Pdots

As schematically illustrated in Figure 3-1, EDOT monomers are electro-polymerized in an ionic liquid (BMIMBF₄). Field-effect scanning electron microscopy (FESEM) reveals that a film of polymerized EDOTs (PEDOT) consequently forms on the ITO electrode (Figure 3-2a). On the film, ultra-long wires and roots of outgrowing wires can be observed (bright dots and lines in Figure 3-2a). A closer inspection shows that the film consists of dense interwoven fibers (inset in Figure 3-2a). The fibrous PEDOT film is then sonicated in DMF solvent, producing a yellow solution with well-dispersed PEDOT-Pdots exfoliated from the film (Figure 3-1). As observed from atomic force microscopy (AFM), the PEDOT-Pdots exhibit (Figure 3-2b and 3-2c) with an average thickness of ~ 0.40 nm (± 0.17 , $n = 152$), with ~ 0.21 nm corresponding to the thickness of a single PEDOT chain.¹⁴² This suggests that PEDOT-Pdots range from single to a-few layers. High-resolution transmission electron microscopy (HRTEM) shows that PEDOT-Pdots are uniform in diameter ($\sim 2.3 \pm 0.36$ nm, $n = 172$) (Figure 3-2d and 3-2e). The diffraction pattern indicates the PEDOT-Pdots possess a limited degree of crystallinity (lower inset in Figure 3-2d). Indeed, a well-defined crystal lattice can be resolved from some QDs under high-resolution TEM (upper inset in Figure 3-2d). Consistent with a previous study,¹⁴³ the observed lattice spacing of 3.4 \AA corresponds to the characteristic face-to-face distance (010) of the rigid PEDOT polymer. Therefore, it appears that the disc-like QDs are mechanically chopped by sonication from the slightly crystalline PEDOT polymer chain. The gel-electrophoresis results (Figure 3-2f) of PEDOT-Pdot sample are compared with protein markers to speculate the molecular weight. The bright field and fluorescence gel images show a narrow band of PEDOT-Pdots, indicating a uniform size distribution and a molecular weight < 10 kDa.

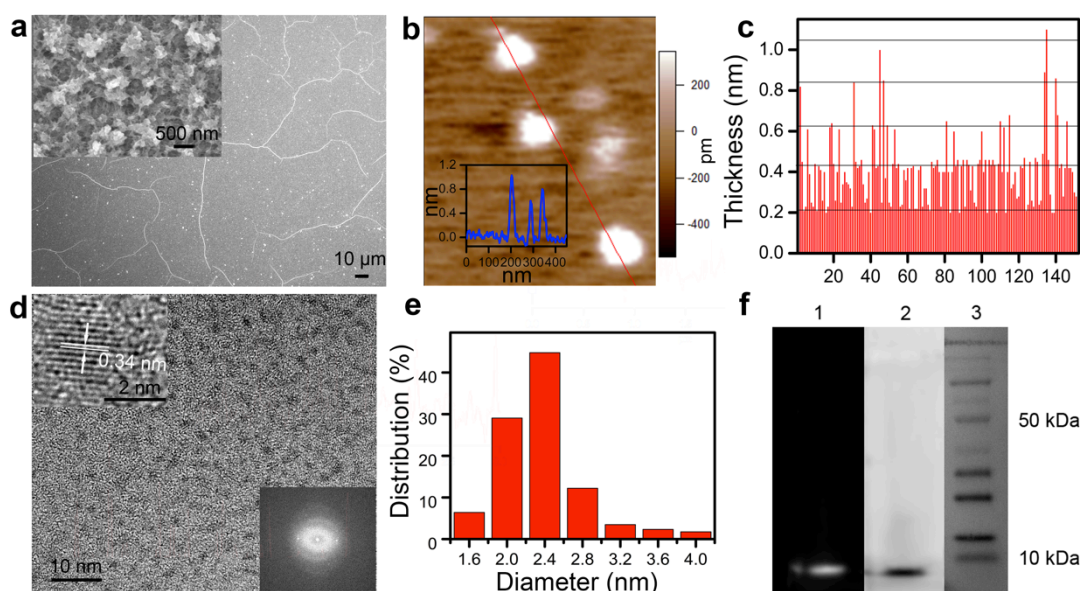


Figure 3-2: QDs exfoliated from the fibrous electropolymerized PEDOT film are small and uniform in size. (a) FESEM image of the PEDOT. Inset shows the film surface with a higher-resolution. (b) AFM image of PEDOT-Pdots. Inset shows the height profile along the indicated line. (c) The height (thickness) of 152 individual PEDOT-Pdots. The indicative horizontal lines are 0.21 nm apart. (d) HRTEM image of PEDOT-Pdots. The upper inset presents a single PEDOT-Pdot with resolved crystal lattices. The lower inset gives the FTT diffraction pattern. (e) Diameter distribution of 172 PEDOT-Pdots. (f) The gel electrophoresis of PEDOT-Pdots (1 - fluorescent image under UV; 2 – bright field image) and protein markers (3).

3.2.2 Chemical Characterization

X-ray photoelectron spectroscopy (XPS) spectra of both PEDOT-film and PEDOT-Pdots show the characteristic S2s (228 eV), S2p (163 eV), C1s (283 eV) and O1s (531 eV) peaks from PEDOT (Figure 3-3a).¹⁴⁴⁻¹⁴⁵ The spectrum of PEDOT-film also exhibits B1s (193 eV), N1s (401 eV), and F1s (685 eV) peaks resulting from the residual ionic liquid (BMIMBF₄) from the polymerization process.¹⁴⁶ The B1s and F1s peaks appear practically non-existent in the XPS spectrum of PEDOT-Pdots while the N1s peak appears significantly reduced. Resolution of the C1s (Figure 3-3b) and S2p

(Figure 3-3c) XPS spectra indicate the existence of the (C=C) sp^2 , (C-C) sp^3 , C-S, C-O, $S2p_{3/2}$, and $S2p_{1/2}$ peaks characteristic to PEDOT, and small C-N and C=N peaks characteristic to [BMIM]⁺, respectively.¹⁴⁷⁻¹⁴⁸ The small amount of association of the nitrogen-containing ionic liquid is also confirmed by the high-resolution N1s spectrum (Figure 3-3b inset). In addition, Raman spectra (Figure 3-3d) of both PEDOT film and PEDOT-Pdots are comparable and in agreement with the characteristic spectrum of PEDOT.¹⁴⁹ Consistent with XPS characterization, Fourier transform infrared spectra (FTIR) of PEDOT-Pdots (Figure 3-3e) in both water and DMF show the characteristic peaks from PEDOT at 1638 cm^{-1} (C=C stretching vibration), 1385 cm^{-1} (C=C stretching of thiophene ring), 1124 cm^{-1} (polythiophene absorption), 1084 cm^{-1} (C-O stretching), and 929 cm^{-1} (C-S stretching).¹⁵⁰ Furthermore, the peaks from BMIMBF₄ are also observed at 1576 cm^{-1} and 1459 cm^{-1} (both from imidazole ring adsorption).¹⁵¹ The d_{020} peak in the X-ray diffraction (XRD) spectrum of PEDOT-Pdots corresponds to the face-to-face packing between the PEDOT chains with a distance of 0.34 nm¹⁴³ (Figure 3-3f). This correlates well with the HRTEM observation shown in Figure 3-2d.

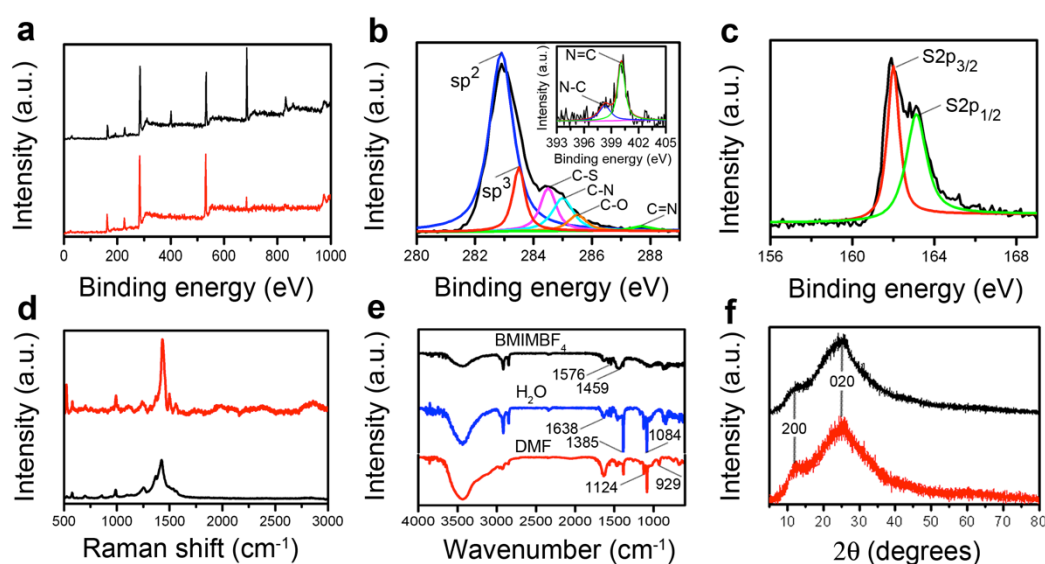


Figure 3-3: Spectroscopic characterizations. (a) XPS spectra of PEDOT film (black) and PEDOT-Pdots (red). (b) High-resolution C1s peak in XPS spectrum of PEDOT-Pdots. Inset

shows N1s peak. (c) High-resolution S2p peak in XPS spectrum of PEDOT-Pdots. (d) Raman spectra of PEDOT film (black) and PEDOT-Pdots (red). (e) FTIR spectra of BMIMBF₄ (black), PEDOT-Pdots (blue – in water; red – in DMF). (f) XRD Spectra of PEDOT Film (black) and PEDOT-Pdots (red).

A simple method for synthesis of a new type of polymer dots is demonstrated. In addition to mechanical stress induced by sonication, it is conceivable that the exfoliation of QDs from PEDOT fibers is facilitated by the intercalation of the ionic liquid (BMIMBF₄). We speculate the imidazole ring of BMIM⁺ interacts with PEDOT *via* π - π and electrostatic interactions to generate the amphiphilic nature of PEDOT-Pdots. In support of this, it has been previously reported that ionic liquids can intercalate into PEDOT films and cause swelling.¹⁵² Furthermore, it seems that DMF solvent also play an important role in exfoliation and stabilizing the exfoliated PEDOT-Pdots. In comparison, high-yield exfoliation of PEDOT-Pdots does not occur in other solvents (specifically, ethanol, water, and acetonitrile).

3.2.3 Optical Characterizations

The thus prepared quantum dots are amphiphilic and can disperse completely in DMF and water. They can be extracted from DMF using rotary evaporation for re-suspension in water. The absorption spectra of these two suspensions are shown in Figure 3-4a. The water suspension of PEDOT-Pdots efficiently absorbs UV light while the DMF suspension extends its adsorption to the visible light region. The excitation-dependent emission spectra of both QD suspensions indicate the maximum emission peaks from PEDOT-Pdots in DMF and in water at 533 nm (excited at 460 nm) and 450 nm (excited at 360 nm), respectively (Figure 3-4b and 3-4c). Clearly, the optical properties of PEDOT-Pdots depend on their interaction with the solvent. Furthermore, the excitation dependence suggests heterogeneity in the size and properties of

synthesized QDs. In comparison, EDOT monomers suspended in DMF or water do not show apparent absorption and emission, suggesting that the observed optical properties arise from extended conjugation lengths.

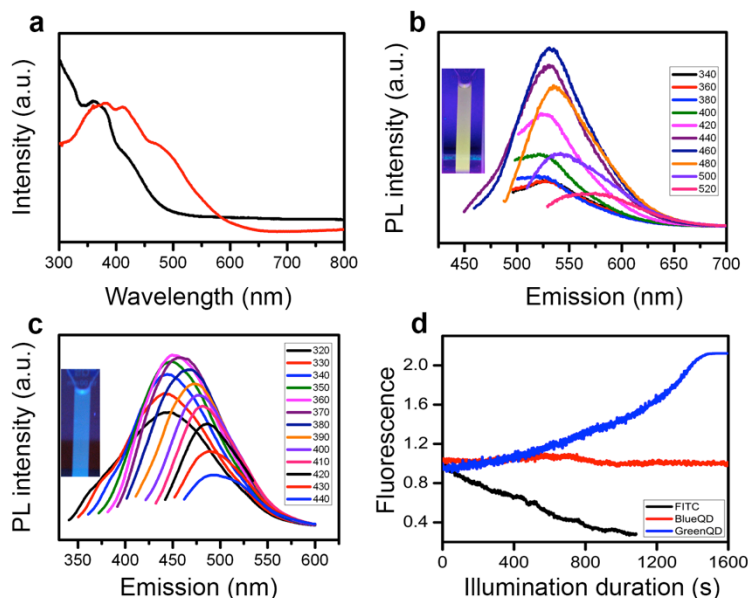


Figure 3-4: Optical characteristics of PEDOT-Pdots. (a) UV-Vis adsorption spectrum of PEDOT-Pdots in water (black) and DMF (red). (b) And (c) PL spectra of Pdots in DMF and water with different excitation wavelengths. The insets show the images of the Pdot suspensions under UV. (d) The photobleaching behavior showing normalized fluorescence of the green Pdots (in DMF), blue Pdots (in water), and FITC under continuous confocal imaging.

To reveal the absorption and emission mechanism, density functional theory (DFT) and time-dependent DFT (TDDFT) calculations were performed. The DFT calculations on EDOT trimers (using it as a model compound for PEDOT-Pdots) suggest that they assume three thermodynamically stable configurations (isomer 1 – 3 as shown in Figure 3-5). In the order of stability the high dipole moment containing Isomer 3 was the most thermodynamically stable configuration, followed by Isomers 2 and 1, respectively. The high thermodynamic stability of Isomer 3 was due to the formation of multiple hydrogen bonds with water molecules, but not in aprotic DMF

solvent. Therefore, we speculate that DMF suspension contains isomer 1 and 2 while isomer 3 dominates the water suspension. Theoretical calculations indicated the absorption peaks of isomer 1 and 2 in the dielectric environment of DMF to be 411 and 390 nm, respectively (Table 3-1).

| EDOT trimer | Polarizable continuum model | Band gap ^a (eV) | E _{abs} (eV) | λ _{abs} (nm) | Oscillator strength, <i>f</i> |
|-------------|--------------------------------|-------------------------------|-----------------------|-----------------------|----------------------------------|
| Isomer 1 | DMF | 3.29 | 3.01 | 411.39 | 0.95 |
| Isomer 2 | DMF | 3.52 | 3.18 | 389.51 | 0.88 |
| Isomer 3 | Water | 3.87 | 3.43 | 361.51 | 0.73 |

^aBand gap = Ground-state HOMO-LUMO energy gap.

Table 3-1: Calculated ground-state band gap^a, absorption energy (E_{abs}), absorption wavelength (λ_{abs}) and associated oscillator strength of EDOT trimer.

| EDOT trimer | Polarizable continuum model | E _{em} (eV) | λ _{em} (nm) | Oscillator strength, <i>f</i> |
|-------------|--------------------------------|----------------------|----------------------|----------------------------------|
| Isomer 1 | DMF | 2.41 | 515.04 | 1.21 |
| Isomer 2 | DMF | 2.37 | 522.76 | 1.16 |
| Isomer 3 | Water | 2.60 | 476.58 | 0.97 |

Table 3-2: Calculated emission energy (E_{em}), emission wavelength (λ_{em}) and associated oscillator strength of EDOT trimer.

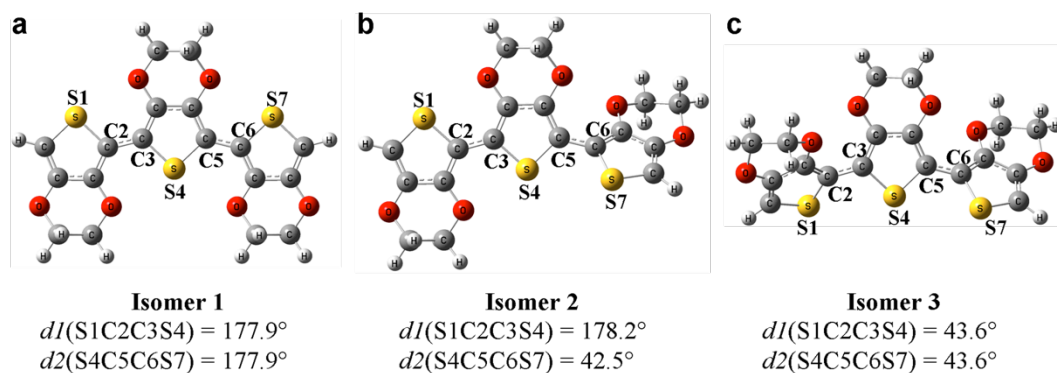


Figure 3-5: Different isomers of EDOT trimer. The isomers vary by the dihedral angles [d1(S1C2C3S4) & d2(S4C5C6S7)]. The figures indicate the conformations of **(a)** Isomer 1 [d1 = 177.9° & d2 = 177.9°], **(b)** Isomer 2 [d1 = 178.2° & d2 = 42.5°], **(c)** Isomer 3 [d1 = 43.6° & d2 = 43.6°]

These values agree well with the experimentally observed peaks at ~412 nm and ~384 nm (Figure 3-4a). The absorption peak of isomer 3 in water was predicted to be 362 nm, close to the experimentally observed values (~360 nm as shown in Figure 3-4a). Similar to the observed emission peak of PEDOT-Pdots in DMF (~533 nm), the emission peaks of isomer 1 and 2 were calculated to be 515 and 523 nm, respectively (Table 3-2). Isomer 3 in water showed emission at 477 nm, consistent with observed emission peaks of PEDOT-Pdots in water (~450 nm). With a small optical band gap (1.6 eV) resultant from rapid electron-hole recombination, PEDOT is natively non-fluorescent.¹⁵³ As shown by our theoretical studies (Table 3-1), the resulting photoluminescence properties of the nano-sized PEDOT-Pdots arise from the band-gap widening because of quantum confinement. The PEDOT-Pdots are observed to exhibit two excitation peaks (Figure 3-6) resulting from σ to π^* and π to π^* transitions (Figure 3-7).

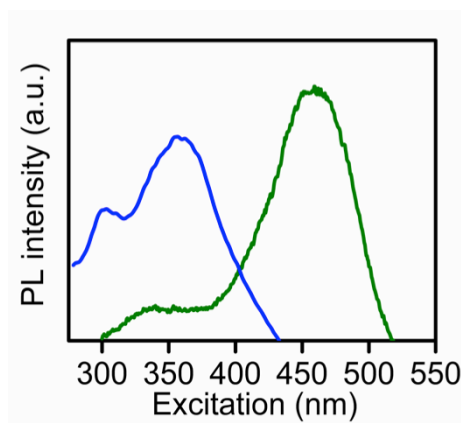


Figure 3-6: Photoluminescence excitation spectrum of blue PEDOT-Pdots suspended in water (emission at 450 nm) and green PEDOT-Pdots suspended in DMF (emission at 533 nm).

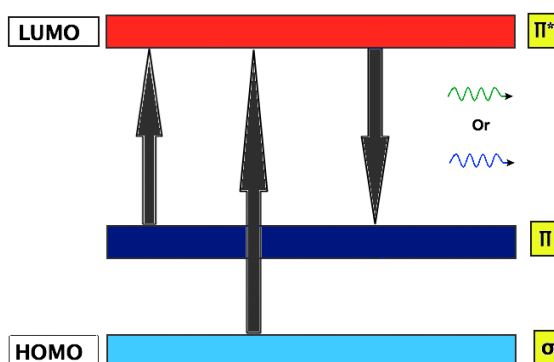


Figure 3-7: Schematic for electronic transitions of PEDOT-Pdots.

Organic fluorophores, such as FITC, bleach quickly under confocal imaging (Figure 3-4d). Remarkably, no bleaching was observed from both PEDOT-Pdots after long-term imaging. Intriguingly, the green-dots (in DMF) significantly increase the fluorescence intensity under illumination. Furthermore, the photo-bleaching studies performed over 2 h using a spectro-fluorometer indicate a similar behavior except that the PL of blue-dots decreases slightly (Figure 3-8). It is conceivable that laser annealing further improves the crystalline structure of PEDOT-Pdots.¹⁵⁴ The green-dots in DMF and blue-dots in water have a quantum yield of 13% (using Rhodamine 6G as the reference) and 4% (using quinine sulfate as the reference), respectively.

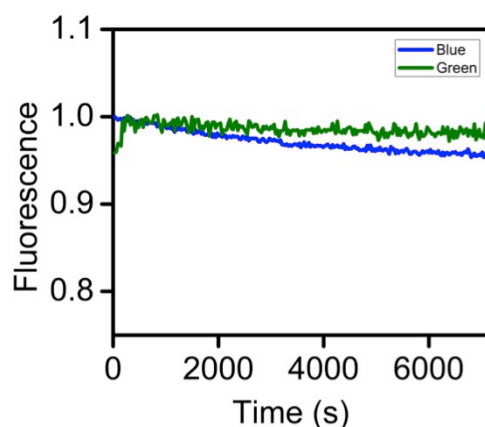


Figure 3-8: Photobleaching studies of the PEDOT-Pdots (blue and green) using a spectro-fluorometer. The fluorescence intensities are normalized to the maximum. A LS-55 fluorescence spectrometer (PerkinElmer) using the inbuilt light source (Xenon lamp) is used. PEDOT-Pdots in either DMF or water (200 $\mu\text{g/mL}$) are added in a quartz cuvette for measurements. The fluorescence intensity over time is recorded continuously at 460 nm (for green QDs in DMF) or 360 nm (for blue QDs in water).

Furthermore, the two-photon excited photoluminescence (TPPL) of the PEDOT-Pdots was examined. TPPL offers unique advantages over conventional one-photon excitation, including larger penetration depth into the tissue and higher signal-to-noise ratio benefiting from the longer excitation wavelength and nonlinear absorption process.¹⁵⁵ The PEDOT-Pdots exhibit strong emission under two-photo excitation (800 nm, even at relatively low intensities of 6.7 GW/cm^2) (Figure 3-9a). The two-photon excitation process is clearly evidenced by the nearly quadratic excitation intensity dependence of the PL signals in the corresponding log-log plot of the PL signals versus excitation intensity (Figure 3-9b).¹⁵⁶ An outstanding photo-stability under two-photon excitation was demonstrated with the retention of >90% of the initial emission after ~ 50 min, when operated at a pumping intensity of 20.1 GW/cm^2 (Figure 3-9c). The molecular size and remarkable photostability of PEDOT-Pdots under both single and two-photon excitation promises their applications as fluorophores for cellular imaging. Furthermore, the PEDOT-Pdots were unable to induce significant cytotoxic

effects at high concentrations (150 $\mu\text{g/mL}$), indicating good biocompatibility (Figure 3-10).

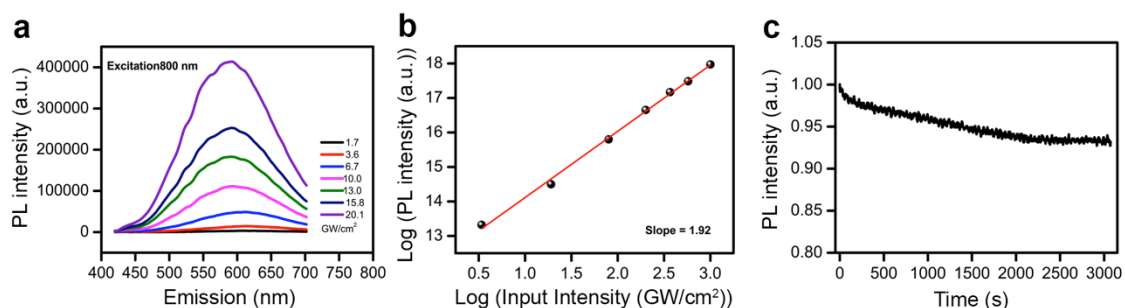


Figure 3-9: Two-photon characterization of PEDOT-Pdots in DMF: (a) Excitation intensity dependent PL spectra at an excitation wavelength of 800 nm, using a femtosecond amplified-pulsed laser with a repetition rate of 1000 Hz and pulse-width of 100 fs¹⁵⁵. (b) Log-log plot of the PL signals versus excitation intensity. The nearly quadratic excitation intensity dependence of the PL signals clearly demonstrates the two-photon excitation process¹⁵⁶ (c) Photostability of the PEDOT-Pdots in a small droplet under two-photon excitation (800 nm), with a pumping intensity of 20.1 GW/cm^2 .

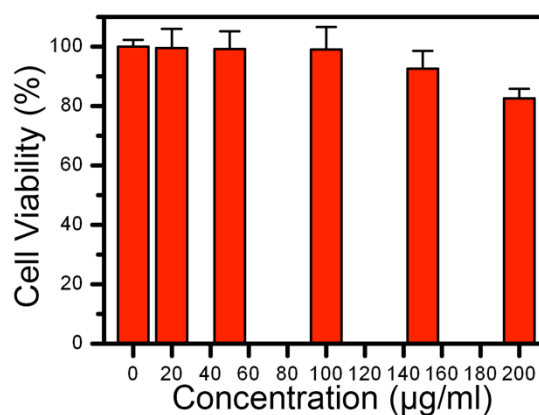


Figure 3-10: Cell viability and proliferation assay of PC12 cells incubated with different concentrations of PEDOT-Pdots.

3.2.4 Cellular imaging using PEDOT-Pdots

Interestingly, diluting the DMF-suspended green-dots in water (95% dilution) showed an absence of PL shift, rather their green fluorescence properties were preserved suggesting the persistent association between DMF molecules and PEDOT-Pdots (Figure 3-11). As a proof-of-concept demonstration for cellular imaging, we incubated PC12 cells with water suspended blue-dots (76.6 $\mu\text{g/mL}$) and DMF-associated green-dots diluted in cell culture medium (5.5 $\mu\text{g/mL}$) for 24 hr. As shown in Figure 3-12, both types of PEDOT-Pdots showed significant cell uptake. The biocompatible PEDOT-Pdots appear to be selectively located within the early endosomes, labeled by the fluorescent early endosome marker (mRFP-Rab5).

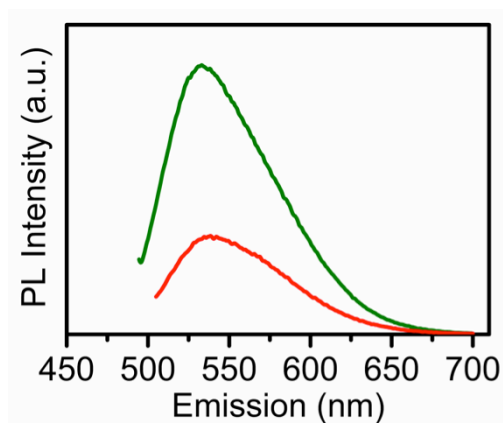


Figure 3-11: PL (excited at 488 nm) of PEDOT-Pdots in DMF (green curve) and in water (5% original dispersion in DMF is diluted in water) (red trace).

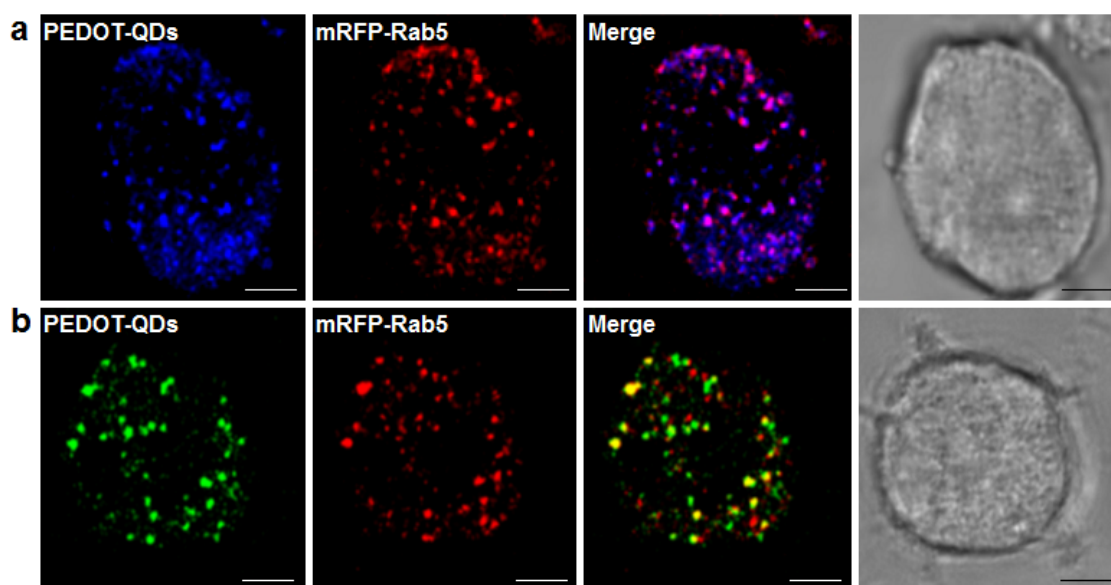


Figure 3-12: Confocal imaging of PC12 cells after 24 h incubation with blue (a) or green (b) PEDOT-Pdots. Confocal images with staining of QDs (column 1), endosome marker mRFP-Rab5 (column 2). Column 3 is the merged image of column 1 and 2. Column 4 shows the bright-field image of the cells. Scale bar = 5 μ m.

3.2.5 Optical detection of mercury ions (Hg^{2+}) using PEDOT-Pdots

Similar to other synthetic quantum dots^{8, 148, 157}, the small PEDOT-Pdots promise wide applications in optical sensing of bio-medically toxic metal ions. As the proof-of-concept demonstration, we show here that the photoluminescence (PL) of PEDOT-Pdots can be significantly quenched by 57% upon addition of 100 μM Hg^{2+} ions whereas the PEDOT-Pdots are not obviously responsive to other metal ions (Pb^{2+} , Zn^{2+} , Cd^{2+} , Cs^+ , Mg^{2+} , Co^{2+} , Ni^{2+} , Mn^{2+} , K^+ and Au^{3+}) (Figure 3-13a). PL quenching by Hg^{2+} is dose-dependent (Figure 3-13b), and as shown in Figure 3-13c, the extrapolated lower theoretical detection limit is as low as 0.87 μM (with S/N = 3) and the linear response is up to 10 μM .

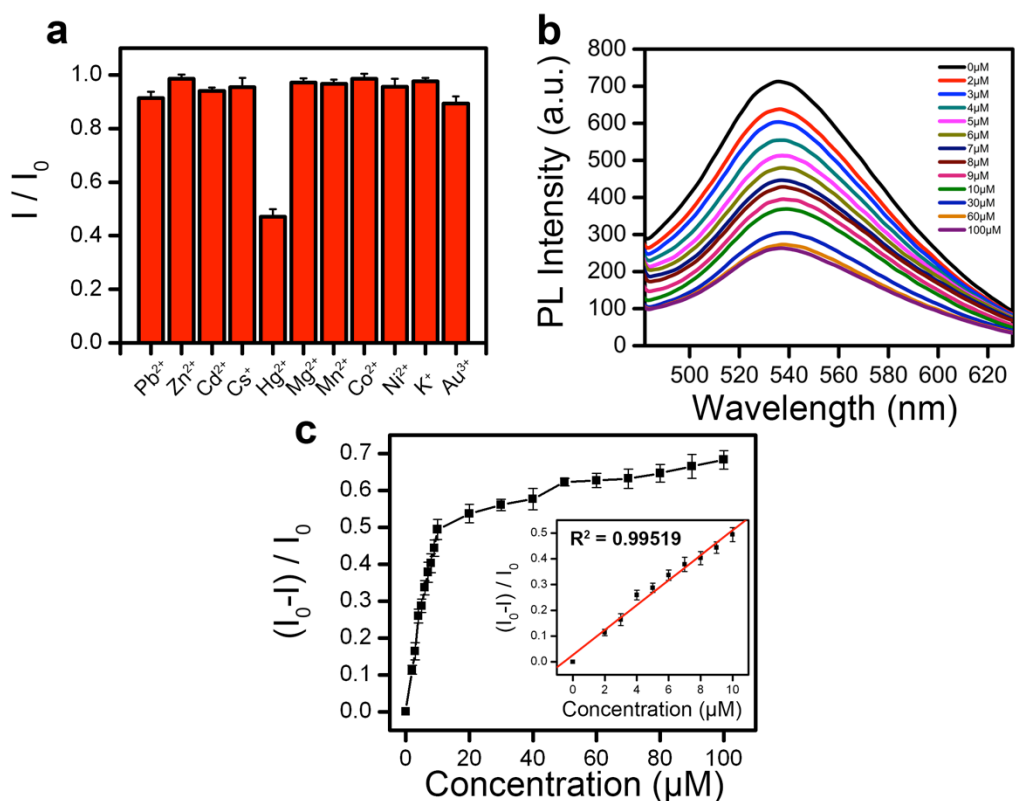


Figure 3-13: Sensitive and selective optical detection of Hg^{2+} ions. (a) PL of PEDOT-Pdots (200 μ g/mL in water) is selectively quenched by Hg^{2+} (100 μ M), but not other metal ions at the concentration (b) The PL emission spectra of PEDOT-Pdots with various concentrations of Hg^{2+} (c) The relative concentration-dependent fluorescence response of PEDOT-Pdots. Inset shows the linear response range. The error bars represent the standard deviation of the measurements from three different samples.

It has been previously reported that nitrogen-containing imidazole¹⁵⁸ and sulfur-containing thiophene,¹⁵⁹⁻¹⁶⁰ can bind with Hg^{2+} with high affinity. Therefore, Hg^{2+} ions act as a coordinating center to bridge several PEDOT-Pdots together, by interacting with thiophene groups from PEDOT and imidazole groups from BMIM⁺ associated with PEDOT-Pdots *via* π - π interactions. In turn, fluorescence quenching occurs due to aggregation of QDs. Indeed, Hg^{2+} -induced Pdots aggregations are observed under AFM (Figure 3-14).

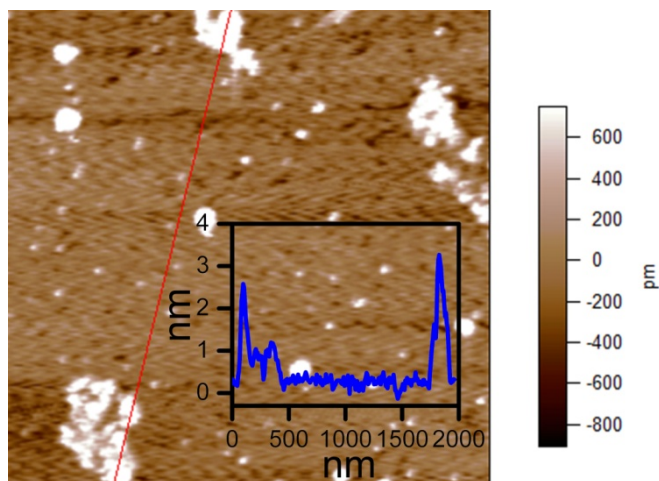


Figure 3-14: AFM image of Hg^{2+} -induced PEDOT-Pdot aggregates.

A future direction in this work would involve understanding the precise chemistry behind the Hg^{2+} -induced PEDOT-Pdots aggregation formation would allow us to tailor the PEDOT-Pdots and render a greater degree of control over the sensitivity of the system. Recent studies suggest that,¹⁶⁰ whilst the precise coordination chemistry behind thiophene - Hg^{2+} based coordination bonds is still unclear, selectivity can be significantly improved by functionalizing the thiophene ring with moieties such as pyridine. This would help in improved coordination bond formation at lesser concentrations, conversely improving sensitivity resulting in improved Hg^{2+} sensors.

3.3 Conclusion

In conclusion, we have developed a facile and general strategy to synthesize novel fluorescent polymer quantum dots derived from non-fluorescent PEDOT. Such molecularly light, perfectly photo-stable PEDOT-Pdots promise a wide range of applications in biomedical settings such as; bio-imaging (e.g., single molecule tracking in live cells) and sensitive optical detection. In principle, the synthetic route demonstrated here can be easily modified (e.g., using different polymer precursors,

ionic liquids for polymerization, solvents) to produce different types of polymer QDs with various interesting properties.

This chapter (including phrases and figures) is adapted / reproduced with permission from our published journal article “Fluorescent quantum dots derived from PEDOT and their applications in optical imaging and sensing. *Materials Horizons*, 2014, 529-534. Copyright 2014, The Royal Society of Chemistry”

Chapter 4

4. Synthesis of Polymer Dots from Polythiophene for Imaging Endocytic Compartments in Live Cells

Developing fluorophores of high brightness and photostability is an ongoing challenge. As discussed before fluorescent quantum dots or nanoparticles derived from semiconducting polymers (Pdots), owing to their unique properties such as high brightness, tunable and non-blinking emission, broad absorption, high photo-stability, biocompatibility, and molecular size are of considerable interest as alternative fluorophores.¹⁶¹⁻¹⁶²

As reviewed in Chapter 2, the Pdots are synthesized using bottom-up chemical synthesis or post-polymerization techniques, and often show high quantum yields depending on the type of polymer used. The quantum yields are often upto 20%, with few groups reporting upto 50%.²⁶ In Chapter 3 we have developed and discussed an alternative electrochemical-ultrasonication based synthesis strategy to produce a new type of crystalline Pdots from non-fluorescent poly(3,4-ethylenedioxythiophene) for cellular imaging applications. It is known that the low quantum yields in conjugated polymers are dependent on their conjugation lengths, conformational changes and faster non-radiative recombination.¹⁶³⁻¹⁶⁴ The presence of bulky groups reduces the effective conjugation length.

In this chapter, we synthesize new polymer dots derived from poly (2,2'-Bithiophene) by modifying the strategy discussed in the previous chapter. The properties of the thus synthesized pTh-Pdots, derived from a thiophene based semiconducting polymer including physical, chemical and optical properties are investigated. Furthermore, these polythiophene-based Pdots (pTh-Pdots) exhibit negative solvatochromism, i.e.,

blue shift in photoluminescence (PL) emission with increasing solvent polarity. Studies are conducted to investigate the potential of these pTh-Pdots for cellular imaging and endocytic tracking using their unique solvatochromic behavior.

4.1 Materials & Methods

4.1.1 Preparation of Polythiophene (pTh) film

2,2'-bithiophene (BTh) monomer, ionic liquids (1-n-butyl-3-methylimidazolium tetrafluoroborate - BMIMBF₄; 1-butyl-3-methylimidazolium methyl sulphate – BMIMMeSO₄) were purchased from Sigma Aldrich.

Using 0.1M BTh monomer in the ionic liquid BMIMBF₄, the Poly (2,2'-bithiophene) (pTh) film (to be referred as polythiophene hence forth) was electro-polymerized onto an ITO working electrode held at the constant potential of 5 V for 45 minutes. Electro-polymerization was done using a standard three-electrode configuration consisting of a platinum plate (counter) electrode, silver wire (reference) electrode and indium tin oxide (ITO) (working) electrode on an electrochemical workstation (CHI 660D). Overnight drying in a 37 °C vacuum oven was done after extensive post-polymerization washing to eliminate excess ionic liquid and unreacted monomers. Polymer films using different ionic liquids such as BMIMMeSO₄ were prepared for optimization studies.

4.1.2 Preparation of polymer dots (Pdots)

The dried pTh polymer film was gently scraped off the ITO electrode and suspended in THF (Tetrahydrofuran, Sigma Aldrich) solvent at 1 mg/ml concentration, followed by exfoliation with ultrasonication (Branson 2510; 1.1 A, 230 W) at 27 °C for 1 h. The suspension formed, was then filtered using a WHATMAN 0.2 µm PTFE filter to

obtain a clear yellow solution. Eventually, the THF was extracted using a rotary evaporator (Heidolf) at 30 °C.

The dried aggregates were subsequently re-suspended in DMF (N,N-Dimethylformide, Sigma Aldrich) or distilled water following which the polythiophene-based Pdots (pTh-Pdots) suspensions were further purified. pTh-Pdots in DMF (green pTh-Pdots) were purified by syringe filtration through a 0.1 µm PTFE filter. On the other hand, the pTh-Pdots in water (blue pTh-Pdots) were ultra-filtered (molecular cut-off weight of 3 KDa) followed by filtration through a 0.1 µm nitrocellulose membrane to remove the aggregates. Both the green pTh-Pdots and blue pTh-Pdots were highly stable (lasting for months without apparent aggregation). Furthermore, aprotic volatile solvents such as THF appeared to be suitable for high yield exfoliations in contrast to solvents like ethanol and water, which showed little to no exfoliation.

4.1.3 Characterization

Similar to chapter 3, the samples were characterized using Field emission scanning electron microscopy (FESEM), Atomic force microscopy (AFM), High-resolution transmission electron microscopy (HRTEM, JEOL JEM 2100F TEM), Fourier transform infrared spectroscopy (FTIR), and X-ray photoelectron spectroscopy (XPS, Kratos Axis Ultra^{DLD} spectrometer from Kratos Analytical Ltd; equipped with a monochromatized Al K α X-ray source). Optical characterization included UV-Vis absorption and photoluminescence (PL) studies. Further details of the instruments used can be found in the previous chapter.

4.1.4 Cell imaging

The HeLa cells (human epithelial carcinoma cell line; American Type Culture Collection) were cultured in DMEM (Life Technologies) supplemented with 10% fetal

bovine serum and 1% penicillin–streptomycin, at 37 °C in a humidified atmosphere containing 5% CO₂ and 95% air. Before the confocal imaging, the cells were incubated for 1-3 h with pTh-Pdots originally stocked in DMF (5 µg/ml), pTh-Pdots originally stocked in water (50 µg/ml), or LysoTracker Red DND-99 (100 nM; Life Technologies). In some experiments, the cells were transfected with mRFP-Rab5 (Addgene) using Lipofectamine3000 (Life Technologies), 1 - 2 days before incubation with pTh-Pdots. Confocal images were taken using a LSM710 confocal laser-scanning microscope (Carl Zeiss, Germany) using excitation at 405 nm, 488 nm, or 580 nm.

4.1.5 Viability Assay

The cell viability were determined using a 3-(4,5-dimethylthiazol-2-yl)-2,5-diphenyl tetrasodium bromide (MTT) based cell growth determination kit (Sigma-Aldrich). Briefly, after washing with phosphate buffer saline (PBS), the cells were incubated in the culture medium containing MTT reagent solution (5 mg/ml MTT in DMEM without phenol red) (10% v/v) for 4 h at 37 °C. MTT solvent (0.1 N HCl in anhydrous isopropanol) is then added to the culturing well (50% v/v), followed by measuring the absorbance of MTT formazan crystals at 570 nm using a Victor3 plate reader (PerkinElmer).

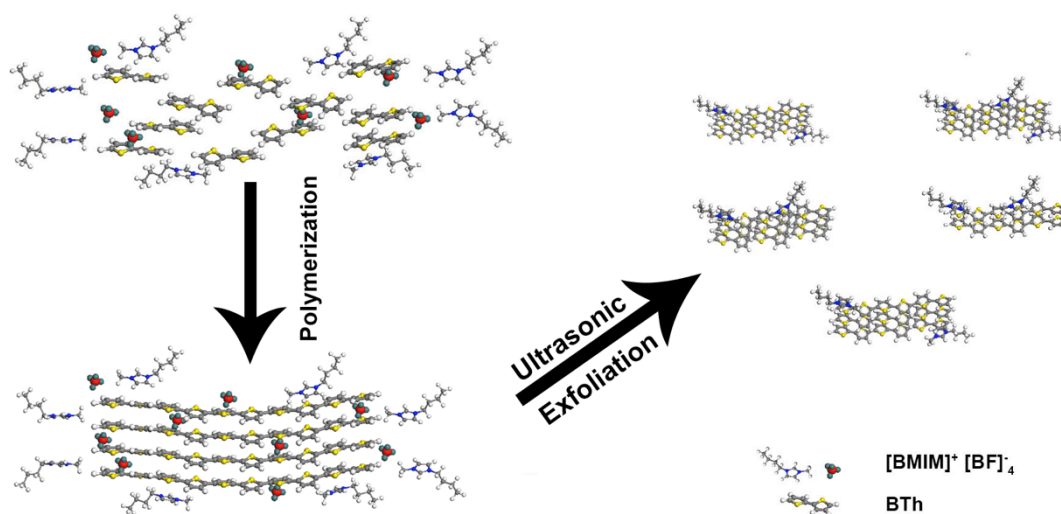
4.1.6 Liposome Preparation

The pure liposomes and pTh-Pdots incorporated liposomes are synthesized using the thin film hydration method.¹⁶⁵ Briefly, DMF from the DMF suspension of pTh-Pdots was extracted in a rotary evaporator at 80 °C under a reduced pressure (11 mbar). 5 mg of the phospholipid 1,2-dipalmitoyl-*sn*-glycero-3-phosphocholine (DPPC, Sigma Aldrich) was dissolved in chloroform and mixed with dried pTh-Pdots. Subsequently, chloroform was extracted at 37 °C under a reduced pressure (474 mbar) in the rotary

evaporator to give a thin lipid film. The thin film was subsequently hydrated at 45 °C, by adding 2 mL DI water. Finally, the free pTh-Pdots and free lipids were removed by ultracentrifugation (molecular weight cut-off 50 KDa).

4.2 Results and Discussion

4.2.1 Synthesis and characterizations



Scheme 4-1 Schematic illustration of pTh-Pdot synthesis.

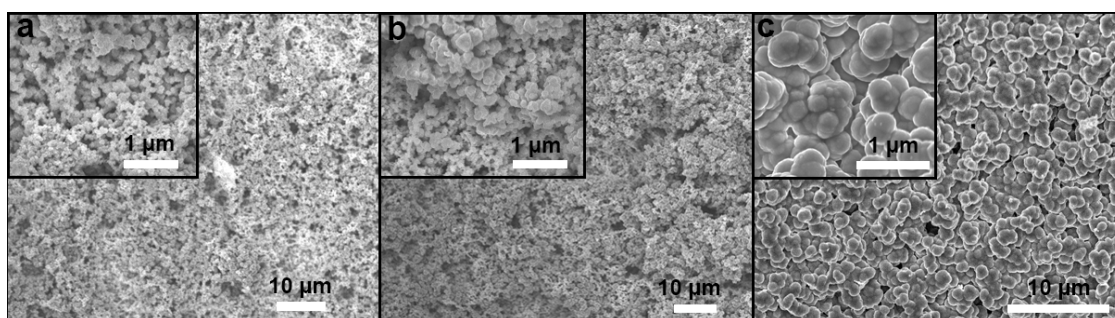


Figure 4-1: Field-effect scanning electron microscopy (FESEM) of pTh films obtained after (a) 30 min, (b) 45 min and (b) 60 min electropolymerization of 2,2'-bithiophene monomers. Insets show the magnified views.

As schematically illustrated in Scheme 4-1, polythiophene (pTh) is initially electropolymerized from 2,2'-bithiophene (BTh) monomers in ionic liquid BMIMBF₄,

to form a thin film on the ITO electrode surface. The BMIMBF₄ was used because of its wide electrochemical working window, excellent ionic conductivity and low volatility.¹⁶⁶ As seen from the Field effect scanning electron microscopy (FESEM), the pTh film consists of micro-granules whose size are linearly dependent on the polymerization time (Figure 4-1). Subsequently, pTh-Pdots are readily exfoliated from pTh film by ultrasonication in anhydrous tetrahydrofuran (THF), yielding a yellowish homogenous suspension. Afterwards THF is completely extracted using rotary evaporation and the dried pTh-Pdots are re-suspended in either dimethylformamide (DMF) or deionized water.

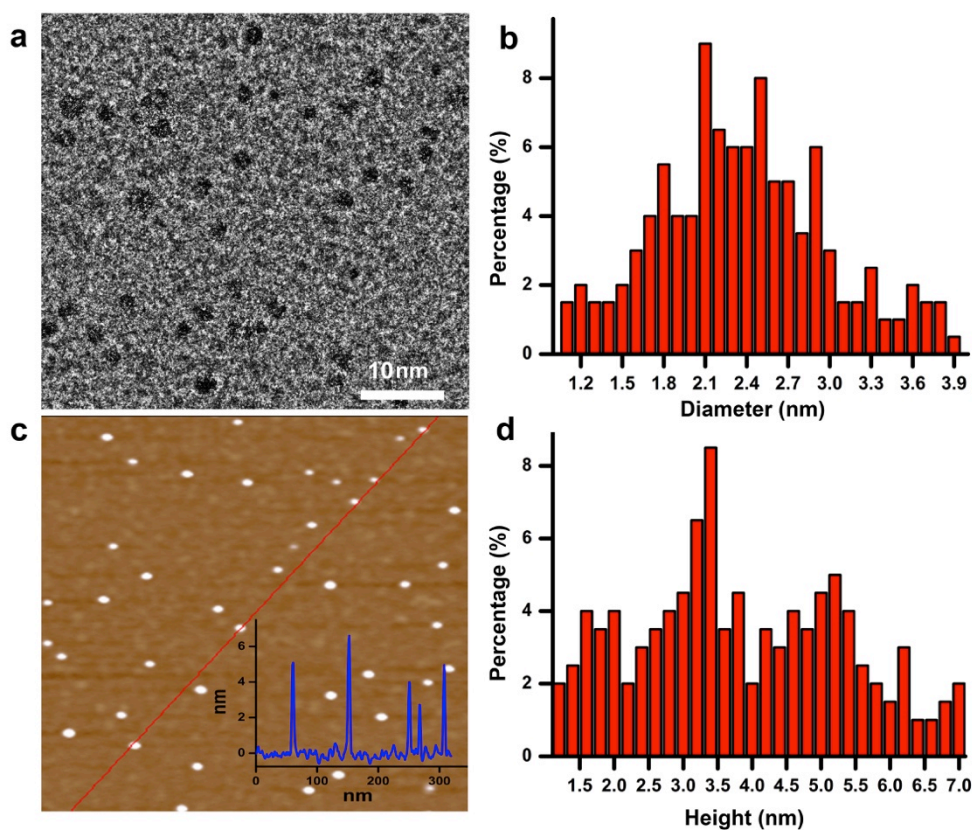


Figure 4-2: (a) High-resolution TEM image of pTh-Pdots. (b) Diameter distribution ($n = 200$). (c) AFM image of pTh-Pdots. Inset shows the height profile along the indicated line. (d) Height distribution ($n = 200$).

High-resolution transmission electron microscopy (HRTEM) reveals that the average diameter of pTh-Pdots is 2.37 ± 0.47 nm ($n = 200$) (Figure 4-2a and 4-2b). Atomic

force microscopy (AFM) shows that the average thickness of pTh-Pdots is $3.83 \text{ nm} \pm 0.73 \text{ nm}$ ($n = 200$), corresponding to ~ 3 layers of pTh (Figure 4-2c and 4-2d).¹⁶⁷⁻¹⁶⁸ The spectrum of Fourier transform infrared spectroscopy (FTIR) of pTh-Pdots exhibits the stretching peaks for thiophene ring (1385 cm^{-1}), C-H (1124 cm^{-1}), C-O (1084 cm^{-1}) and C-S (697 cm^{-1}), which are characteristic to pTh (Figure 4-3a).^{150, 169} The triplet peaks of C-H asymmetric and symmetric vibration (at 2962 , 2921 , and 2852 cm^{-1}) originate from the alkyl groups of BMIM⁺ molecules adsorbed onto pTh-Pdots.^{148, 170}

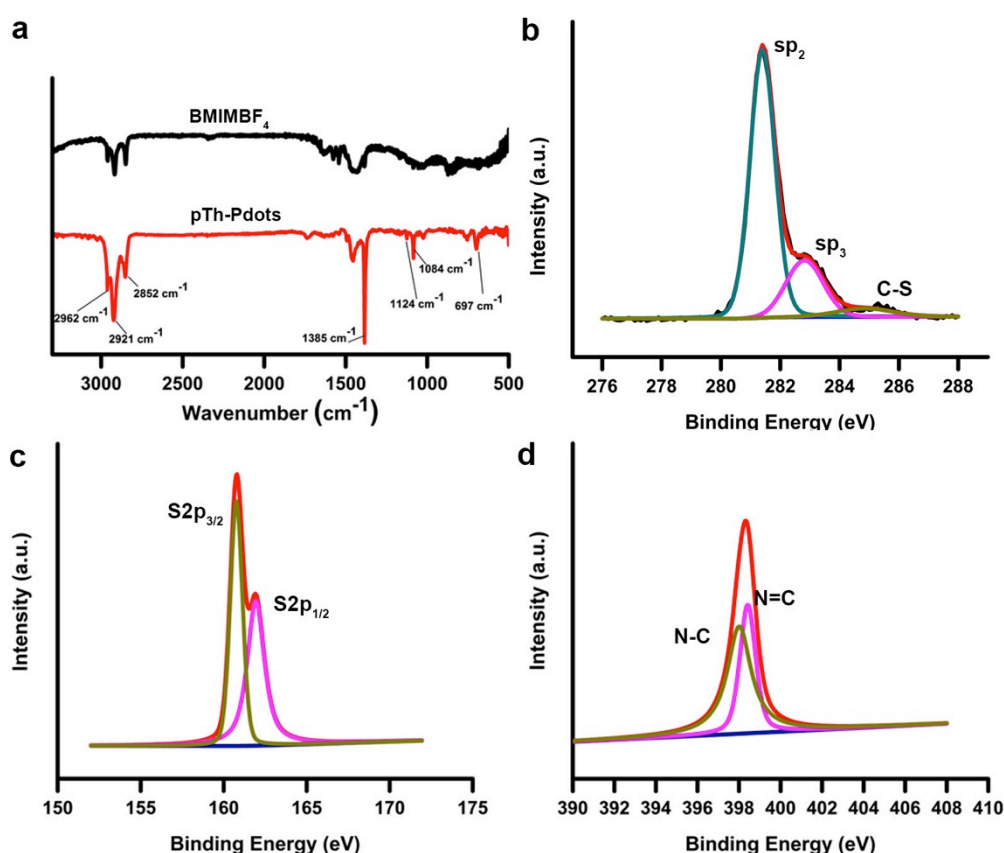


Figure 4-3: (a) Spectra of Fourier transform infrared spectroscopy (FTIR) for pTh-Pdots and BMIMBF₄. (b-d) High-resolution C1s (b), S2p (c), and N1s (d) X-ray photoelectron spectroscopy (XPS) spectra of pTh-Pdots.

Also characteristic to pTh, the X-ray photoelectron spectroscopy (XPS) shows the high-resolution C1s and S2p spectrums are deconvoluted into the sp² (C=C), sp³ (C-C), C-S peaks, and the S2p_{3/2} & S2p_{1/2} peaks, respectively (Figure 4-3b and 4-3c).¹⁷¹⁻

¹⁷² The N-C and N=C peak in the high-resolution N1s spectrum are a result of the imidazole moiety from BMIM⁺ (Figure 4-3d).¹⁷³⁻¹⁷⁴ Presumably, BMIM⁺ facilitates the exfoliation and dispersion of Pdots through π - π interaction with pTh.¹⁷⁵ We found that compared to other ionic liquids such as 1-Butyl-3-methylimidazolium methyl sulphate (BMIMMeSO₄) and tetra ethyl ammonium chloride (TEAC), the amphiphilic BMIMBF₄ offers the highest yield of pTh-Pdots.

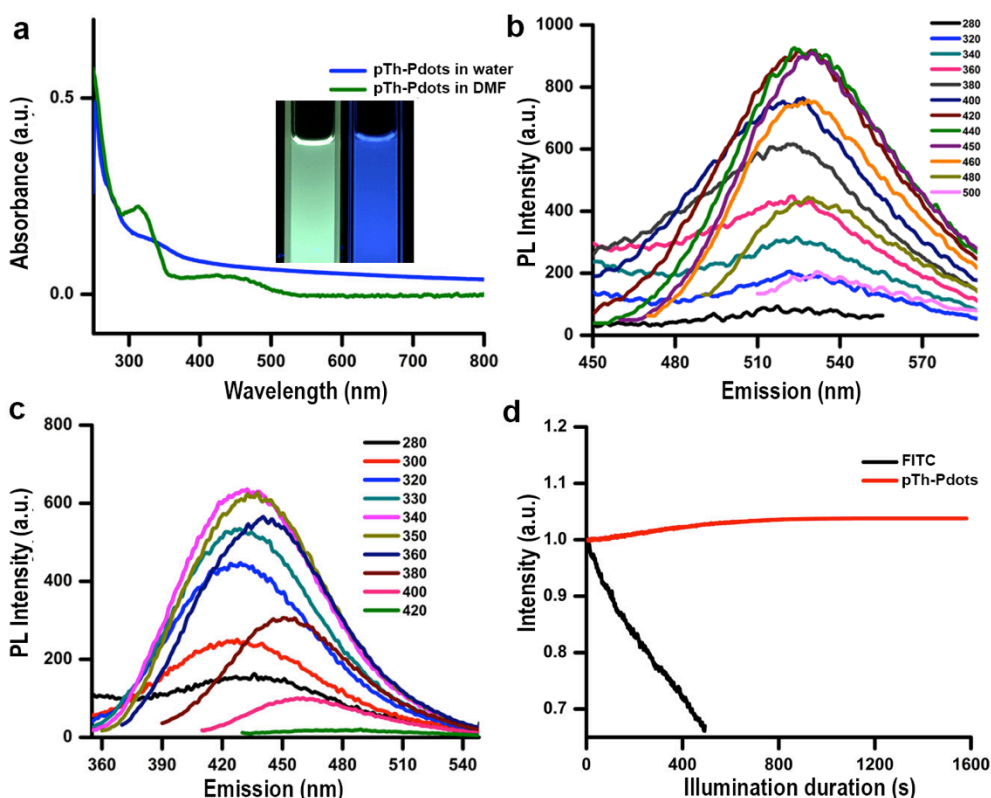


Figure 4-4: (a) UV-Vis spectra of pTh-Pdots in DMF and pTh-Pdots in water. Inset shows the optical images with UV illumination at 365 nm. (b) PL emission spectra of pTh-Pdots in DMF at different excitation wavelengths. (c) PL emission spectra of pTh-Pdots in water, (d) Photo-bleaching of FITC dye molecules and pTh-Pdots under confocal imaging.

Due to its amphiphilic property, BMIM⁺ assists pTh-Pdots in dispersing well in both water and organic solvents with no obvious aggregation for months (inset of Figure 4-5).¹⁷⁵⁻¹⁷⁶ Interestingly, pTh-Pdots in DMF appear green while they fluoresce blue in water under 365 nm UV illumination (Figure 4-4a, inset). It suggests that pTh-Pdots

have negative solvatochromism, i.e., blue shift in PL emission with increasing solvent polarity. Both pTh-Pdot suspensions can efficiently absorb UV light (Figure 4-4a).

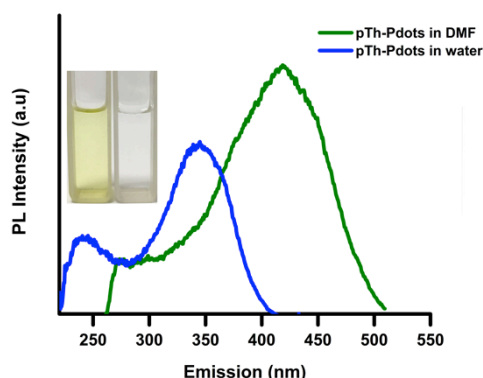


Figure 4-5: PL excitation spectra of pTh-Pdots in DMF (emission at 530 nm) and pTh-Pdots in water (emission at 435 nm), respectively. Inset shows the brightfield images of pTh-Pdots in DMF and water, respectively.

The excitation spectra for both suspensions exhibit two peaks resulting from π to π^* and σ to π^* transitions (Figure 4-5).¹⁷⁷ The maximum emission peaks for green pTh-Pdots in DMF and blue pTh-Pdots in water are achieved at ~ 530 nm (excited by 440 nm) and ~ 435 nm (excited by 340 nm), respectively (Figure 4-4b and 4-4c). In comparison, 2,2'-bithiophene monomer at the concentration (dissolved in DMF; not soluble in water) does not exhibit any apparent light absorption or PL emission. PL quantum yields (QY) for the green pTh-Pdots in DMF and blue pTh-Pdots in water are calculated to be 44% (using R6G as reference) and 10% (using quinine sulfate as reference) respectively. The high quantum yields may be attributed to the effect of backbone chain lengths on quantum yields observed in α -oligothiophenes.¹⁷⁸

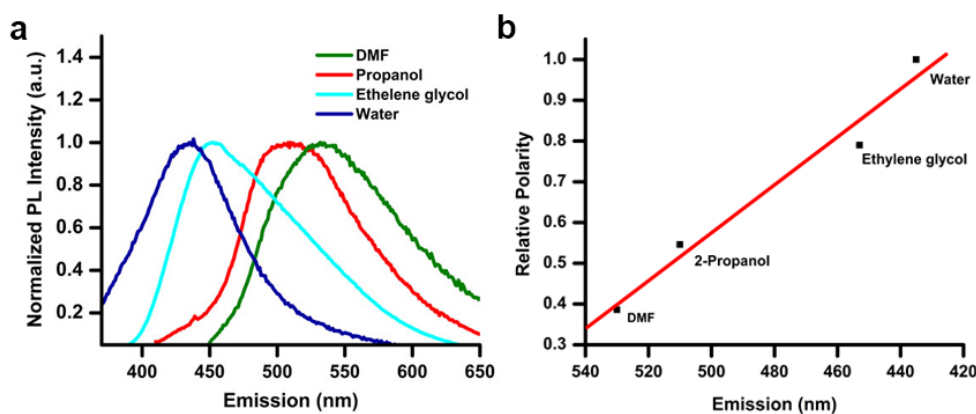


Figure 4-6: (a) PL intensity of pTh-Pdots suspended in solvents with varying polarity. (b) Linear relationship between PL emission peak and relative polarity.¹⁷⁹

Negative solvatochromism of pTh-Pdots is presumably due to intra-molecular conformational changes in the conjugated backbone in the solvents of varying polarity.¹⁸⁰ As seen in Figure 4-6, the emission of pTh-Pdots undergoes a blue shift with increasing solvent polarity (DMF, propanol, ethylene glycol, water). The blue shifting of the emission peak exhibits an approximately linear relation with the increasing relative polarity of the solvent. Based on that observation, the pTh-Pdots may see future applications as a sensor to report changes in polarity. Consistently (Figure 4-7a), addition of 90% water to pTh-Pdots suspension in DMF results in a predominantly blue-shifted emission (green to blue). On the other-hand, addition of 50% water to pTh-Pdots suspension resulted in both blue (excited at 340 nm) and green (excited at 440 nm) emissions (Figure 4-7b).

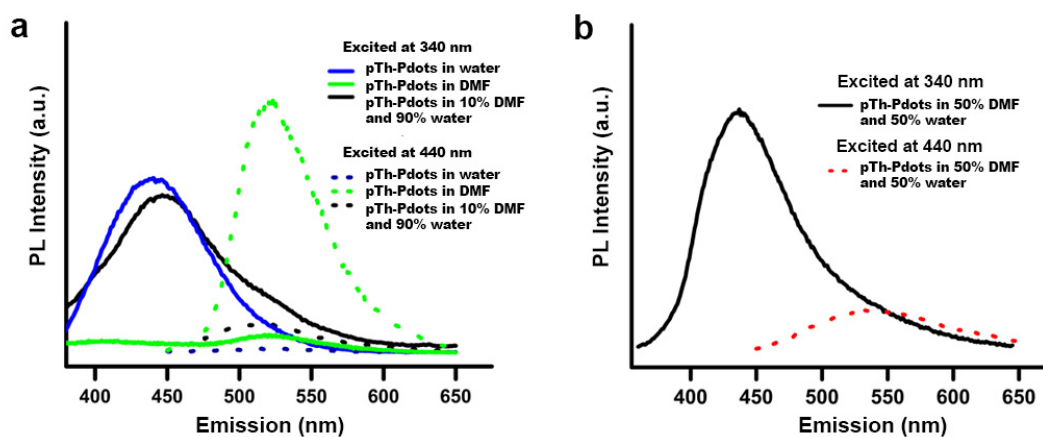


Figure 4-7: (a) PL of pTh-Pdots in water, pTh-Pdots in DMF, and DMF suspension of pTh-Pdots (10%) diluted in water (90%). (b) PL of DMF suspension of pTh-Pdots (50%) diluted in water (50%).

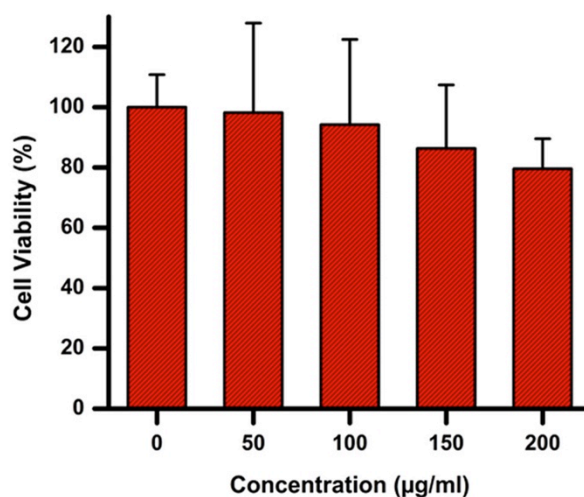


Figure 4-8: MTT assay of HeLa cells after overnight incubation with pTh-Pdots at various concentrations.

The use of organic fluorophores (e.g., FITC) for bioimaging is often plagued by their poor photo-stability, i.e., their fluorescence is quickly bleached under confocal laser illumination (Figure 4-4d). In contrast, no obvious photobleaching of pTh-Pdots is observed under confocal imaging. Photobleaching of organic fluorophores is due to cleaving of covalent bonds or reactions with surrounding molecules or radicals. The high photo-stability of pTh-Pdots suggests their high photochemical stability. Moreover, even at the concentrations (e.g., 100 $\mu\text{g/ml}$) much higher than needed for

bioimaging (typically a few $\mu\text{g/ml}$), pTh-Pdots do not exert apparent cytotoxic effects to animal cells (Figure 4-8). Taken together, the high brightness, excellent photostability, good biocompatibility, and small size of pTh-Pdots are desirable properties for bioimaging.

4.2.2 pTh-Pdots for cellular imaging

As a proof-of-concept demonstration, we herein used pTh-Pdots for cellular imaging of HeLa cells. Although green pTh-Pdots suspended in DMF turn blue after being diluted in bulk aqueous medium (Figure 4-7), as compared to blue pTh-Pdots stocked in water, they can be more easily internalized by the cells (compare Figure 4-9 and Figure 4-10). This is likely due to the residual DMF molecules attached on pTh-Pdots, which facilitate and enhance the cell uptake.¹⁸¹

Therefore, in the following bioimaging experiments, we used pTh-Pdots originally stocked in DMF (i.e., DMF decorated pTh-Pdots). As shown in Figure 4-10, after 1h incubation with pTh-Pdots (5 $\mu\text{g/ml}$), pTh-Pdots are easily taken up by the cells and appear blue.

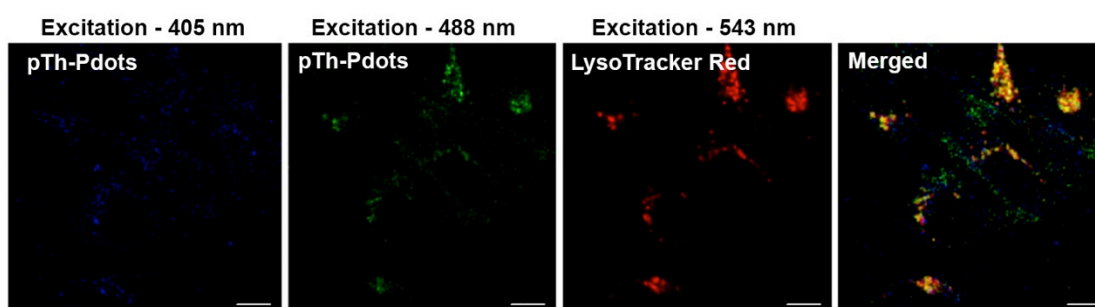


Figure 4-9: Confocal imaging of HeLa cells incubated with pTh-Pdots (water stock diluted in cell medium to 50 $\mu\text{g/ml}$) for 3 h, and co-localization study with lysosome marker (LysoTracker Red).

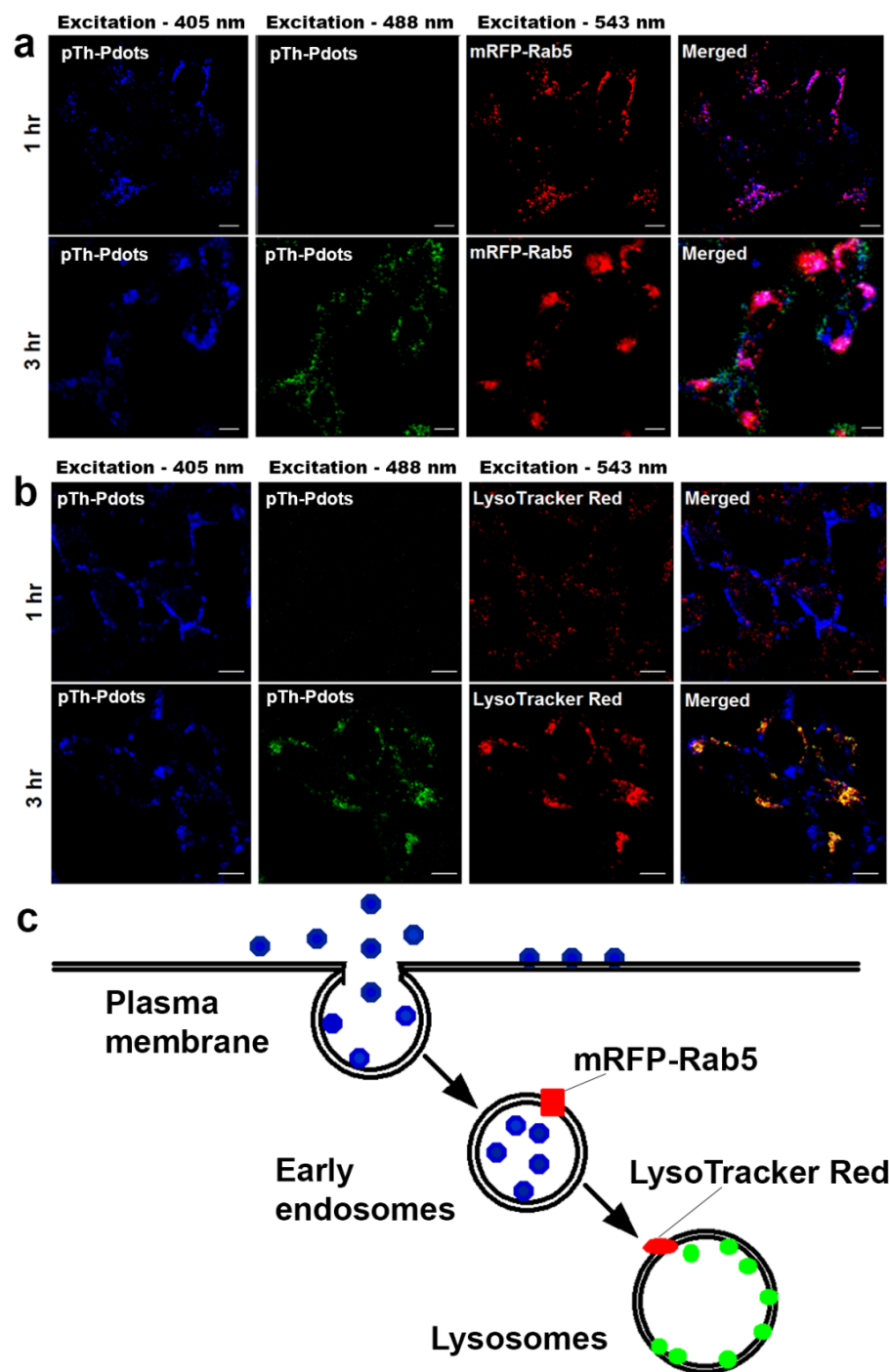


Figure 4-10: Confocal imaging of HeLa cells incubated with pTh-Pdots (DMF stock diluted in cell medium to 5 $\mu\text{g/ml}$) for 1 and 3 h, respectively. (a) Co-localization with early endosome marker (mRFP-Rab5). (b) Co-localization with lysosome marker (LysoTracker Red). (c) Schematic for endocytosis uptake of pTh-Pdots. Scale bar = 10 μm

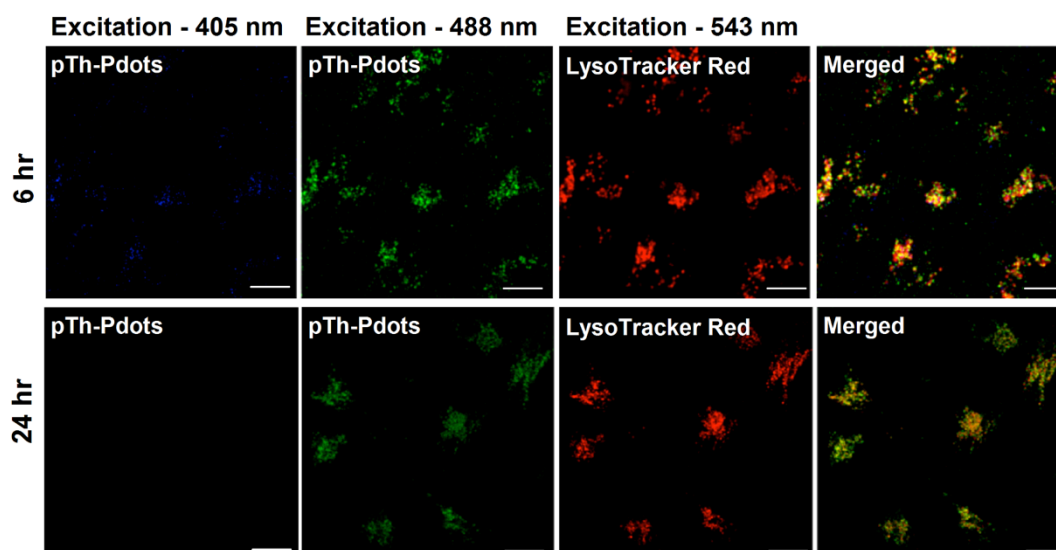


Figure 4-11: Confocal imaging of HeLa cells incubated with pTh-Pdots (DMF stock diluted in cell medium to 5 $\mu\text{g/ml}$) for 6 h and 24 h, and co-localization study with lysosome marker (LysoTracker Red). (Scale bar = 10 μm)

Apparently, these pTh-Pdots are segregated in the early endosomes after being endocytosed as suggested by the significant co-localization with an early endosome marker mRFP-Rab5. Interestingly, after 3h incubation, in addition to blue pTh-Pdots in early endosomes, green pTh-Pdots also appear inside the cells. Evidently, these green pTh-Pdots stain lysosomes (but not early endosomes) because they are essentially co-localized with lysosome marker LysoTracker Red (Figure 4-10). These experiments demonstrate that pTh-Pdots can be employed to specifically label two distinct compartments (early endosomes and lysosomes) residing in the early and late endocytic pathway, respectively. As shown in Figure 4-11, after 6h most of pTh-Pdots go to lysosomes and after 24h all of them reach lysosomes. Taken together, pTh-Pdots migrate from early endosomes to lysosomes over time.

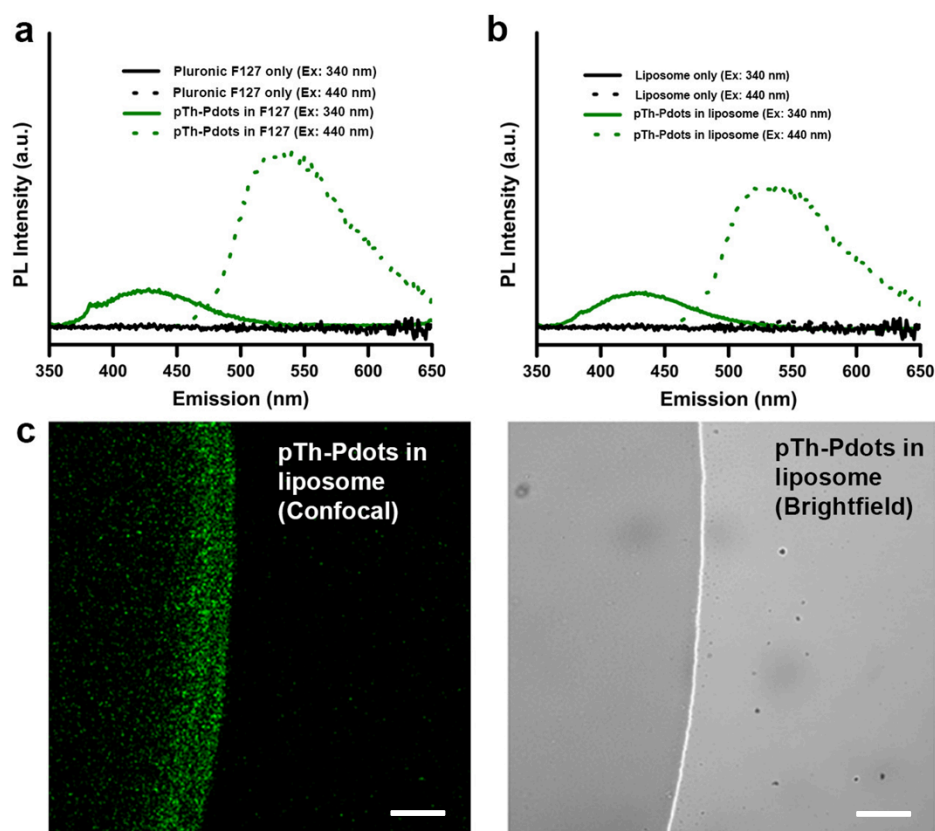


Figure 4-12: (a) PL spectra of Pluronic F127 polymer and pTh-Pdots encapsulated by Pluronic F127, excited at 340 or 440 nm. (b) PL spectra of DPPC liposomes and liposomes incorporated with pTh-Pdots (originally stocked in DMF). (c) Confocal fluorescence image (left) and bright-field image (right) of a water droplet containing pTh-Pdots incorporated liposomes. The borderline between the droplet and the dry glass coverslip can be clearly seen in the bright-field image (bright line). In the fluorescence image, it is seen that liposomes are more concentrated at the edge. (Scale bar = 100 μ m)

We conceive that owing to its polarity-sensitive PL properties pTh-Pdots fluoresce blue in the aqueous endosome lumen whereas they turn into green in lysosome due to their insertion into the hydrophobic lysosomal membrane. As discussed earlier, although polythiophene (pTh) is highly hydrophobic, pTh-Pdots are well dispersed in aqueous solutions because of the attached BMIM⁺ moieties. It is possible that BMIM⁺ moieties are removed or destroyed while going through the early endocytic pathway or inside lysosomes, which are highly destructive due to the presence of various

degradative enzymes. As a consequence, the hydrophobic pTh-Pdots preferably intercalate into the lysosomal membrane. To directly support this hypothesis, we show that green pTh-Pdots originally stocked in DMF turn blue once being added to bulk water (Figure 4-7) whereas pTh-Pdots encapsulated by amphiphilic polymer Pluronic F-127 retain green fluorescence in water (Figure 4-12). This confirms that pTh-Pdots are green fluorescent in hydrophobic environment. We further show that pTh-Pdots incorporated into the lipid bilayers of artificial liposomes are green (Figure 4-12).

4.3 Conclusion

In summary, we have synthesized a new fluorescent polymer dot derived from non-fluorescent polythiophene (pTh-Pdots) by modifying a simple and high yield procedure. These pTh-Pdots are bright, photostable, biocompatible and small, therefore promising as fluorophores for bioimaging applications. Exploiting its negative solvatochromism property, we here demonstrate the use of pTh-Pdots in live cells to label and differentiate early endosomes and lysosomes, thus highlighting their use for tracking the endocytic pathway in *in vitro* settings.

This chapter (including phrases and figures) is adapted / reproduced with permission from our accepted journal article “Thiophene-derived polymer dots for imaging endocytic compartments in live cells and broad-spectrum bacterial killing. *Materials Chemistry Frontiers*, 2016, 152-157. Copyright 2016, The Royal Society of Chemistry.”

Chapter 5

5. Polymer dots as Broad Spectrum Antibacterial agents

Use and abuse of common antimicrobial agents over the years, has led to increasing cases of bacterial strains expressing multiple drug resistance (MDR).¹⁸² This is a major factor of concern in therapeutics, as using multiple drug combinations or increased dosages to fight simple infections raises the complexity of the treatment.¹⁸³ Over the past few decades, synthetic antimicrobial agents including polymers, quaternary ammonium compounds, semiconductor quantum dots (semi-QDs) have gained attention as alternatives to bactericidal agents like antibiotics.¹⁸⁴⁻¹⁸⁵ Silver nanoparticles and copper oxide (CuO) nanoparticles are some of the popular semi-QDs alternatives.¹⁸⁶ However as previously discussed in Chapter 2 these semi-QDs exhibit several intrinsic drawbacks including risks environmental pollution, complex chemical synthesis, high cost, biocompatibility issues and so forth.

π -Conjugated carbon based nanomaterials such as single walled carbon nanotubes (SWCNTs), fullerenes, graphene quantum dots are easily available and renewable alternatives that are comparatively cheaper, biocompatible & environmentally friendly.¹⁸⁷⁻¹⁸⁸ Furthermore they demonstrate tunable physical and surface properties resulting in high biocompatibility, specificity and good bactericidal behaviour.¹⁸⁹ However these nanomaterials often exhibit very high minimum inhibitory concentrations (MICs) for antibacterial activity.

As discussed in Chapter 4 we synthesized novel pTh-Pdots derived from poly(2,2'-bithiophene) and demonstrated its application as alternative fluorophores to organic dyes for tracking the endocytic pathway. With thiophene derivatives being known as good antibacterial agents and their use in antibiotics,¹⁹⁰⁻¹⁹¹ we speculate on such

potential of the pTh-Pdots (Scheme 5-1). We demonstrate the utility of nano-sized polymer dots as excellent anti-bacterial agents with low MICs for the first time, to the best of our knowledge. Interestingly, these pTh-Pdots further demonstrate superb peroxidase mimicking behaviour, and thereby tested for increased potency as anti-bacterial agents.

5.1 Materials & Methods

5.1.1 Synthesis and Characterization of pTh-Pdots

The synthesis, surface and chemical characterization of the pTh-Pdots has been discussed in detail in the Chapter 4. In brief, following electro-polymerization at optimal conditions (5V for 45 mins), the pTh-Pdots are exfoliated from the polythiophene film in tetrahydrofuran (THF) under ultrasonication for 1h. Subsequently following purification, they are extracted under rotary evaporation and re-suspended in water and filtered using a 0.1 μm nitrocellulose membrane to remove aggregates.

5.1.2 Bacteria Inhibition Studies

All bacterial strains were from the American Type Culture Collection. Optical density (OD) at 600 nm (OD 600) of the bacterial suspensions was measured using a spectrophotometer (SpectraMax M5; Molecular Devices). pTh-Pdots (Sigma Aldrich) were added to 2 ml bacterial suspensions in Luria Broth (LB) solution (0.01 OD 600 corresponding to 1×10^6 cells/mL), to attain the final concentrations between 0 – 100 $\mu\text{g/ml}$. This was followed by incubation at 37 °C for 18 h, with ~200 rpm constant shaking. OD change after the incubation was used to assess the inhibitory effect of pTh-Pdots or antibiotics on bacterial growth. Some experiments were performed using ampicillin-resistant E.coli bacteria, which were transformed with a plasmid containing

the ampicillin-resistance gene (Origene) using heat shock. All experiments were independently repeated 3 times.

5.1.3 Peroxidase Activity Studies

All bacterial strains were from the American Type Culture Collection. Optical density of the bacterial suspensions was measured using a spectrophotometer (SpectraMax M5; Molecular Devices) at 600 nm (OD 600). pTh-Pdots or/and H₂O₂ (Sigma Aldrich) were added to 2 ml bacterial suspensions in Luria Broth (LB) solution (0.01 OD 600 corresponding to 1×10^6 cells/mL), to attain the final concentration of 0 – 100 µg/ml and 0 – 0.75 mM, respectively. This was followed by incubation at 37 °C for 8 h, with ~200 rpm constant shaking. OD change after the incubation was used to assess the inhibitory effect of pTh-Pdots – H₂O₂ mixture on bacterial growth.

5.1.4 Viability Studies

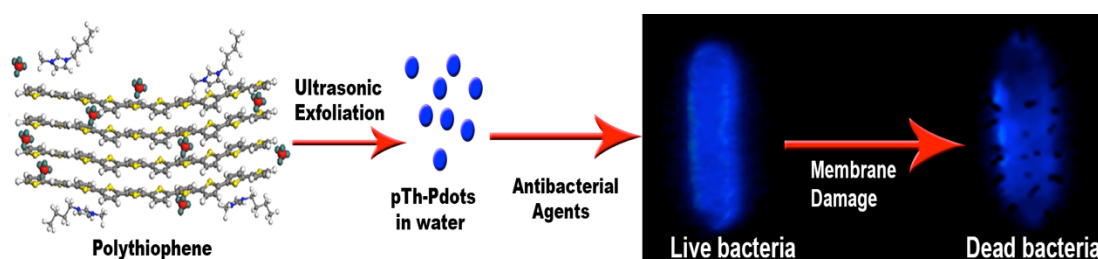
Bactericidal activity of pTh-Pdots was examined by a fluorescence viability kit (Live/Dead BacLight bacterial viability kit, Life Technologies) and FESEM. Before these imaging experiments, overnight grown *E. coli* cultures (OD 600 = 1.0, corresponding to 1×10^9 cells/mL) were centrifuged at 6000 rpm, followed by suspension in HBSS (Hank's balanced salt solution, Life Technologies) and incubated for 2 h with or without 100 µg/ml pTh-Pdots. Subsequently, the suspensions were centrifuged at 6000 rpm, washed thrice with PBS, and re-suspended in PBS. Imaging experiments were performed to study the bactericidal effect of pTh-Pdots on fully-grown *E. coli* cultures. Confocal images were taken using a LSM710 confocal laser-scanning microscope (Carl Zeiss, Germany) using excitation at 488 nm (green) and 580 nm (red).

5.1.5 FESEM Imaging

For FESEM, the sample preparation followed previously reported protocols.¹⁹² Briefly, the bacteria were fixed using 2.5% glutaraldehyde (primary fixative) in 0.1 M phosphate buffer (PB) for 1h. Subsequently, the cells were washed 3 times with PB, followed by incubation in 1% osmium tetroxide (secondary fixative) for 1h. After washing 3 times with PB, the cells were then dehydrated in ethanol at increasing concentrations (25, 50, 75, 90, and 100%). Finally, the cells were re-suspended in the mixture of hexamethyldisilazane and ethanol (1:1) for 15 min, followed by centrifugation at 2000 ×g. The pellet was collected and allowed to dry overnight at room temperature.

5.2 Results & Discussion

5.2.1 Anti-Bacterial Activity



Scheme 5-1: Schematic for pTh-Pdots as fluorophores and antibacterial agents.

With some thiophene derivatives demonstrating good bactericidal properties,¹⁹⁰⁻¹⁹¹ we speculate on the antibacterial behaviour of pTh-Pdots. Indeed, it was found that pTh-Pdots were highly effective against both Gram-negative [G(-); *E. coli* and *P. aeruginosa*] and Gram-positive [G(+); *S. aureus*] bacteria, with low minimum inhibitory concentrations (MIC, lowest concentration to cause appreciable inhibition on bacterial growth). The potency of pTh-Pdots towards the bacterial strains was comparable to a commonly used broad-spectrum antibiotic (kanamycin).

Dose dependent studies clearly indicated the pTh-Pdots as most effective against *E. coli* with MIC ~45 µg/ml, followed by *S. aureus* (MIC ~60 µg/ml) and *P. aeruginosa* (MIC ~100 µg/ml) (Figure 5-1a & 5-1b). Despite high concentrations (~150 µg/ml) they were unable to demonstrate any significant stress on the G(+) *B. subtilis* strains. Unsurprisingly, pTh-Pdots are more potent towards G(-) bacteria than G(+) bacteria, which are protected against antibacterial agents by a thick peptidoglycan surface layer.

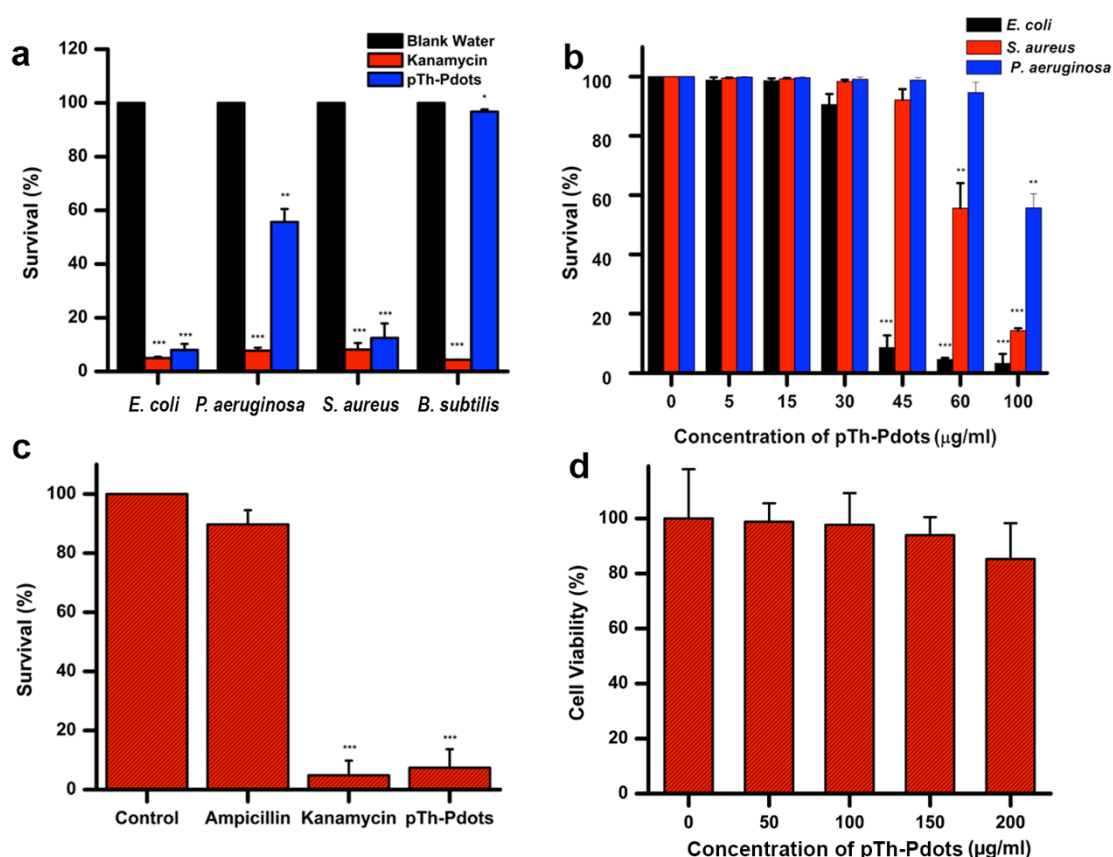


Figure 5-1: Antibacterial activity of pTh-Pdots. (a) Viability test against G(+) and G(-) bacteria with 100 µg/ml pTh-Pdots. (b) Dose dependent effect of pTh-Pdots against G(+) and G(-) bacteria. (c) Viability test of Ampicillin-resistant *E. coli* treated with ampicillin, kanamycin and pTh-Pdots (all at 100 µg/ml). (d) MTT Assay of rat fibroblasts after overnight incubation with pTh-Pdots at various concentrations.

The anti-microbial properties of pTh-Pdots against clinically significant G(-) bacteria offer a promising new antibacterial agent effective as disinfectants. Furthermore,

pathogenic *E. coli* strains can be life threatening (e.g., GI and urinary tract infection, septicemia, etc.), and resistant to antibiotics (MDR in *E.coli* strains against β -lactam antibiotics is rapidly rising).¹⁹³ Additionally, these drug-resistant *E.coli* bacteria are readily acquired *via* the diet (food and water).¹⁹⁴ Thus, the effectiveness of pTh-Pdots against ampicillin (a β -lactam antibiotic) resistant *E.coli* strains was further investigated and compared against two broad-spectrum antibiotics (ampicillin & kanamycin). As shown in Figure 5-1c, pTh-Pdots can efficiently kill ampicillin-resistant *E. Coli*. On the other hand, they demonstrated high efficacy for use in clinical settings, as pTh-Pdots exhibited high biocompatibility towards mammalian cells (primary rat fibroblast cells in Figure 5-1d and HeLa cells in Figure 4-8). Furthermore, the antibacterial capability of pTh-Pdots was confirmed to be independent of the effect of the BMIM⁺ moieties attached on its surface. As seen in Figure 5-2, the ionic liquid (BMIMBF₄) was incapable of causing bacterial death despite usage at high concentrations (0.5 mg/ml).

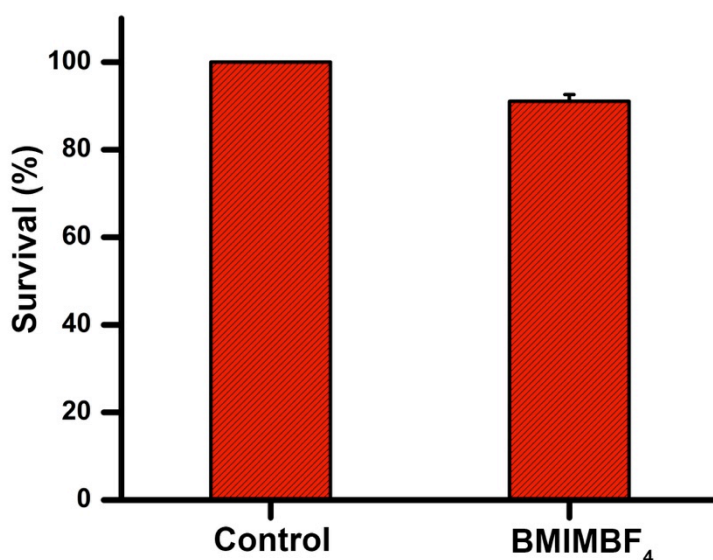


Figure 5-2: The influence of BMIMBF₄ (0.5 mg/mL) to *E. coli* growth. The average and standard deviation are obtained from 3 independent experiments.

5.2.2 pTh-Pdots as Peroxidase Mimics

Hydrogen peroxide (H_2O_2), is a widely used medical reagent for wound disinfection. Nonetheless it possesses significant disadvantages such as reduced activity compared to hydroxyl radicals, and high concentrations for effective action (166 mM to 1M).¹⁸⁹ This in turn can be harmful to the healthy tissues.

Interestingly, we discover that pTh-Pdot (10 $\mu\text{g/ml}$) is an excellent mimic to peroxidase, which converts H_2O_2 into hydroxyl radicals ($\bullet\text{OH}$) (Figure 5-3a). Graphene quantum dots (GQDs) have also been found to exhibit peroxidase-mimicking activities.¹⁹⁵⁻¹⁹⁶ Taking advantage of this, they have been used to improve the antibacterial performance of H_2O_2 for wound disinfection.¹⁸⁹ We found that pTh-Pdots possess much higher peroxidase activity than GQDs (Figure 5-3b). The peroxidase-mimicking activity was attributable to the high electron transport property of the semiconducting polymer dots.¹⁹⁷

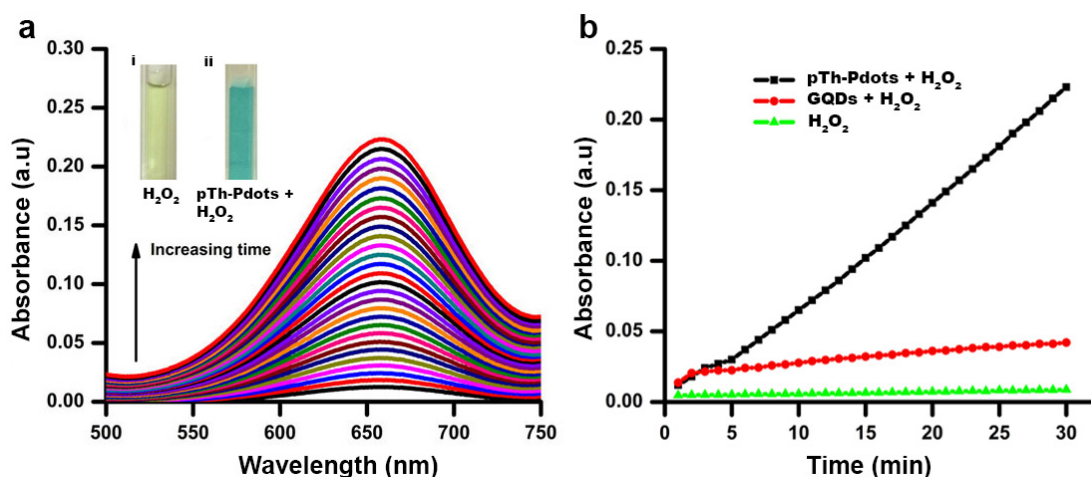


Figure 5-3: (a) Absorption spectra of the mixture of 10 $\mu\text{g/ml}$ pTh-Pdots, 0.25 mM H_2O_2 and 0.6 mM 3,3',5,5'-Tetramethylbenzidine (TMB) with various reaction durations (0 – 30 min). TMB is a commonly used reporter for peroxidase activity (upon oxidation by hydroxyl radicals, it turns blue and increases absorbance at 650 nm). The photographs in the inset shows that TMB turns into blue in the presence of both H_2O_2 and TMB (30-min reaction). (b)

Absorbance (at 650 nm) of 0.6 mM TMB (as the indicator of peroxidase activity) at various reaction durations, in the presence of 0.25 mM H₂O₂, or 10 µg/ml GQD + 0.25 mM H₂O₂, or 10 µg/ml GQD + 0.25 mM H₂O₂.

Although pTh-Pdots by themselves cannot kill gram-positive *B. subtilis* (Figure 5-1a), the synergistic effect between pTh-Pdots and H₂O₂ is potent (Figure 5-4b). pTh-Pdots can greatly enhance the potency of H₂O₂ in killing both gram-negative (Figure 5-4a) and gram-positive strains (Figure 5-4b). By utilizing the intrinsic anti-microbial behaviour of the blue-Pdots in tandem with its peroxidase-like behaviour, we were able to significantly decrease the bacterial viabilities. The overall minimum inhibitory concentration of blue-Pdots required for both the G(+) and G(-) strains is extremely low at 10 µg/ml when used in tandem with extremely low concentrations of H₂O₂.

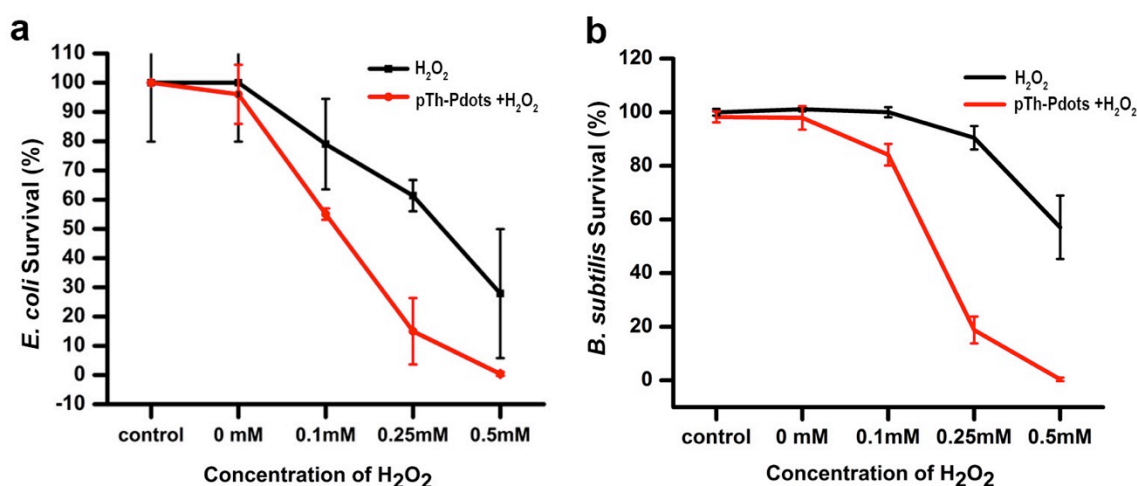


Figure 5-4: Viability Tests of *E. coli* (a) and *B. subtilis* (a) treated with H₂O₂ at different concentrations with or without pTh-Pdots (10 µg/mL).

5.2.3 Antibacterial Mechanism of pTh-Pdots

Previous studies have proposed the antimicrobial mechanism of organic nanomaterials to be predominantly dependant on aggregations and physical interactions, leading to bacterial membranes & cytoplasmic collapse.^{185, 198} We speculate that the antimicrobial

activity of the positively charged pTh-Pdots themselves (zeta potential $\zeta = 21.2$ mV) may be realized by disrupting the negatively charged bacterial membrane through electrostatic interaction. Indeed as shown in Figure 5-5a, in the presence of a viability testing dye mixture (SYTO 9 / propidium iodide), live bacteria appear green due to SYTO 9 staining. However, dying or dead bacteria following pTh-Pdots treatment appear yellow or red due to uptake of red propidium iodide through compromised cell membranes.

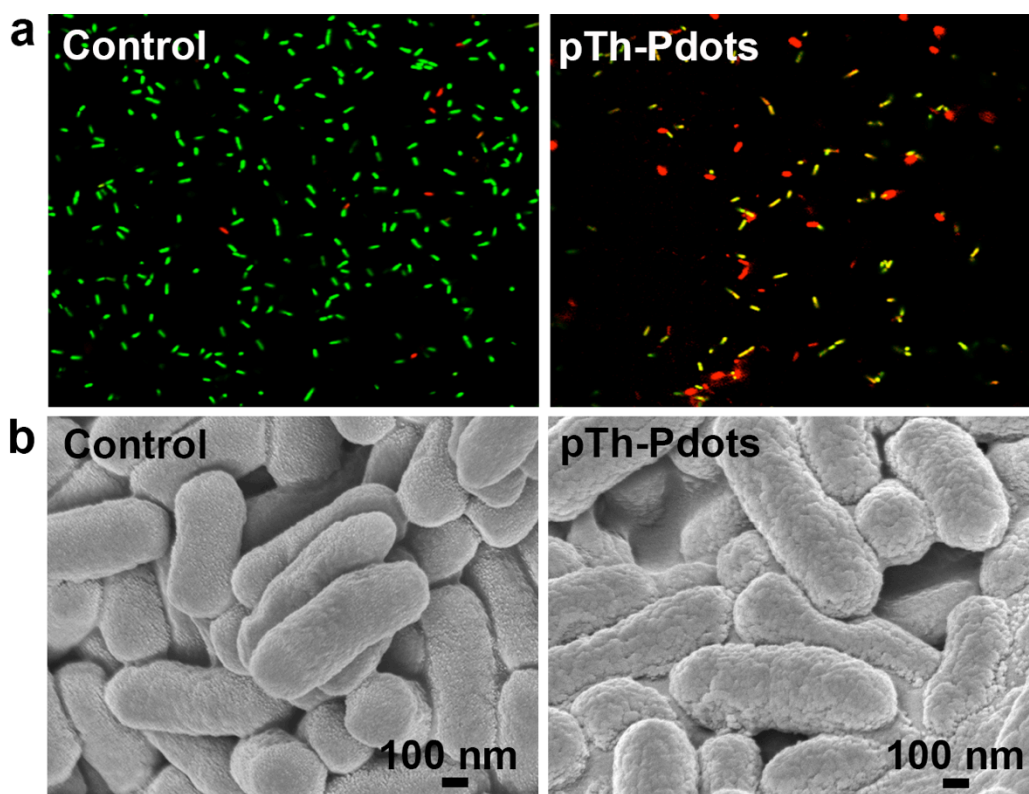


Figure 5-5: Fluorescence images with Live/Dead dye staining (a) and FESEM images of *E. coli* cells (b) without (left column) or with (right column) incubation of pTh-Pdots (100 μ g) for 2 h.

Consistently, field-effect scanning electron microscopy (FESEM) also shows disintegrating/disrupted bacterial membranes following treatment with the polymer dots (Figure 5-5b). Indeed, the blue-Pdots appear to aggregate on & penetrate through

the negatively charged bacterial membrane via electrostatic interactions wherein they disrupt the cell membrane and cause bacterial cell death.

5.3 Conclusion

To the best of our knowledge for the first time, we herein demonstrate polymer dots as the synthetic alternatives to traditional antibacterial agents (e.g. antibiotics). We have demonstrated previously synthesized pTh-Pdots (Chapter 4) as effective antibacterial agents. These pTh-Pdots serve as excellent antibacterial agents against both gram-negative and some gram-positive bacteria, even drug-resistant strains. Furthermore, the synergistic use of their ability to disrupt bacterial membranes and mimic peroxidase activity further increases their potency against the gram-positive bacteria *B. subtilis*. These small sized, peroxidase-mimicking, biocompatible polymer dots promise versatile applications, ranging from therapeutics application in anti bacterial creams to wound disinfectants.

This chapter (including phrases and figures) is adapted / reproduced with permission from our accepted journal article “Thiophene-derived polymer dots for imaging endocytic compartments in live cells and broad-spectrum bacterial killing. Materials Chemistry Frontiers, 2016, 152-157. Copyright 2016, The Royal Society of Chemistry.”

Chapter 6

6. Three-Dimensional Graphene - Carbon Nanotube Hybrid Bioelectrodes for High Performance Enzymatic Biofuel Cells

As reviewed in Chapter 2 Enzymatic biofuel cells (EBFCs) are green energy devices, capable of harvesting electricity from renewable and abundantly available biofuels using enzymes as biocatalysts for the oxidation of biofuels (most commonly, glucose) and reduction of oxidizers (most commonly, oxygen).¹⁹⁹⁻²⁰¹ As glucose is a ubiquitous fuel in living systems, EBFCs are promising as biocompatible and everlasting power sources for implantable devices.²⁰²⁻²⁰³ However, the existing EBFCs suffer several performance related issues not limited to inefficient electron transfer between the enzymes and electrodes, limited active surface area, low conductivity of the electrode, and hindered mass transport.

As discussed earlier, the rate-limiting step for EBFC performance is the poor electron transfer to the electrode, a result of the active centers of the redox enzymes being usually buried deep within the protein matrices. Various nanomaterials such as semiconducting polymer nanowires,¹¹³ inorganic nanoparticles,²⁰ metal oxides metal-organic frame-works (MOFs),²⁰⁴ and biomaterials¹¹⁴ have been used till date to overcome this drawback with limited success. Compared to these materials, carbon nanotubes (1D π -conjugated carbon nanowires) possess superior physical, electrical and electrochemical properties. Their high electrical conductivity, electrochemical stability, and molecular dimension promote intimate interaction with the enzymes.²⁰⁵ Single-walled carbon nanotubes (SWCNTs) have therefore been utilized as the conducting nanowires to facilitate electron transfer from the catalytic centers of enzymes to electrode.

Furthermore we have previously discussed regarding Graphene, a two-dimensional (2D) π -conjugated cousin of 1D SWCNT that has recently attracted enormous interest as an electrode material due to its exceptionally high conductivity and specific surface area. More recently, it has been demonstrated that due to its distinct advantages the three-dimensional (3D) architectures of this 2D material can serve as novel 3D electrochemical electrodes for various applications²⁰⁶ (e.g., energy storage,²⁰⁷ energy conversion,²⁰⁸ and biological sensing.²⁰⁹)

In this chapter, 1D single-walled CNTs (SWCNTs) decorated 3D graphene were utilized to fabricate both the bioanode and biocathode in an EBFC (Scheme 6-1). We demonstrate that EBFCs equipped with such enzyme-functionalized 3D graphene-SWCNT hybrid electrodes exhibit significant improvement in performance as compared to previously reported bio-power devices.

6.1 Materials & Methods

6.1.1 Materials

The nickel (Ni) foams were purchased from Alantum Advanced Technology Materials (China) while P3-SWCNTs were purchased from Carbon Solutions. Glucose oxidase (GOD, Type VII from *Aspergillus niger*) solution was prepared by dissolving the powdered enzyme (5 mg mL⁻¹) in a Tris-HCl buffer (pH 8.9, 0.05 M). Laccase (from *Trametes versicolor*) solution was prepared by dissolving the powder in a PBS buffer (pH 7.0, 0.05 M). The electrolyte buffer solution (pH 5.0, 0.2 M) was prepared using sodium acetate and acetic acid.

6.1.2 Characterization and Measurements

The samples were examined by Field emission scanning electron microscopy (FESEM, JMS-6700F), Raman spectroscopy (WITec CRM200 using 633 nm laser), and Fourier transform infrared spectroscopy (Perkin Elmer FTIR Spectrum GX 69233). Cyclic voltammetry (CV) measurements were conducted using an electrochemical workstation (CHI 660D), in a standard three-electrode configuration consisting of a platinum counter electrode, a saturated calomel reference electrode (SCE) and a fabricated 3D graphene composite working electrode. Open circuit potential was measured in a two-electrode configuration between the SCE and the working electrode.

6.1.3 Preparation of 3D Graphene Composite Electrodes

3D graphene was grown using a previously reported chemical vapor deposition (CVD) method, on a nickel foam substrate with ethanol as the carbon source.²¹⁰ Subsequently, the nickel foam was etched away overnight in 3 M HCl at 60 °C to obtain free-standing 3D graphene foam. The electrode was subsequently fabricated by mounting 3D graphene (0.5 cm²) onto a glass slide. A copper wire, fixed and insulated on one end of graphene substrate was then used as the electrical lead (Figure 6-1). Subsequently, the electrode was soaked in P3- SWCNT dispersion (1 mg mL⁻¹ in *N,N*-dimethylformide) for overnight. After drying at 50 °C for 3 h, the electrode was dipped into 4 mg mL⁻¹ 1-ethyl-3-(3-dimethyl-aminopropyl) carbodiimide hydrochloride (EDC) and *N*-hydroxysuccinimide (NHS) solution for 1 h, followed by conjugation with the respective enzymes by dipping into the enzyme solutions (GOD or laccase) for 24 h.

6.1.4 Biofuel Cell Design

The EBFC was fabricated in-house using acrylic glass. The anodic and cathodic chamber separating perfluorosulfonic acid/PTFE copolymer membrane (25.4 μm thick,

Nafion[®]) was purchased from DuPont (Figure 6-1). While the anodic chamber contained nitrogen saturated glucose (defined amount) containing electrolyte solution, the cathodic chamber was saturated with oxygen and contained 0.5 mM 2,2'-azinobis (3-ethylbenzothiazoline-6-sulfonic acid) diammonium salt (ABTS) mediator.

6.1.5 Biodesign Test

The E_{cell}^{ocv} of the EBFC was measured using CHI-660D electrochemical station. At steady state E_{cell}^{ocv} , the EBFC was loaded with external resistances varying from 100 Ω ~ 100 k Ω to determine the polarization and power output density. A bread-board containing LEDs was used to test the real-time power output from the EBFC.

6.2 Results and Discussion

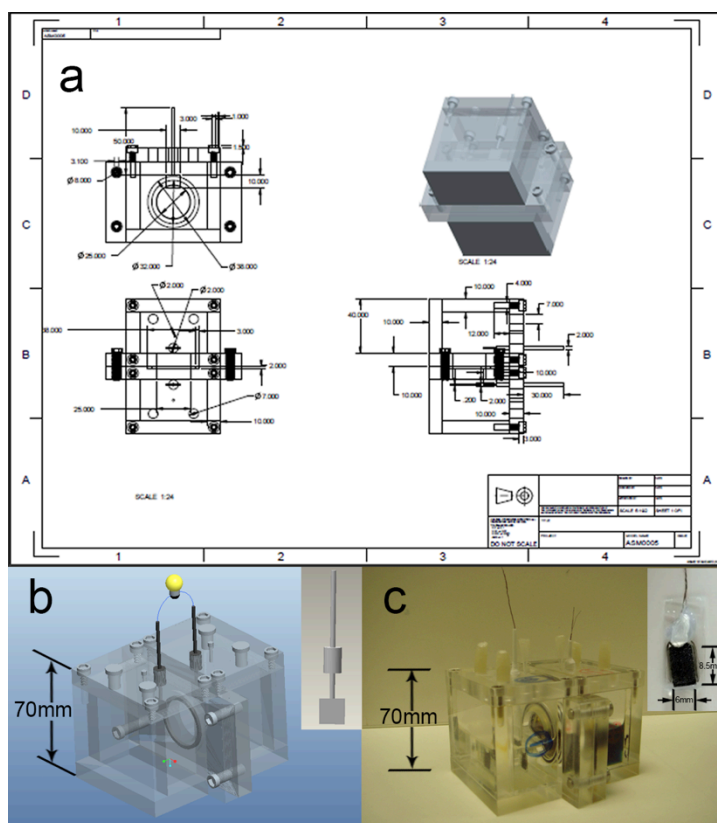
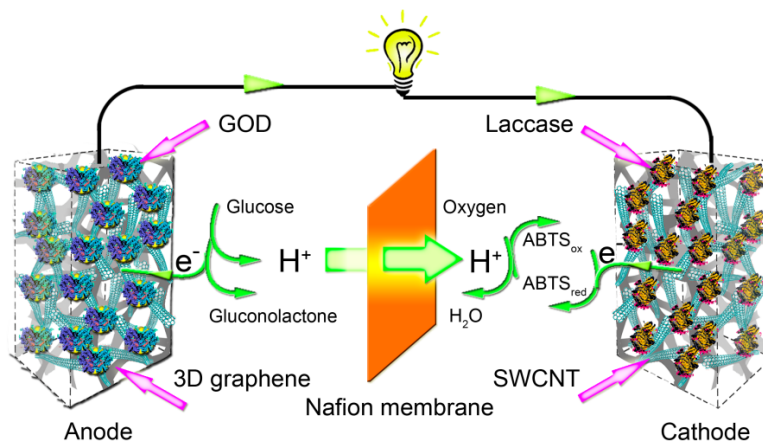


Figure 6-1: (a) The engineering drawing of the biofuel cell. (b) A 3D view of the biofuel cell. Inset shows the schematic drawing of the electrode. (c) The optical image of the working biofuel cell. Inset shows the optical image of the electrode.



Scheme 6-1: Illustration of the EBFC equipped with 3D graphene-SWCNT hybrid electrodes (not to scale).

6.2.1 Material Characterization

The synthesized 3D graphene is a monolithic macroporous structure, as revealed by scanning electron microscopy (Figure 6-2a). SWCNTs can be adsorbed onto 3D graphene scaffold through π - π and hydrophobic interactions,²¹¹⁻²¹³ by direct incubation of the graphene electrode with SWCNT dispersion in DMF. As shown Figure 6-2b, 3D graphene is completely covered by a thin yet dense network of SWCNTs, with the net mesh size being comparable to a macromolecule. The bare 3D graphene is mainly few-layered (as indicated by the ratio between 2D and G band in Figure 6-2c) and highly pristine (defect-free, as indicated by the absence of D band).¹¹⁷ The 3D graphene-SWCNT hybrid exhibits characteristic a D band from the SWCNTs. The presence of carboxyl groups on the SWCNTs is confirmed by Fourier transform infrared spectroscopy (FTIR) (Figure 6-2d). The amphiphilic carboxylated SWCNTs besides interacting with the 3D graphene, make the hybrid structure hydrophilic as evidenced

by the contact angle measurements (Figure 6-2e and 6-2f). This increased hydrophilicity is critical for electrolyte penetration. Furthermore, the SWCNTs coating further increases the overall active surface area of the electrode. Finally, the hybrid electrode is covalently functionalized with glucose oxidase (GOD) or laccase enzymes *via* covalent bonding between the carboxyl group on SWCNTs and amino group on the protein for the anode and cathode, respectively.

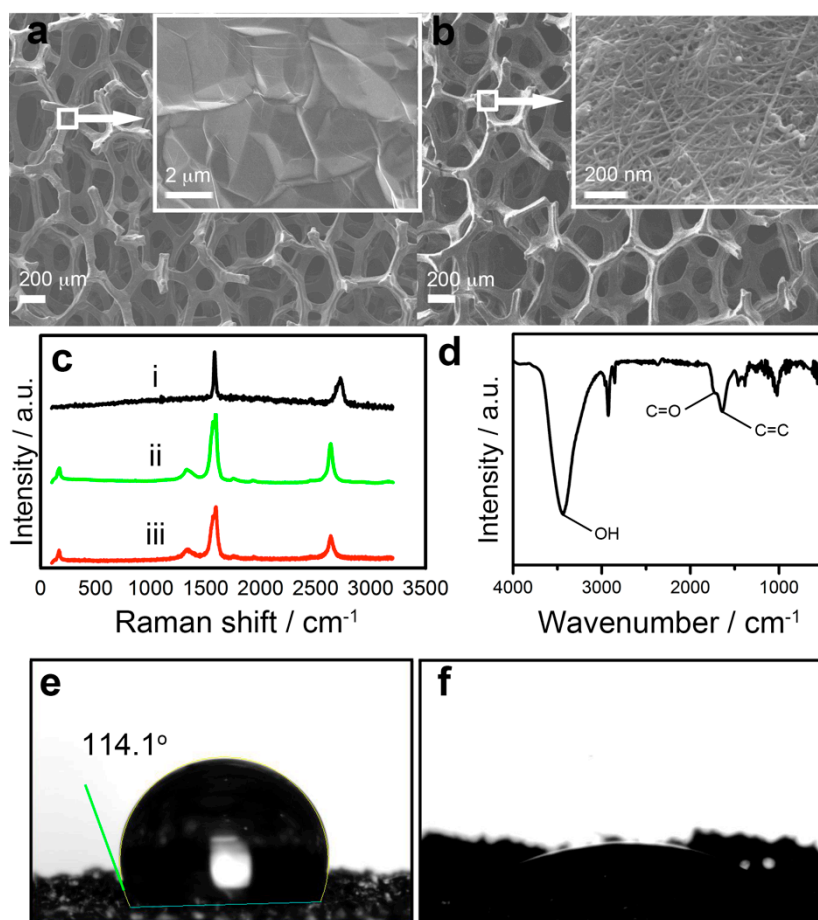


Figure 6-2: FESEM images of (a) bare 3D graphene and (b) 3D graphene-SWCNT hybrid. Each inset shows the surface of the skeleton at a large magnification. (c) Raman spectra of (i) 3D graphene, (ii) SWCNT and (iii) 3D graphene-SWCNT hybrid. (d) FTIR of SWCNT. Contact angle measurements of (e) 3D graphene and (f) 3D graphene-SWCNT hybrid.

6.2.2 Anodic Properties

As demonstrated in Figure 6-3a, the anodic open circuit potential (E_a^{ocp}) of the 3D graphene-SWCNT-GOD hybrid electrode in the presence of 30 mM glucose is ~ -0.58 V (± 0.01 , $n = 3$ electrodes). The value observed is approximately near the theoretical limit determined by the thermodynamic equilibrium of a gluconolactone/glucose couple,^{131, 214} and is significantly higher than previously reported values.¹⁰⁴ In contrast, the E_a^{ocp} of the enzyme loaded but bare 3D graphene is only ~ -0.12 V (± 0.005 , $n = 3$), suggesting the critical role of SWCNTs. Cyclic voltammetry (CV) traces of GOD functionalized hybrid electrode show a pair of prominent redox peaks (at -0.337 V and -0.363 V respectively) in perfect accordance with the reduction and oxidation potentials of the redox active centers (flavin adenine dinucleotide, FAD) of the enzyme (Figure 6-3b).²¹⁵

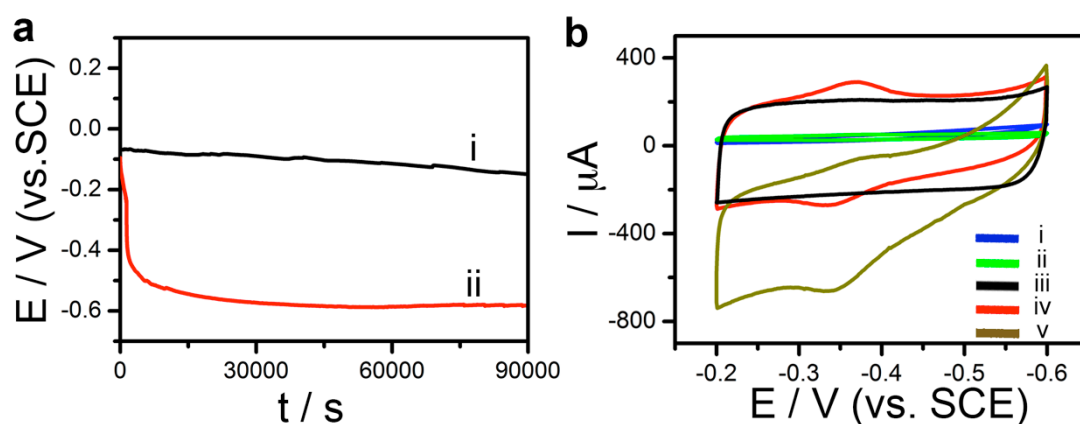
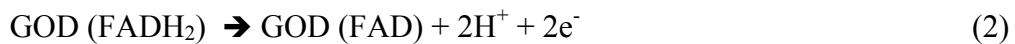
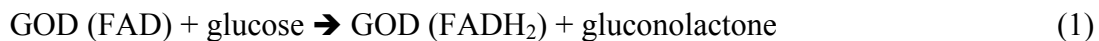


Figure 6-3: (a) The open circuit potential of (i) the 3D graphene-GOD anode and (ii) 3D graphene-SWCNT-GOD anode in pH 5.0 electrolyte solution containing 30 mM glucose. (b) The CVs of (i) 3D graphene electrode, (ii) 3D graphene-GOD electrode, (iii) 3D graphene-SWCNT hybrid electrode and (iv) 3D graphene-SWCNT-GOD hybrid electrode in pH 5.0 electrolyte solution. (v) 3D graphene-SWCNT-GOD hybrid electrode in pH 5.0 electrolyte solution containing 1 mM glucose.

This observation unambiguously indicates the successful immobilization of GODs on the electrode surface as well as an excellent enzyme-electrode electrical coupling (direct electron transfer - DET).²¹⁶⁻²¹⁷ To further support this, it is observed that addition of glucose leads to obvious increase of the oxidative current and dramatic decrease of the reductive current in the CV traces. In the absence of oxygen, the observed CV is a result of electrochemical reactions in the active center of GOD, which are as follows²¹⁸⁻²¹⁹:



In addition, the onset oxidation potential in the presence of glucose is about -0.550 V, which is consistent with the E_a^{ocp} of the of the 3D graphene-SWCNT-GOD anode in the glucose solution.²²⁰⁻²²² The uniform coating of a non-conductive layer of proteins is confirmed by FESEM image, in which the SWCNT mesh becomes blurry due to snugly trapping of proteins (Figure 6-4). As expected, these redox peaks are absent in the GOD-free hybrid electrode. In comparison, we demonstrated that both the 3D graphene and 3D graphene-SWCNT hybrid exhibit no catalytic activities towards glucose (Figure 6-5a). The bare 3D graphene electrode coated with GODs *via* physioadsorption demonstrates weak redox peaks from GODs as well as a weak response towards glucose (Figure 6-5b), presumably due to low abundance of GODs, possible denaturation of GOD on the flat graphene surface, and poor interactions between the enzymes and the electrode. In support of this, FESEM reveals that GODs only sparsely adhere onto the smooth graphene surface as clusters preferably on the wrinkles (Figure 6-4).

In order to evaluate the electron transfer, the CVs of the 3D graphene-SWCNT-GOD electrode were investigated at different scan rates. As shown in Figure 6-6, the formal

potential ($E^{0'}$ – the average between the reduction and oxidation potentials) of GOD remains unchanged with increasing scan rates, with both the anodic and cathodic peak currents (their ratio is close to 1) showing a proportional increase with scan rates. These observations suggest that the redox of GOD is a reversible and surface-confined process. According to the following equation, $i_p = nFQv/4RT$ (where i_p = redox peak current; Q = integrated charge of the redox peak; v = scan rate; F = Faraday constant; R = gas constant; T = temperature),²²³ the number of charges transferred from the GOD redox reaction (n) is calculated to be 2, which is close to the theoretical value of FAD to FADH₂ conversion in the active center of GOD. This confirms an excellent electrical coupling between GOD and the hybrid electrode.

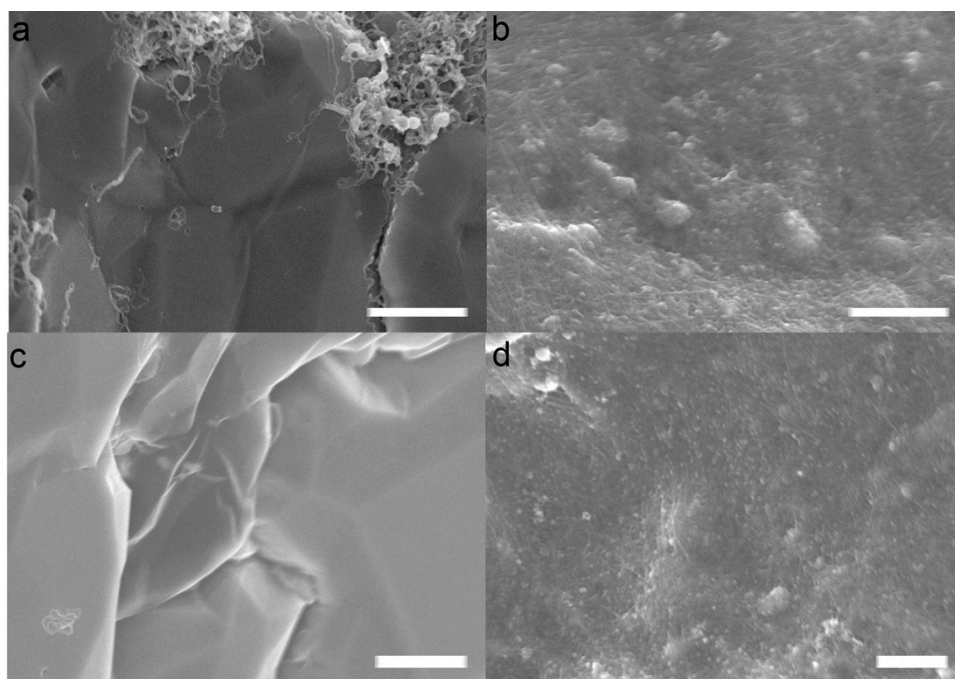


Figure 6-4: FESEM images of (a) 3D graphene-GOD electrode, (b) 3D graphene-SWCNT-GOD electrode, (c) 3D graphene-laccase electrode, and (d) 3D graphene-SWCNT-laccase electrode. Scale bar = 1 μ m.

Furthermore, the small peak-peak separation (the different between the oxidative and reductive peaks, ~ 29 mV), also nicely agrees with the theoretical value

($\ln 10 \cdot R \cdot T / F \cdot n$), indicating the electron transfer kinetics is fast enough to maintain the Nernst equilibrium of GOD's redox transition. Based on Laviron's theory,²²⁴ $k_s = mnFv/RT$ (where m is a constant determined by the separation between oxidative and reductive peaks),²²⁵ the electron transfer rate constant k_s is calculated to be $12.52 \pm 0.84 \text{ s}^{-1}$. This is significantly higher than the previously reported values obtained from graphene (2.83 s^{-1}),²²⁶ multi-walled carbon nanotubes (1.53 s^{-1}),²²⁷ boron-doped carbon nanotubes (1.56 s^{-1}),²²⁸ or single-walled carbon nanohorns (3.0 s^{-1})²²⁹ based electrodes.

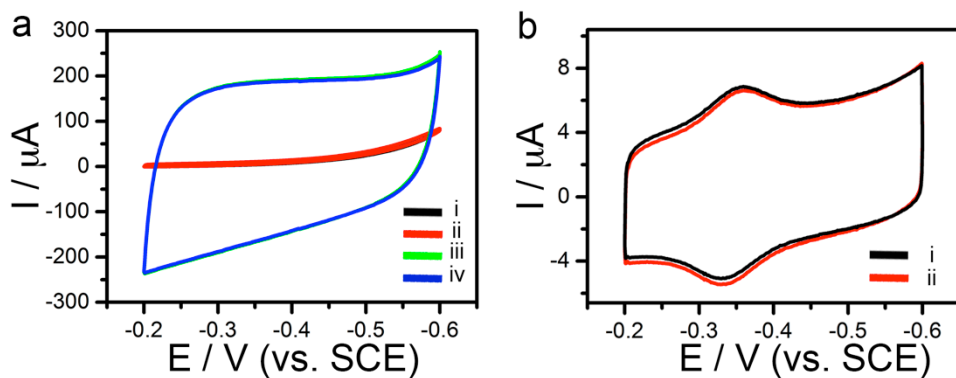


Figure 6-5: (a) The CVs of the 3D graphene electrode in pH 5.0 electrolyte solution, (i) without glucose and (ii) containing 1 mM glucose; 3D graphene-SWCNT electrode in pH 5.0 electrolyte solution, (iii) without glucose and (iv) containing 1 mM glucose. (b) The CVs of 3D graphene-GOD electrode in pH 5.0 electrolyte solution, (i) without glucose and (ii) containing 1 mM glucose.

In an ideal situation (reversible and unhindered electrical coupling between a monolayer of electroactive enzyme and the underlying electrode), the CV traces are predicted to exhibit symmetric redox peaks without any gap between the oxidation and reduction potentials and a peak-width at half height of $90.6 \text{ mV}/n$ (here, $n = 2$).²³⁰ These are indeed observed at a slow scan rate of 1 mV s^{-1} (Figure 6-7), indicating that the electron transfer between GOD and electrode is ideally reversible in such conditions. Furthermore, we demonstrate that $E^{0'}$ decreases linearly with an increase in pH with a slope nearly equal to the theoretical value of $58.6 \text{ mV}/\text{pH}$ (Figure 6-8). This

suggest a reversible electrochemical process with an equal-number ($n = 2$) of electrons and protons involved in the GOD redox reaction:

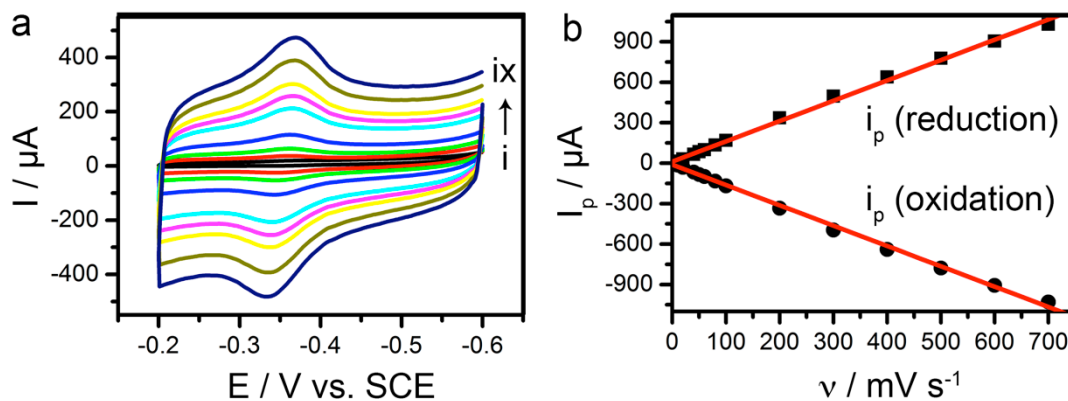
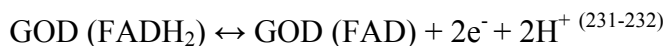


Figure 6-6: (a) CVs of the 3D graphene-SWCNT-GOD hybrid electrode at different scan rates: (i) 1 mV s^{-1} , (ii) 5 mV s^{-1} , (iii) 10 mV s^{-1} , (iv) 20 mV s^{-1} , (v) 40 mV s^{-1} , (vi) 50 mV s^{-1} , (vii) 60 mV s^{-1} , (viii) 80 mV s^{-1} , and (ix) 100 mV s^{-1} . (b) Redox peak currents *versus* scan rates from 1 mV s^{-1} to 700 mV s^{-1} .

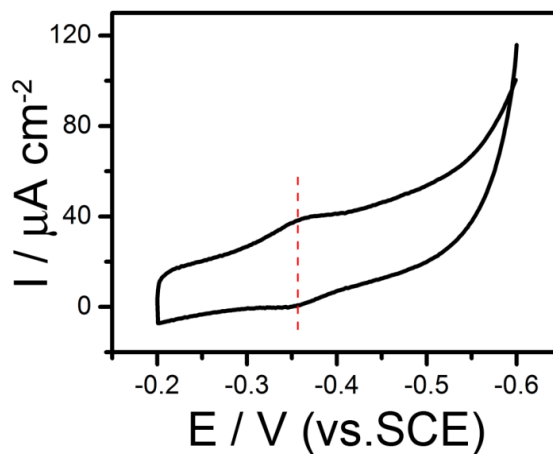


Figure 6-7: CV of the 3D graphene-SWCNT-GOD electrode at the scan rate of 1 mV s^{-1} .

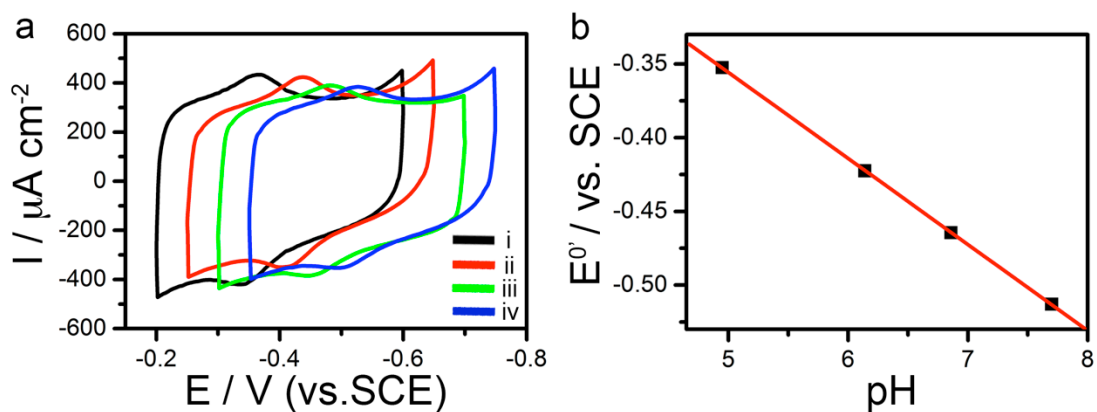


Figure 6-8: (a) CVs of the 3D graphene-SWCNT-GOD electrode in electrolyte solution with different pH values of (i) 4.95, (ii) 6.14, (iii) 6.86, and (iv) 7.70 at the scan rate of 50 mV s^{-1} . (b) Formal potential (E^0) *versus* pH.

6.2.3 Cathodic Properties.

As demonstrated in Figure 6-9a, the cathodic open circuit potential (E_c^{ocp}) of the laccase coated 3D graphene electrode (with saturated oxygen, at pH 5.0) is close to 0 V ($0.02 \pm 0.0003 \text{ V}$, $n = 3$), essentially due to poor adhesion of laccase proteins on graphene surface (Figure 6-4). In comparison, E_c^{ocp} reaches $\sim 0.11 \text{ V}$ (± 0.002 , $n = 3$) when using 3D graphene-SWCNT-laccase electrode. Despite the SWCNTs assisting in abundant loading and snugly anchoring the enzymes, the obtained E_c^{ocp} is still far from the theoretical limit (0.61 V)^{131, 214} suggesting that the electron transfer from the active laccase centers to the electrode is still hindered. ABTS is an electron transfer mediator often used to facilitate the electron transfer from laccase. As shown (Figure 6-9a), in the presence of ABTS (0.5 mM), E_c^{ocp} of the 3D graphene-SWCNT-laccase electrode is boosted nearly close to the theoretical thermodynamic equilibrium of the O_2/H_2O couple ($0.6 \pm 0.01 \text{ V}$, $n = 3$). These observations suggest that ABTS molecules assist in facilitating the electron transfer from oxygen reduction.

Consistently, it is found that the CVs of the 3D graphene-laccase electrode or bare 3D graphene-SWCNT electrode do not exhibit the redox peaks from laccase redox

transition, whereas a pair of prominent redox peaks (at -0.003 V and 0.086 V, respectively), corresponding to the T2 redox active center of laccase (Figure 6-9b) are observed from the 3D graphene-SWCNT-laccase electrode. This confirms the excellent coupling between the enzymes and the 3D graphene-SWCNT substrate. The redox of laccase on the electrode is a reversible and surface-confined process, as evidenced by the linear scaling between redox currents and scan rate (Figure 6-10). In comparison, the controls electrodes namely bare 3D graphene electrode, 3D graphene-SWCNT hybrid electrode, and laccase functionalized 3D graphene electrode show little to no catalytic action towards O_2 (Figure 6-11).

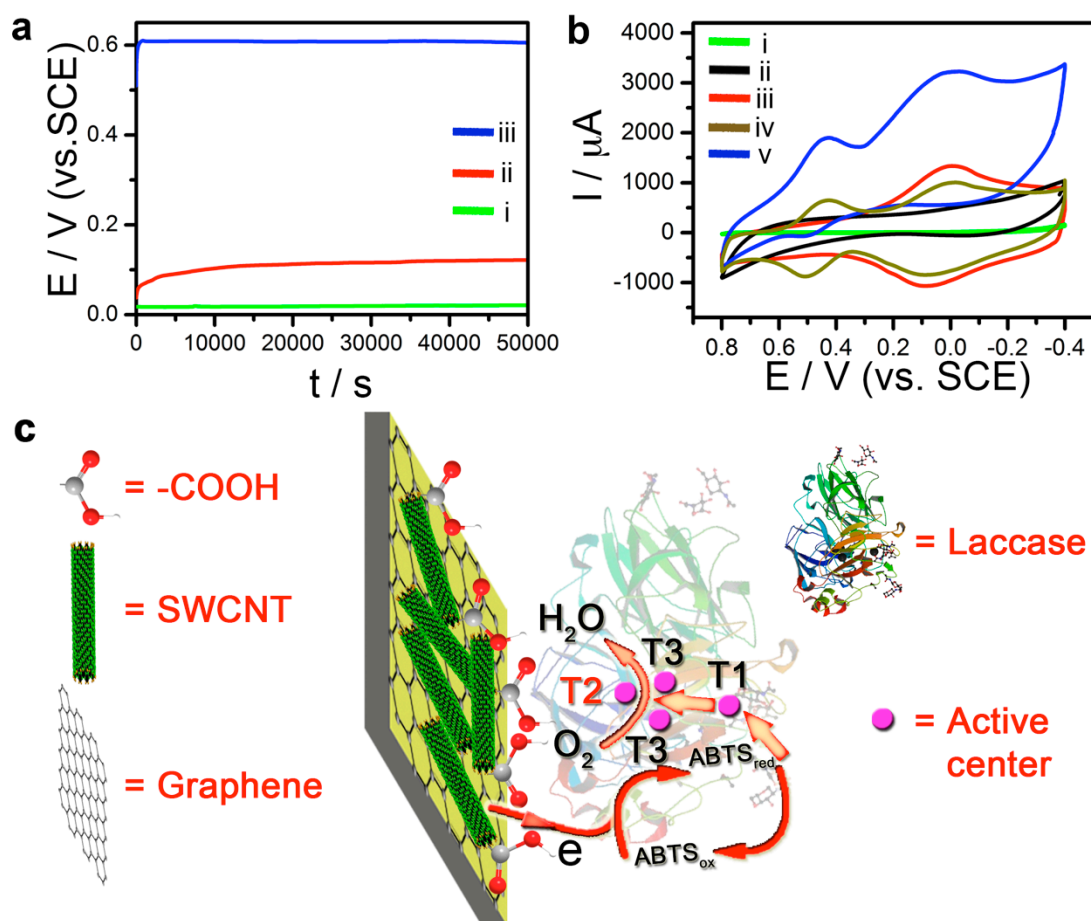


Figure 6-9: (a) The open circuit potential (measured in pH 5.0 electrolyte solution saturated with O_2) of (i) 3D graphene-laccase cathode and (ii) 3D graphene-SWCNT-laccase cathode, and (iii) 3D graphene-SWCNT-laccase cathode (with 0.5 mM ABTS). (b) The CVs of (i) 3D graphene-laccase electrode (solution with saturated N_2), (ii) 3D graphene-SWCNT hybrid

electrode (solution with saturated N_2), (iii) 3D graphene-SWCNT-laccase hybrid electrode (solution with saturated N_2), (iv) 3D graphene-SWCNT-laccase hybrid electrode (solution saturated with N_2 and containing 0.5 mM ABTS) and (v) 3D graphene-SWCNT-laccase hybrid electrode (solution saturated with O_2 and containing 0.5 mM ABTS). (c) Illustration of electron transfer pathways.

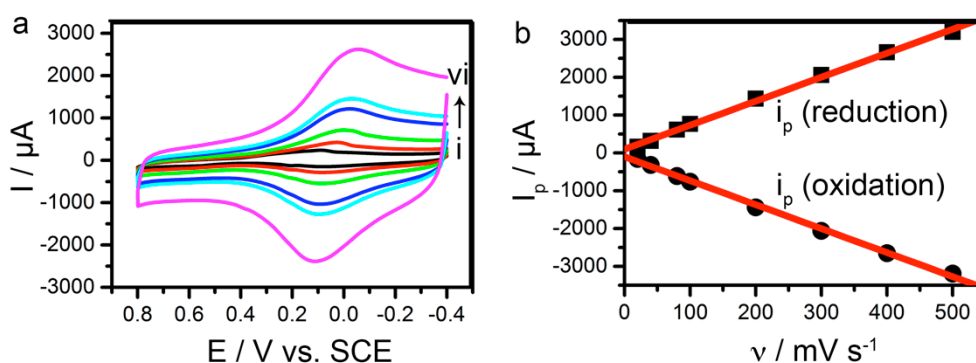


Figure 6-10: (a) CVs of the 3D graphene-SWCNT-laccase hybrid electrode at different scan rates: (i) 10 mV s^{-1} , (ii) 20 mV s^{-1} , (iii) 40 mV s^{-1} , (iv) 80 mV s^{-1} , (v) 100 mV s^{-1} , and (vi) 200 mV s^{-1} . (b) Redox peak currents *versus* scan rates from 20 mV s^{-1} to 500 mV s^{-1} .

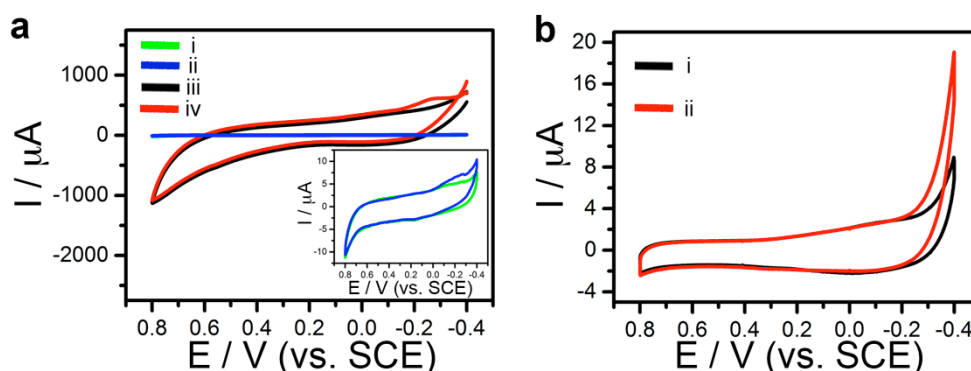


Figure 6-11: (a) The CVs of the 3D graphene electrode in pH 5.0 electrolyte solution, (i) saturated with N_2 and (ii) saturated with O_2 ; 3D graphene-SWCNT electrode in pH 5.0 electrolyte solution, (iii) saturated with N_2 and (iv) saturated with O_2 . (b) The CVs of 3D graphene-laccase electrode in pH 5.0 electrolyte solution, (i) saturated with N_2 and (ii) saturated with O_2 .

As illustrated in Figure 6-9c, laccase has multiple catalytic centers (T1-T3). The redox

peaks in the CV of the 3D graphene-SWCNT-laccase electrode coincide with the redox potentials of T2 center, suggesting that the T2 center of laccase is in the close approximate to the electrode surface to allow direct electron transfer (Figure 6-9b).²³³⁻²³⁴ However, it is known the involvement of T1 center is crucial to achieve efficient oxygen reduction and thus high open circuit potential.²³⁵ In the absence of the ABTS mediator the T1 center, whose oxidation potential is close to the potential of oxygen reduction is unable to participate in the reaction. Therefore, the electron transfer with sole involvement of T2 center is inefficient as a result of the large energy barrier between oxidation of T2 center and oxygen reduction. As the redox potential of ABTS matches well with that of T1 center,²³⁶⁻²³⁷ the diffusive small ABTS molecules can assist in electron transfer to the T1 center of laccase that is distant to the electrode surface,²³⁸⁻²³⁹ whereas the electrons are intra-molecularly passed to the T2/T3 cluster (the oxygen reduction site).²⁴⁰ Therefore, in the presence of ABTS mediator, E_c^{ocp} approaches the thermodynamic equilibrium of O_2/H_2O couple due to improved electrical coupling between the electrode and the catalytic centers of laccase.

As shown in Figure 6-9b, the CV of the 3D graphene-SWCNT-laccase electrode exhibits an additional pair of redox peaks at 0.426 V and 0.508 V due to ABTS.²⁴¹ In the presence of saturated oxygen, the oxidative peak of ABTS decreases while its reductive peak increases confirming the participation of ABTS in the oxygen reaction.²³⁶ The onset reduction potential is near 0.60 V, which coincides with the measured E_c^{ocp} of the 3D graphene-SWCNT-laccase cathode.²²⁰⁻²²² Consistently, in the presence of saturated oxygen, the oxidative peak of T2 center in the CV trace decreases while its reductive peak increases confirming the involvement of T2 center in electron transfer from oxygen reduction (Figure 6-9b).

6.2.4 Enzymatic Biofuel Cell Performance

The enzymatic biofuel cells (EBFCs) were fabricated with a 3D graphene-SWCNT-GOD anode and a 3D graphene-SWCNT-laccase cathode as illustrated in Figure 6-1. As demonstrated in Figure 6-12, the E_{cell}^{ocv} of the EBFC reaches ~ 1.20 V, close to the theoretical potential difference between the O_2/H_2O couple and the gluconolactone/glucose couple at thermodynamic equilibrium.²⁴² To the best of our knowledge, this has not been attained in any of the previous studies. In addition, only a 20% drop of E_{cell}^{ocv} is observed after 30 days, indicating the high stability of our EBFCs. Figure 6-12b displays a typical polarization curve and power output curve of the EBFC in the presence of 30 mM glucose anolyte. The internal resistance of the EBFC is calculated to be 245Ω , by linear-fitting of the polarization curve. The maximal power output (P_{max}) density is $2.27 \pm 0.11 \text{ mW cm}^{-2}$ ($n=3$), which is the highest value ever reported for glucose-based EBFCs. It is superior to the previously reported high performing EBFCs using a graphene electrode¹³⁴ and a carbon nanotube based electrode,¹⁰⁴ as well as other carbon electrodes.²⁴³ Figure 6-12c shows a bell-shaped dependence of P_{max} on glucose concentration at an optimal concentration of ~ 30 mM. Three EBFCs in series are able to lighten up a violet LED with a turn-on voltage of ~ 3 V (Figure 6-12d).

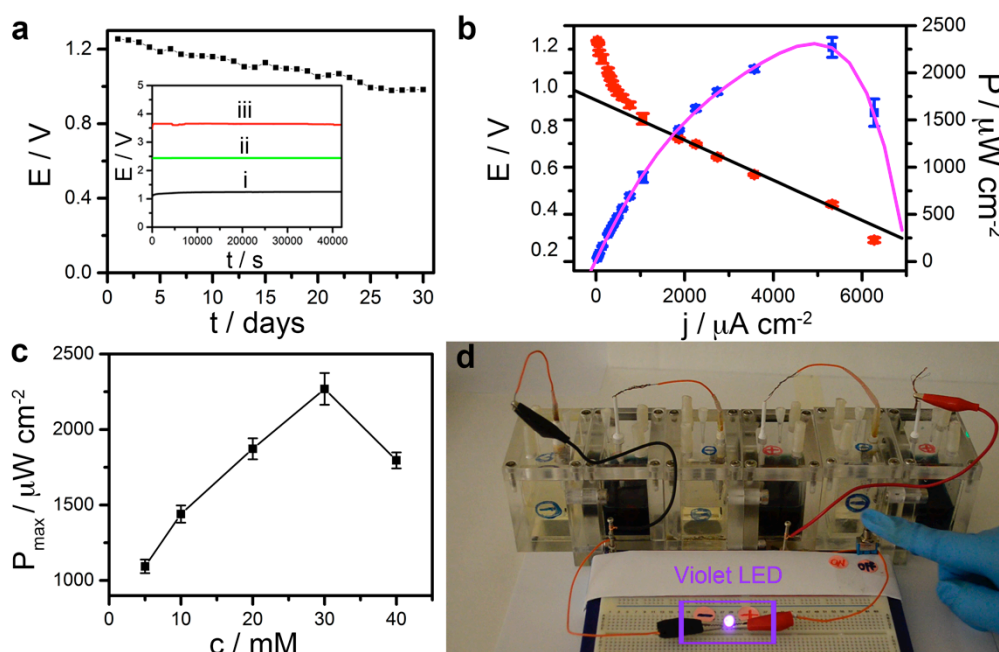


Figure 6-12: (a) The open circuit voltage from one cell over 30 days. Inset: the open circuit voltages from (i) single EBFC, (ii) double EBFCs, and (iii) triple EBFCs in series. (b) Polarization curve and power output curve of the EBFC. (c) The maximum power output of the EBFC with different glucose concentrations. (d) A violet LED powered by three EBFCs in series.

6.3 Conclusion

A novel glucose/O₂ powered EBFC equipped with a 3D graphene-SWCNT-GOD bioanode and a 3D graphene-SWCNT-laccase cathode is developed. Such EBFC is able to approach the theoretical limit of open circuit voltage (1.2 V) and a high power density ($2.27 \pm 0.11 \text{ mW cm}^{-2}$). The improved performance of the bio-power device is dependent on several factors. Firstly, the 3D graphene provides a large surface area for abundant enzyme loading and for catalytic reactions. Secondly, the nano-topographic surface and chemical handles provided by SWCNT networks ensures snug anchoring of enzyme molecules. Thirdly, an excellent electrical coupling between the enzymes and the electrodes for efficient direct electron transfer is achieved from an intimate interaction between the enzymes and the electrodes as well as the electron shuttling by

ABTS molecules at the cathode. Finally, the 3D multiplexed and continuous conduction networks offered by 3D graphene-SWCNT substrate ensure rapid charge transfer and conduction. This study demonstrates the synergistic integration between the two π -conjugated carbon allotropes (graphene and carbon nanotubes), and sets new performance boundaries for glucose-powered EBFC based bio-power devices.

This chapter (including phrases and figures) is adapted / reproduced with permission from our published journal article “Three-Dimensional Graphene-Carbon Nanotube Hybrid for High-Performance Enzymatic Biofuel Cells. ACS Applied Materials & Interfaces, 2014, 3387-3393. Copyright 2014, American Chemical Society”

Chapter 7

7. Conclusions and Outlook

7.1 Conclusions

Semiconducting polymer quantum dots and nanocomposite graphene emerge as a new class of π -conjugated carbon derivatives with immense potential for applications in biomedicine. This thesis focuses on developing novel π -conjugated carbon nanomaterials with customizable properties for diverse biomedical applications namely; fluorescent labeling/sensing, therapeutics and enzymatic biofuel cells (bio-power devices).

In brief, a new general strategy for synthesizing fluorescent polymer quantum dots from non-fluorescent conjugated semiconducting polymers (1D) was developed in this work. Using this strategy unique fluorescent polymer dots with customizable properties (optical, surface properties) were synthesized and utilized as tools for optical (*in vitro* cellular imaging and sensing) and therapeutic (antibacterial) applications. Finally a bio-power device was fabricated, wherein two π -conjugated nanocarbons (CNTs and graphene) work synergistically to enhance the performance of a biological power device. The fabricated biofuel cell was capable of generating power from physiological substances including glucose. The materials were well characterized and possessed unique physical, chemical, optical and electrochemical properties. Specifically;

1. A facile electropolymerization-ultrasonication based general strategy was developed to synthesize polymer dots with small sizes, high brightness, excellent photostability and superb biocompatibility. An easily modifiable route, the synthetic strategy demonstrated here can be easily adjusted (e.g., different polymer

precursors, ionic liquids, exfoliation solvents) to produce different types of polymer QDs with unique properties use in biomedical settings. The physicochemical and optical behaviors of the synthesized polymer dots were studied in detail. Further theoretical studies were performed to elucidate their PL mechanisms.

2. Using this strategy novel fluorescent polymer quantum dots derived from non-fluorescent 1D semiconducting polymer poly (3,4-ethylenedioxythiophene (PEDOT) were synthesized. The molecularly light and highly photo-stable PEDOT-Pdots were then demonstrated as promising fluorophores for bio-imaging (labeling the early endosomes) and sensitive optical sensors for detection of toxic Hg^{2+} ions with a detection limit of 0.87 μM (with $\text{S/N} = 3$) and the linear response upto 10 μM .
3. Practical applications like *in vitro* cellular imaging require the fluorophores to possess properties like high brightness, excellent photostability and biocompatibility. To this extent, a new type of thiophene based polymer dots with improved quantum yields were synthesized by modifying the previously developed strategy. The synthesized pTh-Pdots were small and highly biocompatible. The pTh-Pdots suspensions in an organic solvent Dimethylformamide (DMF) show significant promise for cellular imaging and tracking applications, even at low working concentrations (5-10 $\mu\text{g/ml}$). Interestingly the pTh-Pdots nanostructures show negative solvatochromism, and were utilized to label and differentiate early endosomes and lysosomes. Their ability to fluoresce different colors in the early endosomes and lysosomes highlights their promising ability to track the endocytic pathway in real time.

4. The pTh-Pdots possess unique surface properties enabling them to exhibit good therapeutic behavior. Subsequently, water suspensions of the pTh-Pdots were demonstrated as potent antibacterial agents. With low minimum inhibitory concentrations, these synthetic antibacterial alternatives showed good activity against both G(-) bacteria (*E. coli* - 45 µg/ml, *P. aeruginosa* -100 µg/ml)) and G(+) bacteria (*S. aureus* - 60 µg/ml), even drug resistant strains. Additionally, these pTh-Pdots demonstrated excellent peroxidase mimicking activity. The synergistic use of their intrinsic ability to disrupt bacterial membranes and mimic peroxidase resulted in a dramatic increase in their potency (MIC - 10 µg/ml) against both G(+) and G(-) strains.
5. Besides modulating their size and surface properties to generate high performance quantum dots, these π -conjugated nanocarbons intrinsically possess excellent properties that can be used to enhance electrode performances in bio-power devices. High performance bioelectrodes for a glucose/O₂ powered enzymatic biofuel cell (EBFC) were fabricated by producing composites between two π -conjugated carbon allotropes, 1D single-walled carbon nanotubes and CVD grown freestanding graphene (3D form of the 2D graphene). The novel 3D graphene-SWCNT-enzyme based bio-electrodes demonstrated a synergistic intergration between two conjugated carbon allotropes (carbon nanotubes and graphene), to push the EBFC performance to new limits. With a superb performance due to extensive electrochemically active surface areas, excellent anchoring of enzymes by SWCNTs, efficient direct electron transfer and superb conductivity, this EBFC approaches the theoretical limit of open circuit voltage (1.2 V) and a high power density ($2.27 \pm 0.11 \text{ mW cm}^{-2}$).
6. The different nanomaterials synthesized, their properties and performance have been summarized in Table 7-1.

| Nanomaterials Synthesized | Properties | Performance |
|---|--|---|
| Poly (3,4-ethylenedioxythiophene) derived polymer quantum dots (PEDOT-Pdots) | <ul style="list-style-type: none"> - Small Size - High Biocompatibility - Hg²⁺ specific sensing - Photoluminescence | <ul style="list-style-type: none"> - Photostability over 3h - Early endosome specific uptake - Optical sensitivity (0.87 μM, S/N = 3) |
| Poly(2,2'-bithiophene) derived polymer quantum dots (pTh-Pdots) | <ul style="list-style-type: none"> - Small Size - High Biocompatibility - Solvatochromic Photoluminescence - Amphiphilic - Peroxidase mimicking activity - Antibacterial activity | <ul style="list-style-type: none"> - DMF-suspended pTh-Pdots used as fluorophores at working concentrations. - Tracks the endocytic pathway over 6h – 24h. - Emits blue in early endosomes and green in lysosomes. - Possess antibacterial activity against <i>E. coli</i> (MIC - 45 μg/ml), <i>S. aureus</i> (MIC- 60 μg/ml) and <i>P. aeruginosa</i> (MIC-100 μg/ml) - Peroxidase mimicking behavior improves potency. Kills previously resistant <i>B. subtilis</i> (MIC-10 μg/ml). |
| -DMF suspended pTh-Pdots | | |
| -Water suspended pTh-Pdots | | |
| 3D graphene-SWCNT-enzyme Bioelectrodes | <ul style="list-style-type: none"> - Synergistic effect between SWCNTs and 3D graphene. - Increased active surface area - Improved direct electron transfer - Electrical connection between the enzyme centre and electrode - Improved enzyme loading | <ul style="list-style-type: none"> - Power density - 2.27 ± 0.11 mW cm⁻² - Open circuit voltage - ~ 1.2 V - Stability - $\sim 20\%$ loss over 1 month - Two EBFCs in series can light up a violet LED. - Produces more power than 10μW requirement of modern pacemaker.²⁴⁴ |

Table 7-1 –Nanomaterials synthesized, their properties and performance

7.2 Outlook

Although this thesis work has been dedicated to developing strategies to generate nanomaterials with customized physicochemical/surface properties from 1D and 2D π -conjugated carbons for biomedical applications, multiple challenges still exist before these materials can be used in clinical settings. Further research is required before these polymer dots and bio-electrodes can be used in clinical settings:

1. While a new strategy for the easy and facile synthesis of small sized polymer dots has been developed over the course of this thesis work, when taken together with the limited existing synthesis strategies as discussed in Chapter 2 still highlights the need for further development of uncomplicated synthesis strategies. Furthermore, while the yields reported in this work is high; it is still not viable on a commercial scale or large-scale production.
2. The as-prepared polymer dots in this thesis, fall within the short wavelength and are not very favorable for *in vivo* applications. It is known that the photoluminescence (PL) emission of the polymer dots is significantly controlled by the changes in its size and across the conjugated backbone including change in length, bending, kinking, inter/intrachain packing and so forth. Potential strategies are required to develop polymer dots with red-shifted PL emission for *in vivo* imaging applications. Some strategies for modulating the optical properties of the polymer dots would involve atomic substitution, addition of functional groups, and modification of the monomers themselves.²⁴⁵ For example, it has been demonstrated that surfactants (cationic, anionic etc.) can be used to control PL emission shifts in conjugated polymers.²⁴⁶ Simultaneous functionalization of desirable surfactants with the polymer during electrochemical polymerization may be used generate polymer dots with red-shifted emission. Selecting commercial monomers with band-gap for polymer dot synthesis may be another modulation strategy, wherein extending the conjugation lengths during synthesis may result in widened bang-gaps. Yet another strategy may involve the chemical tuning of the monomer followed by electropolymerization, then ultrasonication based synthesis.
3. Another disadvantage of the existing strategies are the difficulties in functionalization of the polymer dots, which usually involves complex chemical techniques or utilizing commercial pre-functionalized heavy polymers. While, the

current synthesis strategy allows for simultaneous functionalization during synthesis, it is however limited to moieties capable of forming π - π stacks with the polymer dots or functional groups already present on the polymeric backbone. The requirement for synthesis methods with quicker and easier functionalization routes still persists to an extent. Improved functionalization strategies are needed for the use of polymer dots as cellular imaging probes, optical sensors and antibacterial agents in clinical settings without compromising their high degrees of sensitivity and specificity. Simultaneous functionalization with anionic, cationic or other moieties may be one such approach.

4. As polymer dots are a relatively new generation of synthetic alternatives, further investigation regarding the utility of various polymer dots in diverse biomedical settings need to be conducted. It is clear over the course of this work that the quantum confinement of these polymer dots results them in showing promise for versatile applications in biomedical settings. Further investigations including extensive *in vivo* studies, investigating two-photon properties, developing application specific polymer dots such as photodynamic therapy agents, drug delivery vehicles, sensors, trackers and fluorophores are needed in order to realize their complete potential. Designing structures containing encapsulated conjugated polymer dots with photosensitizer dyes, anti-cancer drugs and so forth is one such strategy. Alternatively, selecting specific activity dependent monomer or co-functionalization of drug or sensitizer moiety to the polymer dot backbone are some other possible strategies.

The challenges and future development of bioelectrodes for enzymatic biofuel cells for clinical applications and commercialization are as follows:

5. Graphene-SWCNTs with their plethora of electrical, electrochemical, physical, and chemical properties are excellent hybrid electrodes. Furthermore, their high degree of biocompatibility makes them suitable for implantable medical devices (IMD). However, an important requirement for EBFC to be used in IMDs is miniaturization without adversely affecting the power output. Further research would be required to produce miniaturized bio-power devices with comparable performances. Extensive investigations are needed in order to reduce the size of the bioelectrodes while preserving their structural integrity, extensive active surface area and high power output. In that aspect, doping graphene with polymer nanoparticles, graphene quantum dots and other 0D structures may generate many interesting electrochemical properties such as high surface area, catalytic activity and small sizes.
6. A drawback with EBFCs is the use of enzymes as catalysts leads to enzyme degradation and storage issues over times. Additionally, surface fouling also results in electrode deterioration over time. However, a common bottleneck for non-enzymatic BFCs was the requirement of highly basic environments for glucose oxidation. This constraint has been overcome in the recent years, by fabricating composites such as metal oxides (cobalt oxide¹³¹)/ graphene hybrids capable of functioning in non-basic environments. Similarly, an enzymeless mesoporous silica/rGO/platinum²⁴⁷ based *in vivo* biofuel cell has also been developed. This becomes especially significant clinically since long-term implantable devices cannot be replaced repeatedly in short term and should be capable of functioning at physiological pH. Alternative catalyst materials including metal oxides, platinum nano-clusters/alloys, polymers nanoparticles, and polymer quantum dots should be composited with graphene and investigated in order to improve electrode performance such as electron transfer and mass diffusion.

Appendix I – Publications

- I. **Prasad, K. P.**; Than, A.; Li, N.; Sk, M. A.; Pu, K.; Zheng, X. T.; Chen, P., “Thiophene-Derived Polymer Dots for Imaging Endocytic Compartments in Live Cells and Broad-Spectrum Bacterium Killing.” *Materials Chemistry Frontiers.*, **2016**, DOI: 10.1039/c6qm00065g.
- II. **Prasad, K. P.**; Chen, Y.; Sk, M. A.; Than, A.; Wang, Y.; Sun, H. D.; Lim, K. H.; Dong, X. C.; Chen, P., “Fluorescent Quantum Dots Derived from PEDOT and their Applications in Optical Imaging and Sensing,” *Materials Horizons*, **2014**, 1 (5), 529-534.
- III. **Prasad, K. P.**; Chen, Y.; Chen, P., “Three-Dimensional Graphene-Carbon Nanotube Hybrid for High-Performance Enzymatic Biofuel Cells.” *ACS Applied Materials & Interfaces*, **2014**, 6 (5), 3387-3393.
- IV. Chen, Y.; **Prasad, K. P.**; Wang, X. W.; Pang, H. C.; Yan, R. Y.; Than, A.; Chan-Park, M. B.; Chen, P., “Enzymeless multi-sugar fuel cells with high power output based on 3D graphene-Co₃O₄ hybrid electrodes.” *Physical Chemistry Chemical Physics (PCCP)*, **2013**, 15 (23), 9170-9176.

Appendix II – Common Abbreviations

| Abbreviation | Expansion |
|---------------------|--|
| 0D | Zero Dimensional |
| 1D | One Dimensional |
| 2D | Two Dimensional |
| π | Pi |
| π - π | Pi-Pi |
| BMIMBF ₄ | 1-n-butyl-3-methylimidazolium tetrafluoroborate |
| DMF | Dimethylformamide |
| KDa | Kilodaltons |
| nm | Nanometer |
| pNPs | Polymer nanoparticles |
| Pdots | Polymer quantum dots/polymer dots |
| QD | Quantum dots |
| SWCNT | Single walled carbon nanotubes |
| Semi-QDs | Semiconductor quantum dots |
| THF | Tetrahydrofuran |

Appendix III – Table of Figures

| | |
|---|----|
| Figure 2-1: Schematic representation of various methods of preparation. Reproduced with permission from Reference ¹⁴ . Copyright 2013, The Royal Society of Chemistry. | 25 |
| Figure 2-2: Functionalization using (a) Co-precipitation, Adapted with permission from Reference ⁴⁹ . Copyright 2010, American Chemical Society (b) Click chemistry, Adapted with permission from Reference ⁵⁰ , Copyright 2010, Wiley-VCH (c) Direct Functionalization, Adapted with permission from Reference ⁵¹ , Copyright 2012, American Chemical Society | 27 |
| Figure 2-3: (a) TEM image of pNPs of poly (p-phenylene) prepared by microemulsion method and Pdots prepared from poly (fluorene) copolymer by nano-precipitation methods. Adapted with permission from Reference ^{26, 50, 53} , Copyright 2002, Wiley-VCH. Copyright 2010, Wiley-VCH. Copyright 2013, Wiley-VCH. (b) Multi-emission Pdots synthesized from different boron dipyrromethene (BODIPY) units, with (inset) showing absorption behavior - Confocal images of Pdots with MCF-7 cell. Adapted with permission from Reference ⁵⁴ , Copyright 2013, American Chemical Society. | 29 |
| Figure 2-4: Schematic of various biological applications using conjugated polymer dots and nanoparticles. Reproduced with permission from Reference ¹⁴ , Copyright 2013, The Royal Society of Chemistry. | 38 |
| Figure 2-5: Dual Colorimetric and Fluorescent Sensor Based On Semiconducting Polymer Dots for Ratiometric Detection of Lead Ions in Living Cells. Reprinted with permission from Reference ⁸² . Copyright 2015, American Chemical Society | 40 |
| Figure 2-6: Self assembled phosphorescent Pdots for dual applications of O ₂ sensing, and photodynamic therapy. Reproduced with permission from Reference ⁹¹ , Copyright 2016, Wiley-VCH..... | 42 |
| Figure 2-7: CNT based EBFC - At the anode, glucose is oxidized to gluconolactone, where the electrons are transferred from the GOX to CNT. Catalase decomposes hydrogen peroxide into oxygen and water. At the cathode, electrons are transferred from CNT to laccase where dioxygen is reduced to water. Reproduced with permission from Reference ¹⁰⁴ . Copyright 2011, Nature Publishing Group (NPG). | 46 |
| Figure 2-8: (a) Hydrothermal driven self-assembly of 3D graphene foam. Adapted with permission from Reference ¹²² . Copyright 2015, American Chemical Society. (b) 3D Graphene hydrogel formation in the presence of cross-linkers. Adapted with permission from Reference ¹²³ . Copyright 2014, One Central Press (OCP). | 52 |
| Figure 2-9: (a) Chemical vapor deposition grown macroporous 3D graphene on Nickel foam. Adapted by permission from Macmillan Publishers Ltd: Nature Materials Reference ¹¹⁷ , Copyright 2011, Nature Publishing Group (NPG). (b) Schematic for gold and copper template driven synthesis. Reproduced with permission from Reference ¹²⁶ . Copyright 2016, Published by The Royal Society of Chemistry. | 54 |
| Figure 2-10: 3D graphene-CO ₃ O ₄ based multi-sugar biofuel cell. Reproduced with permission of PCCP Owner Societies from Reference ¹³¹ , Copyright 2013, Royal Society of Chemistry..... | 57 |
| Figure 3-1: Schematic illustration for the preparation of PEDOT-Pdots. | 62 |

| | |
|---|----|
| Figure 3-2: QDs exfoliated from the fibrous electropolymerized PEDOT film are small and uniform in size. (a) FESEM image of the PEDOT. Inset shows the film surface with a higher-resolution. (b) AFM image of PEDOT-Pdots. Inset shows the height profile along the indicated line. (c) The height (thickness) of 152 individual QDs. The indicative horizontal lines are 0.21 nm apart. (d) HRTEM image of PEDOT-Pdots. The upper inset presents a single PEDOT-Pdot with resolved crystal lattices. The lower inset gives the FTT diffraction pattern. (e) Diameter distribution of 172 PEDOT-Pdots. (f) The gel electrophoresis of PEDOT-Pdots (1 - fluorescent image under UV; 2 – bright field image) and protein markers (3). | 64 |
| Figure 3-3: Spectroscopic characterizations. (a) XPS spectra of PEDOT film (black) and PEDOT-Pdots (red). (b) High-resolution C1s peak in XPS spectrum of PEDOT-Pdots. Inset shows N1s peak. (c) High-resolution S2p peak in XPS spectrum of PEDOT-Pdots. (d) Raman spectra of PEDOT film (black) and PEDOT-Pdots (red). (e) FTIR spectra of BMIMBF ₄ (black), PEDOT-Pdots (blue – in water; red – in DMF). (f) XRD Spectra of PEDOT Film (black) and PEDOT-Pdots (red). | 65 |
| Figure 3-4: Optical characteristics of PEDOT-Pdots. (a) UV-Vis adsorption spectrum of PEDOT-Pdots in water (black) and DMF (red). (b) And (c) PL spectra of Pdots in DMF and water with different excitation wavelengths. The insets show the images of the Pdot suspensions under UV. (d) The photobleaching behavior showing normalized fluorescence of the green Pdots (in DMF), blue Pdots (in water), and FITC under continuous confocal imaging. | 67 |
| Figure 3-5: Different isomers of EDOT trimer. The isomers vary by the dihedral angles [d1(S1C2C3S4) & d2(S4C5C6S7)]. The figures indicate the conformations of (a) Isomer 1 [d1 = 177.9° & d2 = 177.9°], (b) Isomer 2 [d1 = 178.2° & d2 = 42.5°], (c) Isomer 3 [d1 = 43.6° & d2 = 43.6°] | 69 |
| Figure 3-6: Photoluminescence excitation spectrum of blue PEDOT-Pdots suspended in water (emission at 450 nm) and green PEDOT-Pdots suspended in DMF (emission at 533 nm) | 70 |
| Figure 3-7: Schematic for electronic transitions of PEDOT-Pdots. | 70 |
| Figure 3-8: Photobleaching studies of the PEDOT-Pdots (blue and green) using a spectrofluorometer. The fluorescence intensities are normalized to the maximum. A LS-55 fluorescence spectrometer (PerkinElmer) using the inbuilt light source (Xenon lamp) is used. PEDOT-Pdots in either DMF or water (200 µg/mL) are added in a quartz cuvette for measurements. The fluorescence intensity over time is recorded continuously at 460 nm (for green QDs in DMF) or 360 nm (for blue QDs in water). | 71 |
| Figure 3-9: Two-photon characterization of PEDOT-Pdots in DMF: (a) Excitation intensity dependent PL spectra at an excitation wavelength of 800 nm, using a femtosecond amplified-pulsed laser with a repetition rate of 1000 Hz and pulse-width of 100 fs ¹⁵⁵ . (b) Log-log plot of the PL signals versus excitation intensity. The nearly quadratic excitation intensity dependence of the PL signals clearly demonstrates the two-photon excitation process ¹⁵⁶ (c) Photostability of the PEDOT-Pdots in a small droplet under two-photon excitation (800 nm), with a pumping intensity of 20.1 GW/cm ² . | 72 |
| Figure 3-10: Cell viability and proliferation assay of PC12 cells incubated with different concentrations of PEDOT-Pdots. | 72 |

| | |
|--|----|
| Figure 3-11: PL (excited at 488 nm) of PEDOT-Pdots in DMF (green curve) and in water (5% original dispersion in DMF is diluted in water) (red trace)..... | 73 |
| Figure 3-12: Confocal imaging of PC12 cells after 24 h incubation with blue (a) or green (b) PEDOT-Pdots. Confocal images with staining of QDs (column 1), endosome marker mRFP-Rab5 (column 2). Column 3 is the merged image of column 1 and 2. Column 4 shows the bright-field image of the cells. Scale bar = 5 μ m..... | 74 |
| Figure 3-13: Sensitive and selective optical detection of Hg^{2+} ions. (a) PL of PEDOT-Pdots (200 $\mu\text{g/mL}$ in water) is selectively quenched by Hg^{2+} (100 μM), but not other metal ions at the concentration (b) The PL emission spectra of PEDOT-Pdots with various concentrations of Hg^{2+} (c) The relative concentration-dependent fluorescence response of PEDOT-Pdots. Inset shows the linear response range. The error bars represent the standard deviation of the measurements from three different samples..... | 75 |
| Figure 3-14: AFM image of Hg^{2+} -induced PEDOT-Pdot aggregates. | 76 |
| Figure 4-1: Field-effect scanning electron microscopy (FESEM) of pTh films obtained after (a) 30 min, (b) 45 min and (b) 60 min electropolymerization of 2,2'-bithiophene monomers. Insets show the magnified views. | 82 |
| Figure 4-2: (a) High-resolution TEM image of pTh-Pdots. (b) Diameter distribution ($n = 200$). (c) AFM image of pTh-Pdots. Inset shows the height profile along the indicated line. (d) Height distribution ($n = 200$). | 83 |
| Figure 4-3: (a) Spectra of Fourier transform infrared spectroscopy (FTIR) for pTh-Pdots and BMIMBF ₄ . (b-d) High-resolution C1s (b), S2p (c), and N1s (d) X-ray photoelectron spectroscopy (XPS) spectra of pTh-Pdots..... | 84 |
| Figure 4-4: (a) UV-Vis spectra of pTh-Pdots in DMF and pTh-Pdots in water. Inset shows the optical images with UV illumination at 365 nm. (b) PL emission spectra of pTh-Pdots in DMF at different excitation wavelengths. (c) PL emission spectra of pTh-Pdots in water, (d) Photo-bleaching of FITC dye molecules and pTh-Pdots under confocal imaging. | 85 |
| Figure 4-5: PL excitation spectra of pTh-Pdots in DMF (emission at 530 nm) and pTh-Pdots in water (emission at 435 nm), respectively. Inset shows the brightfield images of pTh-Pdots in DMF and water, respectively..... | 86 |
| Figure 4-6: (a) PL intensity of pTh-Pdots suspended in solvents with varying polarity. (b) Linear relationship between PL emission peak and relative poarity. ¹⁷⁹ | 87 |
| Figure 4-7: (a) PL of pTh-Pdots in water, pTh-Pdots in DMF, and DMF suspension of pTh-Pdots (10%) diluted in water (90%). (b) PL of DMF suspension of pTh-Pdots (50%) diluted in water (50%). | 88 |
| Figure 4-8: MTT assay of HeLa cells after overnight incubation with pTh-Pdots at various concentrations..... | 88 |
| Figure 4-9: Confocal imaging of HeLa cells incubated with pTh-Pdots (water stock diluted in cell medium to 50 $\mu\text{g/ml}$) for 3 h, and co-localization study with lysosome marker (LysoTracker Red). | 89 |
| Figure 4-10: Confocal imaging of HeLa cells incubated with pTh-Pdots (DMF stock diluted in cell medium to 5 $\mu\text{g/ml}$) for 1 and 3 h, respectively. (a) Co-localization with early endosome marker | |

| | |
|--|-----|
| (mRFP-Rab5). (b) Co-localization with lysosome marker (LysoTracker Red). (c) Schematic for endocytosis uptake of pTh-Pdots. Scale bar = 10 μ m..... | 90 |
| Figure 4-11: Confocal imaging of HeLa cells incubated with pTh-Pdots (DMF stock diluted in cell medium to 5 μ g/ml) for 6 h and 24 h, and co-localization study with lysosome marker (LysoTracker Red). (Scale bar = 10 μ m)..... | 91 |
| Figure 4-12: (a) PL spectra of Pluronic F127 polymer and pTh-Pdots encapsulated by Pluronic F127, excited at 340 or 440 nm. (b) PL spectra of DPPC liposomes and liposomes incorporated with pTh-Pdots (originally stocked in DMF). (c) Confocal fluorescence image (left) and bright-field image (right) of a water droplet containing pTh-Pdots incorporated liposomes. The borderline between the droplet and the dry glass coverslip can be clearly seen in the bright-field image (bright line). In the fluorescence image, it is seen that liposomes are more concentrated at the edge. (Scale bar = 100 μ m)..... | 92 |
| Figure 5-1: Antibacterial activity of pTh-Pdots. (a) Viability test against G(+) and G(-) bacteria with 100 μ g/ml pTh-Pdots. (b) Dose dependent effect of pTh-Pdots against G(+) and G(-) bacteria. (c) Viability test of Ampicillin-resistant <i>E. coli</i> treated with ampicillin, kanamycin and pTh-Pdots (all at 100 μ g/ml). (d) MTT Assay of rat fibroblasts after overnight incubation with pTh-Pdots at various concentrations. | 98 |
| Figure 5-2: The influence of BMIMBF ₄ (0.5 mg/mL) to <i>E. coli</i> growth. The average and standard deviation are obtained from 3 independent experiments. | 99 |
| Figure 5-3: (a) Absorption spectra of the mixture of 10 μ g/ml pTh-Pdots, 0.25 mM H ₂ O ₂ and 0.6 mM 3,3',5,5'-Tetramethylbenzidine (TMB) with various reaction durations (0 – 30 min). TMB is a commonly used reporter for peroxidase activity (upon oxidation by hydroxyl radicals, it turns blue and increases absorbance at 650 nm). The photographs in the inset shows that TMB turns into blue in the presence of both H ₂ O ₂ and TMB (30-min reaction). (b) Absorbance (at 650 nm) of 0.6 mM TMB (as the indicator of peroxidase activity) at various reaction durations, in the presence of 0.25 mM H ₂ O ₂ , or 10 μ g/ml GQD + 0.25 mM H ₂ O ₂ , or 10 μ g/ml GQD + 0.25 mM H ₂ O ₂ | 100 |
| Figure 5-4: Viability Tests of <i>E. coli</i> (a) and <i>B. subtilis</i> (a) treated with H ₂ O ₂ at different concentrations with or without pTh-Pdots (10 μ g/mL). | 101 |
| Figure 5-5: Fluorescence images with Live/Dead dye staining (a) and FESEM images of <i>E. coli</i> cells (b) without (left column) or with (right column) incubation of pTh-Pdots (100 μ g) for 2 h. | 102 |
| Figure 6-1: (a) The engineering drawing of the biofuel cell. (b) A 3D view of the biofuel cell. Inset shows the schematic drawing of the electrode. (c) The optical image of the working biofuel cell. Inset shows the optical image of the electrode. | 108 |
| Figure 6-2: FESEM images of (a) bare 3D graphene and (b) 3D graphene-SWCNT hybrid. Each inset shows the surface of the skeleton at a large magnification. (c) Raman spectra of (i) 3D graphene, (ii) SWCNT and (iii) 3D graphene-SWCNT hybrid. (d) FTIR of SWCNT. Contact angle measurements of (e) 3D graphene and (f) 3D graphene-SWCNT hybrid. | 109 |
| Figure 6-3: (a) The open circuit potential of (i) the 3D graphene-GOD anode and (ii) 3D graphene-SWCNT-GOD anode in pH 5.0 electrolyte solution containing 30 mM glucose. (b) The CVs of (i) 3D graphene electrode, (ii) 3D graphene-GOD electrode, (iii) 3D graphene-SWCNT hybrid electrode and (iv) 3D graphene-SWCNT-GOD hybrid electrode in pH 5.0 electrolyte solution. (v) | |

| | |
|---|-----|
| 3D graphene-SWCNT-GOD hybrid electrode in pH 5.0 electrolyte solution containing 1 mM glucose..... | 110 |
| Figure 6-4: FESEM images of (a) 3D graphene-GOD electrode, (b) 3D graphene-SWCNT-GOD electrode, (c) 3D graphene-laccase electrode, and (d) 3D graphene-SWCNT-laccase electrode. Scale bar = 1 μm | 112 |
| Figure 6-5: (a) The CVs of the 3D graphene electrode in pH 5.0 electrolyte solution, (i) without glucose and (ii) containing 1 mM glucose; 3D graphene-SWCNT electrode in pH 5.0 electrolyte solution, (iii) without glucose and (iv) containing 1 mM glucose. (b) The CVs of 3D graphene-GOD electrode in pH 5.0 electrolyte solution, (i) without glucose and (ii) containing 1 mM glucose.. | 113 |
| Figure 6-6: (a) CVs of the 3D graphene-SWCNT-GOD hybrid electrode at different scan rates: (i) 1 mV s^{-1} , (ii) 5 mV s^{-1} , (iii) 10 mV s^{-1} , (iv) 20 mV s^{-1} , (v) 40 mV s^{-1} , (vi) 50 mV s^{-1} , (vii) 60 mV s^{-1} , (viii) 80 mV s^{-1} , and (ix) 100 mV s^{-1} . (b) Redox peak currents versus scan rates from 1 mV s^{-1} to 700 mV s^{-1} | 114 |
| Figure 6-7: CV of the 3D graphene-SWCNT-GOD electrode at the scan rate of 1 mV s^{-1} | 114 |
| Figure 6-8: (a) CVs of the 3D graphene-SWCNT-GOD electrode in electrolyte solution with different pH values of (i) 4.95, (ii) 6.14, (iii) 6.86, and (iv) 7.70 at the scan rate of 50 mV s^{-1} . (b) Formal potential (E^0) versus pH..... | 115 |
| Figure 6-9: (a) The open circuit potential (measured in pH 5.0 electrolyte solution saturated with O_2) of (i) 3D graphene-laccase cathode and (ii) 3D graphene-SWCNT-laccase cathode, and (iii) 3D graphene-SWCNT-laccase cathode (with 0.5 mM ABTS). (b) The CVs of (i) 3D graphene-laccase electrode (solution with saturated N_2), (ii) 3D graphene-SWCNT hybrid electrode (solution with saturated N_2), (iii) 3D graphene-SWCNT-laccase hybrid electrode (solution with saturated N_2), (iv) 3D graphene-SWCNT-laccase hybrid electrode (solution saturated with N_2 and containing 0.5 mM ABTS) and (v) 3D graphene-SWCNT-laccase hybrid electrode (solution saturated with O_2 and containing 0.5 mM ABTS). (c) Illustration of electron transfer pathways. | 116 |
| Figure 6-10: (a) CVs of the 3D graphene-SWCNT-laccase hybrid electrode at different scan rates: (i) 10 mV s^{-1} , (ii) 20 mV s^{-1} , (iii) 40 mV s^{-1} , (iv) 80 mV s^{-1} , (v) 100 mV s^{-1} , and (vi) 200 mV s^{-1} . (b) Redox peak currents versus scan rates from 20 mV s^{-1} to 500 mV s^{-1} | 117 |
| Figure 6-11: (a) The CVs of the 3D graphene electrode in pH 5.0 electrolyte solution, (i) saturated with N_2 and (ii) saturated with O_2 ; 3D graphene-SWCNT electrode in pH 5.0 electrolyte solution, (iii) saturated with N_2 and (iv) saturated with O_2 . (b) The CVs of 3D graphene-laccase electrode in pH 5.0 electrolyte solution, (i) saturated with N_2 and (ii) saturated with O_2 | 117 |
| Figure 6-12: (a) The open circuit voltage from one cell over 30 days. Inset: the open circuit voltages from (i) single EBFC, (ii) double EBFCs, and (iii) triple EBFCs in series. (b) Polarization curve and power output curve of the EBFC. (c) The maximum power output of the EBFC with different glucose concentrations. (d) A violet LED powered by three EBFCs in series..... | 120 |

REFERENCES

1. Siegel, R. L.; Miller, K. D.; Jemal, A., Cancer Statistics, 2015. *CA: A Cancer Journal For Clinicians* **2015**, 65 (1), 5-29.
2. Cha, C.; Shin, S. R.; Annabi, N.; Dokmeci, M. R.; Khademhosseini, A., Carbon-Based Nanomaterials: Multifunctional Materials For Biomedical Engineering. *Acs Nano* **2013**, 7 (4), 2891-7.
3. Chang, H. H.; Cohen, T.; Grad, Y. H.; Hanage, W. P.; O'brien, T. F.; Lipsitch, M., Origin And Proliferation Of Multiple-Drug Resistance In Bacterial Pathogens. *Microbiology And Molecular Biology Reviews* **2015**, 79 (1), 101-16.
4. Deharo, J. C.; Djiane, P., Pacemaker Longevity. Replacement Of The Device. *Annales De Cardiologie Et D'angiologie* **2005**, 54 (1), 26-31.
5. Medintz, I. L.; Uyeda, H. T.; Goldman, E. R.; Mattoussi, H., Quantum Dot Bioconjugates For Imaging, Labelling And Sensing. *Nature Materials* **2005**, 4 (6), 435-46.
6. Derfus, A. M.; Chan, W. C. W.; Bhatia, S. N., Probing The Cytotoxicity Of Semiconductor Quantum Dots. *Nano Letters* **2003**, 4 (1), 11-18.
7. Freeman, R.; Willner, I., Optical Molecular Sensing With Semiconductor Quantum Dots (Qds). *Chemical Society Reviews* **2012**, 41 (10), 4067-85.
8. Lou, Y.; Zhao, Y.; Chen, J.; Zhu, J.-J., Metal Ions Optical Sensing By Semiconductor Quantum Dots. *Journal Of Materials Chemistry C* **2014**, 2 (4), 595.
9. Ehrenfreund, P.; Foing, B. H., Fullerenes And Cosmic Carbon. *Science* **2010**, 329 (5996), 1159-1160.
10. Taghioskoui, M., Trends In Graphene Research. *Materials Today* **2009**, 12 (10), 34-37.
11. Singh, S. K.; Kulkarni, P. P.; Dash, D., Biomedical Applications Of Carbon-Based Nanomaterials. In *Bio-Nanotechnology*, Blackwell Publishing Ltd.: **2013**, Pp 443-463.
12. Eatemadi, A.; Daraee, H.; Karimkhanloo, H.; Kouhi, M.; Zarghami, N.; Akbarzadeh, A.; Abasi, M.; Hanifehpour, Y.; Joo, S. W., Carbon Nanotubes: Properties, Synthesis, Purification, And Medical Applications. *Nanoscale Research Letters* **2014**, 9.
13. Roth, S.; Carrol, R., Introduction. In *One-Dimensional Metals: Conjugated Polymers, Organic Crystals, Carbon Nanotubes And Graphene*, 3rd Edition Ed.; Roth, S.; Carrol, R., Eds. Wiley-Vch Verlag Gmbh & Co. Kgaa: Weinheim, Germany, **2013**; Chapter 1, Pp 1-18.
14. Feng, L.; Zhu, C.; Yuan, H.; Liu, L.; Lv, F.; Wang, S., Conjugated Polymer Nanoparticles: Preparation, Properties, Functionalization And Biological Applications. *Chemical Society Reviews* **2013**, 42 (16), 6620-33.
15. Heeger, A. J., Halbleitende Und Metallische Polymere: Polymere Materialien Der Vierten Generation (Nobel-Vortrag). *Angewandte Chemie* **2001**, 113 (14), 2660-2682.
16. Kim, J. H.; Park, K.; Nam, H. Y.; Lee, S.; Kim, K.; Kwon, I. C., Polymers For Bioimaging. *Progress In Polymer Science* **2007**, 32 (8-9), 1031-1053.

17. Vairavapandian, D.; Vichchulada, P.; Lay, M. D., Preparation And Modification Of Carbon Nanotubes: Review Of Recent Advances And Applications In Catalysis And Sensing. *Analytica Chimica Acta* **2008**, *626* (2), 119-129.
18. Holzinger, M.; Le Goff, A.; Cosnier, S., Carbon Nanotube/Enzyme Biofuel Cells. *Electrochimica Acta* **2012**, *82*, 179-190.
19. Liu, Y.; Dong, X.; Chen, P., Biological And Chemical Sensors Based On Graphene Materials. *Chemical Society Reviews* **2012**, *41* (6), 2283-307.
20. Huang, X.; Qi, X.; Boey, F.; Zhang, H., Graphene-Based Composites. *Chemical Society Reviews* **2012**, *41* (2), 666-86.
21. Liang, M. H.; Luo, B.; Zhi, L. J., Application Of Graphene And Graphene-Based Materials In Clean Energy-Related Devices. *International Journal Of Energy Research* **2009**, *33* (13), 1161-1170.
22. Bruchez, M.; Moronne, M.; Gin, P.; Weiss, S.; Alivisatos, A. P., Semiconductor Nanocrystals As Fluorescent Biological Labels. *Science* **1998**, *281* (5385), 2013-2016.
23. Deerinck, T. J., The Application Of Fluorescent Quantum Dots To Confocal, Multiphoton, And Electron Microscopic Imaging. *Toxicologic Pathology* **2008**, *36* (1), 112-6.
24. Wang, Y. C.; Hu, R.; Lin, G. M.; Roy, I.; Yong, K. T., Functionalized Quantum Dots For Biosensing And Bioimaging And Concerns On Toxicity. *ACS Applied Materials & Interfaces* **2013**, *5* (8), 2786-2799.
25. Valizadeh, A.; Mikaeili, H.; Samiei, M.; Farkhani, S. M.; Zarghami, N.; Kouhi, M.; Akbarzadeh, A.; Davaran, S., Quantum Dots: Synthesis, Bioapplications, And Toxicity. *Nanoscale Research Letters* **2012**, *7*.
26. Wu, C.; Chiu, D. T., Highly Fluorescent Semiconducting Polymer Dots For Biology And Medicine. *Angewandte Chemie International Edition* **2013**, *52* (11), 3086-109.
27. Zhu, S. J.; Song, Y. B.; Zhao, X. H.; Shao, J. R.; Zhang, J. H.; Yang, B., The Photoluminescence Mechanism In Carbon Dots (Graphene Quantum Dots, Carbon Nanodots, And Polymer Dots): Current State And Future Perspective. *Nano Research* **2015**, *8* (2), 355-381.
28. Burroughes, J. H.; Jones, C. A.; Friend, R. H., New Semiconductor Device Physics In Polymer Diodes And Transistors. *Nature* **1988**, *335* (6186), 137-141.
29. Pei, Q.; Yu, G.; Zhang, C.; Yang, Y.; Heeger, A. J., Polymer Light-Emitting Electrochemical Cells. *Science* **1995**, *269* (5227), 1086-1088.
30. Yu, G.; Gao, J.; Hummelen, J. C.; Wudl, F.; Heeger, A. J., Polymer Photovoltaic Cells: Enhanced Efficiencies Via A Network Of Internal Donor-Acceptor Heterojunctions. *Science* **1995**, *270* (5243), 1789-1791.
31. Zhu, C.; Liu, L.; Yang, Q.; Lv, F.; Wang, S., Water-Soluble Conjugated Polymers For Imaging, Diagnosis, And Therapy. *Chemical Reviews* **2012**, *112* (8), 4687-735.

32. Shen, J.; Zhu, Y.; Yang, X.; Li, C., Graphene Quantum Dots: Emergent Nanolights For Bioimaging, Sensors, Catalysis And Photovoltaic Devices. *Chemical Communications* **2012**, 48 (31), 3686-99.
33. Pecher, J.; Mecking, S., Nanoparticles Of Conjugated Polymers. *Chemical Reviews* **2010**, 110 (10), 6260-79.
34. Zrazhevskiy, P.; Sena, M.; Gao, X., Designing Multifunctional Quantum Dots For Bioimaging, Detection, And Drug Delivery. *Chemical Society Reviews* **2010**, 39 (11), 4326-4354.
35. Hittinger, E.; Kokil, A.; Weder, C., Synthesis And Characterization Of Cross-Linked Conjugated Polymer Milli-, Micro-, And Nanoparticles. *Angewandte Chemie* **2004**, 116 (14), 1844-1847.
36. Groenendaal, L. B., *Conductive Polymers, In Flexible Flat Panel Displays (Ed G. P. Crawford)*. John Wiley & Sons, Ltd: Chichester, UK., **2005**.
37. Zhou, M.; Heinze, J., Electropolymerization Of Pyrrole And Electrochemical Study Of Polypyrrole: 1. Evidence For Structural Diversity Of Polypyrrole. *Electrochimica Acta* **1999**, 44 (11), 1733-1748.
38. Krische, B.; Zagorska, M., Polythiophene Synthesis By Electropolymerization Of Thiophene And Bithiophene. *Synthetic Metals* **1989**, 33 (3), 257-267.
39. Szymanski, C.; Wu, C.; Hooper, J.; Salazar, M. A.; Perdomo, A.; Dukes, A.; McNeill, J., Single Molecule Nanoparticles Of The Conjugated Polymer MEH-PPV, Preparation And Characterization By Near-Field Scanning Optical Microscopy. *The Journal Of Physical Chemistry B* **2005**, 109 (18), 8543-8546.
40. Xing, C.; Xu, Q.; Tang, H.; Liu, L.; Wang, S., Conjugated Polymer/Porphyrin Complexes For Efficient Energy Transfer And Improving Light-Activated Antibacterial Activity. *Journal Of The American Chemical Society* **2009**, 131 (36), 13117-13124.
41. Moon, J. H.; Maclean, P.; Mcdaniel, W.; Hancock, L. F., Conjugated Polymer Nanoparticles For Biochemical Protein Kinase Assay. *Chemical Communications* **2007**, (46), 4910-4912.
42. Rahim, N. A. A.; Mcdaniel, W.; Bardon, K.; Srinivasan, S.; Vickerman, V.; So, P. T. C.; Moon, J. H., Conjugated Polymer Nanoparticles For Two-Photon Imaging Of Endothelial Cells In A Tissue Model. *Advanced Materials* **2009**, 21 (34), 3492-3496.
43. Moon, J. H.; Mendez, E.; Kim, Y.; Kaur, A., Conjugated Polymer Nanoparticles For Small Interfering RNA Delivery. *Chemical Communications* **2011**, 47 (29), 8370-8372.
44. Pu, K.-Y.; Li, K.; Shi, J.; Liu, B., Fluorescent Single-Molecular Core-Shell Nanospheres Of Hyperbranched Conjugated Polyelectrolyte For Live-Cell Imaging. *Chemistry Of Materials* **2009**, 21 (16), 3816-3822.
45. Wu, C.; Szymanski, C.; McNeill, J., Preparation And Encapsulation Of Highly Fluorescent Conjugated Polymer Nanoparticles. *Langmuir* **2006**, 22 (7), 2956-2960.

46. Howes, P.; Green, M.; Levitt, J.; Suhling, K.; Hughes, M., Phospholipid Encapsulated Semiconducting Polymer Nanoparticles: Their Use In Cell Imaging And Protein Attachment. *Journal Of The American Chemical Society* **2010**, *132* (11), 3989-3996.
47. Li, K.; Pan, J.; Feng, S.-S.; Wu, A. W.; Pu, K.-Y.; Liu, Y.; Liu, B., Generic Strategy Of Preparing Fluorescent Conjugated-Polymer-Loaded Poly(DL-Lactide-Co-Glycolide) Nanoparticles For Targeted Cell Imaging. *Advanced Functional Materials* **2009**, *19* (22), 3535-3542.
48. Wu, C.; Hansen, S. J.; Hou, Q.; Yu, J.; Zeigler, M.; Jin, Y.; Burnham, D. R.; Mcneill, J. D.; Olson, J. M.; Chiu, D. T., Design Of Highly Emissive Polymer Dot Bioconjugates For In Vivo Tumor Targeting. *Angewandte Chemie* **2011**, *123* (15), 3492-3496.
49. Wu, C.; Schneider, T.; Zeigler, M.; Yu, J.; Schiro, P. G.; Burnham, D. R.; Mcneill, J. D.; Chiu, D. T., Bioconjugation Of Ultrabright Semiconducting Polymer Dots For Specific Cellular Targeting. *Journal Of The American Chemical Society* **2010**, *132* (43), 15410-15417.
50. Wu, C.; Jin, Y.; Schneider, T.; Burnham, D. R.; Smith, P. B.; Chiu, D. T., Ultrabright And Bioorthogonal Labeling Of Cellular Targets Using Semiconducting Polymer Dots And Click Chemistry. *Angewandte Chemie International Edition In English* **2010**, *49* (49), 9436-40.
51. Zhang, X. J.; Yu, J. B.; Wu, C. F.; Jin, Y. H.; Rang, Y.; Ye, F. M.; Chiu, D. T., Importance Of Having Low-Density Functional Groups For Generating High-Performance Semiconducting Polymer Dots. *ACS Nano* **2012**, *6* (6), 5429-5439.
52. Yu, J.; Wu, C.; Zhang, X.; Ye, F.; Gallina, M. E.; Rong, Y.; Wu, I. C.; Sun, W.; Chan, Y.-H.; Chiu, D. T., Stable Functionalization Of Small Semiconducting Polymer Dots Via Covalent Cross-Linking And Their Application For Specific Cellular Imaging. *Advanced Materials* **2012**, *24* (26), 3498-3504.
53. Landfester, K.; Montenegro, R.; Scherf, U.; Guntner, R.; Asawapirom, U.; Patil, S.; Neher, D.; Kietzke, T., Semiconducting Polymer Nanospheres In Aqueous Dispersion Prepared By A Miniemulsion Process. *Advanced Materials* **2002**, *14* (9), 651-655.
54. Rong, Y.; Wu, C.; Yu, J.; Zhang, X.; Ye, F.; Zeigler, M.; Gallina, M. E.; Wu, I. C.; Zhang, Y.; Chan, Y.-H.; Sun, W.; Uvdal, K.; Chiu, D. T., Multicolor Fluorescent Semiconducting Polymer Dots With Narrow Emissions And High Brightness. *ACS Nano* **2013**, *7* (1), 376-384.
55. Howes, P.; Thorogate, R.; Green, M.; Jickells, S.; Daniel, B., Synthesis, Characterisation And Intracellular Imaging Of PEG Capped BEHP-PPV Nanospheres. *Chemical Communications (Cambridge, England)* **2009**, (18), 2490-2.
56. Chandler, D., Interfaces And The Driving Force Of Hydrophobic Assembly. *Nature* **2005**, *437* (7059), 640-7.
57. Kurokawa, N.; Yoshikawa, H.; Hirota, N.; Hyodo, K.; Masuhara, H., Size-Dependent Spectroscopic Properties And Thermochromic Behavior In Poly(Substituted Thiophene) Nanoparticles. *Chemphyschem : A European Journal Of Chemical Physics And Physical Chemistry* **2004**, *5* (10), 1609-15.

58. Wu, C. F.; McNeill, J., Swelling-Controlled Polymer Phase And Fluorescence Properties Of Polyfluorene Nanoparticles. *Langmuir* **2008**, *24* (11), 5855-5861.
59. Marie, E.; Rothe, R.; Antonietti, M.; Landfester, K., Synthesis Of Polyaniline Particles Via Inverse And Direct Miniemulsion. *Macromolecules* **2003**, *36* (11), 3967-3973.
60. Szymanski, C.; Wu, C. F.; Hooper, J.; Salazar, M. A.; Perdomo, A.; Dukes, A.; McNeill, J., Single Molecule Nanoparticles Of The Conjugated Polymer MEH-PPV, Preparation And Characterization By Near-Field Scanning Optical Microscopy. *The Journal Of Physical Chemistry B* **2005**, *109* (18), 8543-8546.
61. Rahim, N. A. A.; Mcdaniel, W.; Bardon, K.; Srinivasan, S.; Vickerman, V.; So, P. T. C.; Moon, J. H., Conjugated Polymer Nanoparticles For Two-Photon Imaging Of Endothelial Cells In A Tissue Model. *Advanced Materials* **2009**, *21* (34), 3492-+.
62. Fernando, L. P.; Kandel, P. K.; Yu, J.; McNeill, J.; Ackroyd, P. C.; Christensen, K. A., Mechanism Of Cellular Uptake Of Highly Fluorescent Conjugated Polymer Nanoparticles. *Biomacromolecules* **2010**, *11* (10), 2675-82.
63. Ye, F. M.; Wu, C. F.; Jin, Y. H.; Wang, M.; Chan, Y. H.; Yu, J. B.; Sun, W.; Hayden, S.; Chiu, D. T., A Compact And Highly Fluorescent Orange-Emitting Polymer Dot For Specific Subcellular Imaging. *Chemical Communications* **2012**, *48* (12), 1778-1780.
64. Wu, C.; Bull, B.; Szymanski, C.; Christensen, K.; McNeill, J., Multicolor Conjugated Polymer Dots For Biological Fluorescence Imaging. *ACS Nano* **2008**, *2* (11), 2415-2423.
65. Piok, T.; Gadermaier, C.; Wenzl, F. P.; Patil, S.; Montenegro, R.; Landfester, K.; Lanzani, G.; Cerullo, G.; Scherf, U.; List, E. J. W., The Photophysics Of Organic Semiconducting Nanospheres: A Comprehensive Study. *Chemical Physics Letters* **2004**, *389* (1-3), 7-13.
66. Eggeling, C.; Widengren, J.; Rigler, R.; Seidel, C. A. M., Photobleaching Of Fluorescent Dyes Under Conditions Used For Single-Molecule Detection: Evidence Of Two-Step Photolysis. *Analytical Chemistry* **1998**, *70* (13), 2651-2659.
67. Grey, J. K.; Kim, D. Y.; Norris, B. C.; Miller, W. L.; Barbara, P. F., Size-Dependent Spectroscopic Properties Of Conjugated Polymer Nanoparticles. *The Journal Of Physical Chemistry B* **2006**, *110* (51), 25568-25572.
68. Yao, J.; Larson, D. R.; Vishwasrao, H. D.; Zipfel, W. R.; Webb, W. W., Blinking And Nonradiant Dark Fraction Of Water-Soluble Quantum Dots In Aqueous Solution. *Proceedings Of The National Academy Of Sciences Of The United States Of America* **2005**, *102* (40), 14284-14289.
69. Clifton, S. N.; Beattie, D. A.; Mierczynska-Vasilev, A.; Acres, R. G.; Morgan, A. C.; Kee, T. W., Chemical Defects In The Highly Fluorescent Conjugated Polymer Dots. *Langmuir* **2010**, *26* (23), 17785-17789.
70. Guimard, N. K.; Gomez, N.; Schmidt, C. E., Conducting Polymers In Biomedical Engineering. *Progress In Polymer Science* **2007**, *32* (8-9), 876-921.

71. Moon, J. H.; Mcdaniel, W.; Maclean, P.; Hancock, L. F., Live-Cell-Permeable Poly(P-Phenylene Ethynylene). *Angewandte Chemie* **2007**, *46* (43), 8223-5.
72. Fernando, L. P.; Kandel, P. K.; Yu, J.; Mcneill, J.; Ackroyd, P. C.; Christensen, K. A., Mechanism Of Cellular Uptake Of Highly Fluorescent Conjugated Polymer Nanoparticles. *Biomacromolecules* **2010**, *11* (10), 2675-2682.
73. Kim, S.; Lim, C.-K.; Na, J.; Lee, Y.-D.; Kim, K.; Choi, K.; Leary, J. F.; Kwon, I. C., Conjugated Polymer Nanoparticles For Biomedical In Vivo Imaging. *Chemical Communications* **2010**, *46* (10), 1617-1619.
74. Choi, H. S.; Liu, W.; Misra, P.; Tanaka, E.; Zimmer, J. P.; Ipe, B. I.; Bawendi, M. G.; Frangioni, J. V., Renal Clearance Of Quantum Dots. *Nature Biotechnology* **2007**, *25* (10), 1165-1170.
75. Yu, J.; Wu, C.; Tian, Z.; Mcneill, J., Tracking Of Single Charge Carriers In A Conjugated Polymer Nanoparticle. *Nano Letters* **2012**, *12* (3), 1300-1306.
76. Yu, J.; Wu, C.; Sahu, S. P.; Fernando, L. P.; Szymanski, C.; Mcneill, J., Nanoscale 3D Tracking With Conjugated Polymer Nanoparticles. *Journal Of The American Chemical Society* **2009**, *131* (51), 18410-18414.
77. Heeger, P. S.; Heeger, A. J., Making Sense Of Polymer-Based Biosensors. *Proceedings Of The National Academy Of Sciences Of The United States Of America* **1999**, *96* (22), 12219-12221.
78. Wu, C.; Bull, B.; Christensen, K.; Mcneill, J., Ratiometric Single-Nanoparticle Oxygen Sensors For Biological Imaging. *Angewandte Chemie* **2009**, *121* (15), 2779-2783.
79. Chan, Y.-H.; Wu, C.; Ye, F.; Jin, Y.; Smith, P. B.; Chiu, D. T., Development Of Ultrabright Semiconducting Polymer Dots For Ratiometric Ph Sensing. *Analytical Chemistry* **2011**, *83* (4), 1448-1455.
80. Ye, F.; Wu, C.; Jin, Y.; Chan, Y.-H.; Zhang, X.; Chiu, D. T., Ratiometric Temperature Sensing With Semiconducting Polymer Dots. *Journal Of The American Chemical Society* **2011**, *133* (21), 8146-8149.
81. Harbron, E. J.; Davis, C. M.; Campbell, J. K.; Allred, R. M.; Kovary, M. T.; Economou, N. J., Photochromic Dye-Doped Conjugated Polymer Nanoparticles: Photomodulated Emission And Nanoenvironmental Characterization. *The Journal Of Physical Chemistry C* **2009**, *113* (31), 13707-13714.
82. Kuo, S. Y.; Li, H. H.; Wu, P. J.; Chen, C. P.; Huang, Y. C.; Chan, Y. H., Dual Colorimetric And Fluorescent Sensor Based On Semiconducting Polymer Dots For Ratiometric Detection Of Lead Ions In Living Cells. *Analytical Chemistry* **2015**, *87* (9), 4765-4771.
83. Polavarapu, L.; Perez-Juste, J.; Xu, Q. H.; Liz-Marzan, L. M., Optical Sensing Of Biological, Chemical And Ionic Species Through Aggregation Of Plasmonic Nanoparticles. *The Journal Of Physical Chemistry C* **2014**, *2* (36), 7460-7476.
84. Chan, Y.-H.; Jin, Y.; Wu, C.; Chiu, D. T., Copper(Ii) And Iron(Ii) Ion Sensing With Semiconducting Polymer Dots. *Chemical Communications* **2011**, *47* (10), 2820-2822.

85. Childress, E. S.; Roberts, C. A.; Sherwood, D. Y.; Leguyader, C. L. M.; Harbron, E. J., Ratiometric Fluorescence Detection Of Mercury Ions In Water By Conjugated Polymer Nanoparticles. *Analytical Chemistry* **2012**, *84* (3), 1235-1239.
86. Cordovilla, C.; Swager, T. M., Strain Release In Organic Photonic Nanoparticles For Protease Sensing. *Journal Of The American Chemical Society* **2012**, *134* (16), 6932-6935.
87. Feng, X.; Lv, F.; Liu, L.; Tang, H.; Xing, C.; Yang, Q.; Wang, S., Conjugated Polymer Nanoparticles For Drug Delivery And Imaging. *ACS Applied Materials & Interfaces* **2010**, *2* (8), 2429-2435.
88. Feng, X. L.; Tang, Y. L.; Duan, X. R.; Liu, L. B.; Wang, S., Lipid-Modified Conjugated Polymer Nanoparticles For Cell Imaging And Transfection. *Journal Of Materials Chemistry* **2010**, *20* (7), 1312-1316.
89. Li, S. Y.; Chang, K. W.; Sun, K.; Tang, Y.; Cui, N.; Wang, Y.; Qin, W. P.; Xu, H.; Wu, C. F., Amplified Singlet Oxygen Generation In Semiconductor Polymer Dots For Photodynamic Cancer Therapy. *ACS Applied Materials & Interfaces* **2016**, *8* (6), 3624-3634.
90. Zhang, Y. R.; Pang, L.; Ma, C.; Tu, Q.; Zhang, R.; Saeed, E.; Mahmoud, A.; Wang, J. Y., Small Molecule-Initiated Light-Activated Semiconducting Polymer Dots: An Integrated Nanoplatfrom For Targeted Photodynamic Therapy And Imaging Of Cancer Cells. *Analytical Chemistry* **2014**, *86* (6), 3092-3099.
91. Zhou, X. B.; Liang, H.; Jiang, P. F.; Zhang, K. Y.; Liu, S. J.; Yang, T. S.; Zhao, Q.; Yang, L. J.; Lv, W.; Yu, Q.; Huang, W., Multifunctional Phosphorescent Conjugated Polymer Dots For Hypoxia Imaging And Photodynamic Therapy Of Cancer Cells. *Advanced Science* **2016**, *3* (2).
92. Wu, C. F.; Zheng, Y. L.; Szymanski, C.; McNeill, J., Energy Transfer In A Nanoscale Multichromophoric System: Fluorescent Dye-Doped Conjugated Polymer Nanoparticles. *The Journal Of Physical Chemistry C* **2008**, *112* (6), 1772-1781.
93. Zhang, D.; Wu, M.; Zeng, Y. Y.; Liao, N. S.; Cai, Z. X.; Liu, G.; Liu, X. L.; Liu, J. F., Lipid Micelles Packaged With Semiconducting Polymer Dots As Simultaneous MRI/Photoacoustic Imaging And Photodynamic/Photothermal Dual-Modal Therapeutic Agents For Liver Cancer. *Journal Of Materials Chemistry B* **2016**, *4* (4), 589-599.
94. Hong, G.; Diao, S.; Antaris, A. L.; Dai, H., Carbon Nanomaterials For Biological Imaging And Nanomedicinal Therapy. *Chemical Reviews* **2015**, *115* (19), 10816-906.
95. Zhang, J.; Chen, H.; Zhou, T.; Wang, L.; Gao, D.; Zhang, X.; Liu, Y.; Wu, C.; Yuan, Z., A PIID-DTBT Based Semi-Conducting Polymer Dots With Broad And Strong Optical Absorption In The Visible-Light Region: Highly Effective Contrast Agents For Multiscale And Multi-Spectral Photoacoustic Imaging. *Nano Research* **2016**, 1-13.
96. Lyu, Y.; Fang, Y.; Miao, Q. Q.; Zhen, X.; Ding, D.; Fu, K. Y., Intraparticle Molecular Orbital Engineering Of Semiconducting Polymer Nanoparticles As Amplified Theranostics For In Vivo Photoacoustic Imaging And Photothermal Therapy. *ACS Nano* **2016**, *10* (4), 4472-4481.

97. Zhu, C.; Yang, Q.; Liu, L.; Lv, F.; Li, S.; Yang, G.; Wang, S., Multifunctional Cationic Poly(P-Phenylene Vinylene) Polyelectrolytes For Selective Recognition, Imaging, And Killing Of Bacteria Over Mammalian Cells. *Advanced Materials* **2011**, 23 (41), 4805-10.
98. Jain, A.; Duvvuri, L. S.; Farah, S.; Beyth, N.; Domb, A. J.; Khan, W., Antimicrobial Polymers. *Advanced Healthcare Materials* **2014**, 3 (12), 1969-85.
99. Piozzi, A.; Francolini, I., Editorial Of The Special Issue Antimicrobial Polymers. *International Journal of Molecular Sciences* **2013**, 14 (9), 18002-8.
100. Liang, F.; Chen, B., A Review On Biomedical Applications Of Single-Walled Carbon Nanotubes. *Current Medicinal Chemistry* **2010**, 17 (1), 10-24.
101. Falk, M.; Villarrubia, C. W. N.; Babanova, S.; Atanassov, P.; Shleev, S., Biofuel Cells For Biomedical Applications: Colonizing The Animal Kingdom. *Chemphyschem* **2013**, 14 (10), 2045-2058.
102. Qiu, H. J.; Guan, Y.; Luo, P.; Wang, Y., Recent Advance In Fabricating Monolithic 3D Porous Graphene And Their Applications In Biosensing And Biofuel Cells. *Biosensors & Bioelectronics* **2015**.
103. Yahiro, A. T.; Lee, S. M.; Kimble, D. O., Bioelectrochemistry .I. Enzyme Utilizing Bio-Fuel Cell Studies. *Biochimica et Biophysica Acta* **1964**, 88 (2), 375-&.
104. Zebda, A.; Gondran, C.; Le Goff, A.; Holzinger, M.; Cinquin, P.; Cosnier, S., Mediatorless High-Power Glucose Biofuel Cells Based On Compressed Carbon Nanotube-Enzyme Electrodes. *Nature Communications* **2011**, 2.
105. Falk, M.; Blum, Z.; Shleev, S., Direct Electron Transfer Based Enzymatic Fuel Cells. *Electrochimica Acta* **2012**, 82, 191-202.
106. Kwon, C. H.; Lee, S. H.; Choi, Y. B.; Lee, J. A.; Kim, S. H.; Kim, H. H.; Spinks, G. M.; Wallace, G. G.; Lima, M. D.; Kozlov, M. E.; Baughman, R. H.; Kim, S. J., High-Power Biofuel Cell Textiles From Woven Biscrolled Carbon Nanotube Yarns. *Nature Communications* **2014**, 5.
107. Gao, F.; Viry, L.; Maugey, M.; Poulin, P.; Mano, N., Engineering Hybrid Nanotube Wires For High-Power Biofuel Cells. *Nature Communications* **2010**, 1.
108. Kamitaka, Y.; Tsujimura, S.; Setoyama, N.; Kajino, T.; Kano, K., Fructose/Dioxygen Biofuel Cell Based On Direct Electron Transfer-Type Bioelectrocatalysis. *Physical Chemistry Chemical Physics: PCCP* **2007**, 9 (15), 1793-1801.
109. Novoselov, K. S.; Geim, A. K.; Morozov, S. V.; Jiang, D.; Zhang, Y.; Dubonos, S. V.; Grigorieva, I. V.; Firsov, A. A., Electric Field Effect In Atomically Thin Carbon Films. *Science* **2004**, 306 (5696), 666-669.
110. Feng, L.; Liu, Z., Graphene In Biomedicine: Opportunities And Challenges. *Nanomedicine* **2011**, 6 (2), 317-24.

111. Hou, J.; Shao, Y.; Ellis, M. W.; Moore, R. B.; Yi, B., Graphene-Based Electrochemical Energy Conversion And Storage: Fuel Cells, Supercapacitors And Lithium Ion Batteries. *Physical Chemistry Chemical Physics : PCCP* **2011**, *13* (34), 15384-402.
112. Han, T. H.; Lee, W. J.; Lee, D. H.; Kim, J. E.; Choi, E.-Y.; Kim, S. O., Peptide/Graphene Hybrid Assembly Into Core/Shell Nanowires. *Advanced Materials* **2010**, *22* (18), 2060-2064.
113. Qi, X.; Pu, K.-Y.; Li, H.; Zhou, X.; Wu, S.; Fan, Q.-L.; Liu, B.; Boey, F.; Huang, W.; Zhang, H., Amphiphilic Graphene Composites. *Angewandte Chemie International Edition* **2010**, *49* (49), 9426-9429.
114. Lu, C.-H.; Yang, H.-H.; Zhu, C.-L.; Chen, X.; Chen, G.-N., A Graphene Platform For Sensing Biomolecules. *Angewandte Chemie* **2009**, *121* (26), 4879-4881.
115. Cao, X. H.; Yin, Z. Y.; Zhang, H., Three-Dimensional Graphene Materials: Preparation, Structures And Application In Supercapacitors. *Energy & Environmental Science* **2014**, *7* (6), 1850-1865.
116. Zeng, M.; Wang, W.-L.; Bai, X.-D., Preparing Three-Dimensional Graphene Architectures: Review Of Recent Developments. *Chinese Physics B* **2013**, *22* (9), 098105.
117. Chen, Z. P.; Ren, W. C.; Gao, L. B.; Liu, B. L.; Pei, S. F.; Cheng, H. M., Three-Dimensional Flexible And Conductive Interconnected Graphene Networks Grown By Chemical Vapour Deposition. *Nature Materials* **2011**, *10* (6), 424-428.
118. Jiang, L.; Fan, Z., Design Of Advanced Porous Graphene Materials: From Graphene Nanomesh To 3D Architectures. *Nanoscale* **2014**, *6* (4), 1922-45.
119. Filip, J.; Tkac, J., Is Graphene Worth Using In Biofuel Cells? *Electrochimica Acta* **2014**, *136*, 340-354.
120. Xu, Y.; Sheng, K.; Li, C.; Shi, G., Self-Assembled Graphene Hydrogel Via A One-Step Hydrothermal Process. *ACS Nano* **2010**, *4* (7), 4324-4330.
121. Bi, H.; Yin, K.; Xie, X.; Zhou, Y.; Wan, N.; Xu, F.; Banhart, F.; Sun, L.; Ruoff, R. S., Low Temperature Casting Of Graphene With High Compressive Strength. *Advanced Materials* **2012**, *24* (37), 5124-5129.
122. Xu, Y. X.; Shi, G. Q.; Duan, X. F., Self-Assembled Three-Dimensional Graphene Macrostructures: Synthesis And Applications In Supercapacitors. *Accounts Of Chemical Research* **2015**, *48* (6), 1666-1675.
123. Żelechowska, K.; Kondratowicz, I.; Sadowski, W., 3D Porous Graphene-Based Structures – Synthesis And Applications. In *Carbon Nanotechnology*, Milne, W. I.; Cole, M., Eds. One Central Press (OCP): United Kingdom, **2014**; Chapter 9.
124. Dong, X.; Wang, P.; Fang, W.; Su, C.-Y.; Chen, Y.-H.; Li, L.-J.; Huang, W.; Chen, P., Growth Of Large-Sized Graphene Thin-Films By Liquid Precursor-Based Chemical Vapor Deposition Under Atmospheric Pressure. *Carbon* **2011**, *49* (11), 3672-3678.

125. Dong, X.; Wang, X.; Wang, L.; Song, H.; Zhang, H.; Huang, W.; Chen, P., 3D Graphene Foam As A Monolithic And Macroporous Carbon Electrode For Electrochemical Sensing. *ACS Applied Materials & Interfaces* **2012**, *4* (6), 3129-3133.
126. Tynan, M. K.; Johnson, D. W.; Dobson, B. P.; Coleman, K. S., Formation Of 3D Graphene Foams On Soft Templated Metal Monoliths. *Nanoscale* **2016**, *8* (27), 13303-10.
127. Zhao, Y.; Liu, J.; Hu, Y.; Cheng, H.; Hu, C.; Jiang, C.; Jiang, L.; Cao, A.; Qu, L., Highly Compression-Tolerant Supercapacitor Based On Polypyrrole-Mediated Graphene Foam Electrodes. *Advanced Materials* **2013**, *25* (4), 591-595.
128. Bacon, M.; Bradley, S. J.; Nann, T., Graphene Quantum Dots. *Particle & Particle Systems Characterization* **2014**, *31* (4), 415-428.
129. Zheng, X. T.; Ananthanarayanan, A.; Luo, K. Q.; Chen, P., Glowing Graphene Quantum Dots And Carbon Dots: Properties, Syntheses, And Biological Applications. *Small* **2015**, *11* (14), 1620-1636.
130. Jo, G.; Choe, M.; Lee, S.; Park, W.; Kahng, Y. H.; Lee, T., The Application Of Graphene As Electrodes In Electrical And Optical Devices. *Nanotechnology* **2012**, *23* (11).
131. Chen, Y.; Prasad, K. P.; Wang, X. W.; Pang, H. C.; Yan, R. Y.; Than, A.; Chan-Park, M. B.; Chen, P., Enzymeless Multi-Sugar Fuel Cells With High Power Output Based On 3D Graphene-Co₃O₄ Hybrid Electrodes. *Physical Chemistry Chemical Physics : PCCP* **2013**, *15* (23), 9170-9176.
132. Yong, Y. C.; Dong, X. C.; Chan-Park, M. B.; Song, H.; Chen, P., Macroporous And Monolithic Anode Based On Polyaniline Hybridized Three-Dimensional Graphene For High-Performance Microbial Fuel Cells. *ACS Nano* **2012**, *6* (3), 2394-2400.
133. Kumar, G. G.; Kirubakaran, C. J.; Udhayakumar, S.; Karthikeyan, C.; Nahm, K. S., Conductive Polymer/Graphene Supported Platinum Nanoparticles As Anode Catalysts For The Extended Power Generation Of Microbial Fuel Cells. *Industrial And Engineering Chemistry Research* **2014**, *53* (43), 16883-16893.
134. Liu, C.; Alwarappan, S.; Chen, Z. F.; Kong, X. X.; Li, C. Z., Membraneless Enzymatic Biofuel Cells Based On Graphene Nanosheets. *Biosensors & Bioelectronics* **2010**, *25* (7), 1829-1833.
135. Song, Y.; Chen, C.; Wang, C., Graphene/Enzyme-Encrusted Three-Dimensional Carbon Micropillar Arrays For Mediatorless Micro-Biofuel Cells. *Nanoscale* **2015**, *7* (16), 7084-90.
136. Campbell, A. S.; Jeong, Y. J.; Geier, S. M.; Koepsel, R. R.; Russell, A. J.; Islam, M. F., Membrane/Mediator-Free Rechargeable Enzymatic Biofuel Cell Utilizing Graphene/Single-Wall Carbon Nanotube Cogel Electrodes. *ACS Applied Materials & Interfaces* **2015**, *7* (7), 4056-4065.
137. Liu, J. Y.; Wang, T. S.; Wang, J.; Wang, E. K., Mussel-Inspired Biopolymer Modified 3D Graphene Foam For Enzyme Immobilization And High Performance Biosensor. *Electrochimica Acta* **2015**, *161*, 17-22.

138. Komathi, S.; Muthuchamy, N.; Lee, K. P.; Gopalan, A. I., Fabrication Of A Novel Dual Mode Cholesterol Biosensor Using Titanium Dioxide Nanowire Bridged 3D Graphene Nanostacks. *Biosensors & Bioelectronics* **2016**, *84*, 64-71.
139. Jang, H. D.; Kim, S. K.; Chang, H.; Jo, E. H.; Roh, K. M.; Choi, J. H.; Choi, J. W., Synthesis Of 3D Silver-Graphene-Titanium Dioxide Composite Via Aerosol Spray Pyrolysis For Sensitive Glucose Biosensor. *Aerosol Science And Technology* **2015**, *49* (7), 538-546.
140. Dong, X.; Ma, Y.; Zhu, G.; Huang, Y.; Wang, J.; Chan-Park, M. B.; Wang, L.; Huang, W.; Chen, P., Synthesis Of Graphene-Carbon Nanotube Hybrid Foam And Its Use As A Novel Three-Dimensional Electrode For Electrochemical Sensing. *Journal of Materials Chemistry* **2012**, *22* (33), 17044-17048.
141. Lovenich, W., PEDOT-Properties And Applications. *Polym Science Series C* **2014**, *56* (1), 135-143.
142. Chen, Y.; Gai, P. P.; Jin, L.; Zhu, D.; Tian, D. B.; Abdel-Halim, E. S.; Zhang, J. R.; Zhu, J. J., Fabrication Of PEDOT Nanowhiskers For Electrical Connection Of The Hemoglobin Active Center For H₂O₂ Electrochemical Biosensing. *Journal of Materials Chemistry B* **2013**, *1* (28), 3451-3457.
143. Martin, D. C.; Wu, J.; Shaw, C. M.; King, Z.; Spanninga, S. A.; Richardson-Burns, S.; Hendricks, J.; Yang, J., The Morphology Of Poly(3,4-Ethylenedioxythiophene). *Polymer Reviews* **2010**, *50* (3), 340-384.
144. Bhandari, S.; Deepa, M.; Singh, S.; Gupta, G.; Kant, R., Redox Behavior And Optical Response Of Nanostructured Poly(3,4-Ethylenedioxythiophene) Films Grown In A Camphorsulfonic Acid Based Micellar Solution. *Electrochimica Acta* **2008**, *53* (7), 3189-3199.
145. Yao, Y.; Liu, N.; McDowell, M. T.; Pasta, M.; Cui, Y., Improving The Cycling Stability Of Silicon Nanowire Anodes With Conducting Polymer Coatings. *Energy & Environmental Science* **2012**, *5* (7), 7927.
146. Kinoshita, K.; Matsunaga, N.; Hiraoka, M.; Yanagimoto, H.; Minami, H., Preparation Of Boron Nitride And Polystyrene/Boron Nitride Composite Particles By Dehydrogenation In Ionic Liquids. *RSC Advances* **2014**, *4* (17), 8605.
147. Kim, H. J.; Bae, I. S.; Cho, S. J.; Boo, J. H.; Lee, B. C.; Heo, J.; Chung, I.; Hong, B., Synthesis And Characteristics Of NH₂-Functionalized Polymer Films To Align And Immobilize DNA Molecules. *Nanoscale Research Letters* **2012**, *7*, 30.
148. Ananthanarayanan, A.; Wang, X.; Routh, P.; Sana, B.; Lim, S.; Kim, D.-H.; Lim, K.-H.; Li, J.; Chen, P., Facile Synthesis Of Graphene Quantum Dots From 3D Graphene And Their Application For Fe³⁺-Sensing. *Advanced Functional Materials* **2014**.
149. Zhang, X.; Chang, D.; Liu, J.; Luo, Y., Conducting Polymer Aerogels From Supercritical CO₂ Drying PEDOT-PSS Hydrogels. *Journal of Materials Chemistry* **2010**, *20* (24), 5080.

150. Sun, D.; Jin, L.; Chen, Y.; Zhang, J. R.; Zhu, J. J., Microwave-Assisted Insitu Synthesis Of Graphene/PEDOT Hybrid And Its Application In Supercapacitors. *Chempluschem* **2013**, 78 (3), 227-234.
151. Xie, N.; Luan, W., Ionic-Liquid-Induced Microfluidic Reaction For Water-Soluble Ce(1 - X)Tb(X)F₃ Nanocrystal Synthesis. *Nanotechnology* **2011**, 22 (26), 265609.
152. Armel, V.; Rivnay, J.; Malliaras, G.; Winther-Jensen, B., Unexpected Interaction Between PEDOT And Phosphonium Ionic Liquids. *Journal Of The American Chemical Society* **2013**, 135 (30), 11309-13.
153. Elschner, A.; Kirchmeyer, S.; Lovenich, W.; Merker, U.; K, R., *PEDOT : Principles And Applications Of An Intrinsically Conductive Polymer*. CRC Press: Boca Raton, FL, **2011**.
154. Dubowski, J. J.; Allen, C. N.; Fafard, S., Laser-Induced Inas/Gaas Quantum Dot Intermixing. *Applied Physics Letters* **2000**, 77 (22), 3583.
155. Zhang, H.; Liao, W. Q.; Chao, W.; Chen, Q. L.; Zeng, H. X.; Wu, C. P.; Wu, S. X.; Ho, H. I., Risk Factors For Sebaceous Gland Diseases And Their Relationship To Gastrointestinal Dysfunction In Han Adolescents. *The Journal of Dermatology* **2008**, 35 (9), 555-561.
156. Wang, Y.; Yang, X.; He, T. C.; Gao, Y.; Demir, H. V.; Sun, X. W.; Sun, H. D., Near resonant and nonresonant third-order optical nonlinearities of colloidal InP/ZnS quantum dots. *Applied Physics Letters* **2013**, 102 (2), 021917
157. Ran, X.; Sun, H.; Pu, F.; Ren, J.; Qu, X., Ag Nanoparticle-Decorated Graphene Quantum Dots For Label-Free, Rapid And Sensitive Detection Of Ag⁺ And Biothiols. *Chemical Communications* **2013**, 49 (11), 1079-1081.
158. Madhu, S.; Sharma, D. K.; Basu, S. K.; Jadhav, S.; Chowdhury, A.; Ravikanth, M., Sensing Hg(II) In Vitro And In Vivo Using A Benzimidazole Substituted BODIPY. *Inorganic Chemistry* **2013**, 52 (19), 11136-45.
159. Pal, A.; Bag, B., Hg(II) Ion Specific Dual Mode Signalling In A Thiophene Derivatized Rhodamine Based Probe And Their Complexation Cooperativity. *Journal Of Photochemistry And Photobiology A: Chemistry* **2012**, 240, 42-49.
160. Shigemoto, A. K.; Virca, C. N.; Underwood, S. J.; Shetterly, L. R.; McCormick, T. M., Thiophene-Based Fluorescent Mercury-Sensors. *Journal of Coordination Chemistry* **2016**, 69 (11-13), 2081-2089.
161. Tian, Z.; Yu, J.; Wu, C.; Szymanski, C.; Mcneill, J., Amplified Energy Transfer In Conjugated Polymer Nanoparticle Tags And Sensors. *Nanoscale* **2010**, 2 (10), 1999-2011.
162. Dmitriev, R. I.; Borisov, S. M.; Dussmann, H.; Sun, S.; Muller, B. J.; Prehn, J.; Baklaushev, V. P.; Klimant, I.; Papkovsky, D. B., Versatile Conjugated Polymer Nanoparticles For High-Resolution O₂ Imaging In Cells And 3D Tissue Models. *ACS Nano* **2015**, 9 (5), 5275-88.
163. Salzmann, S.; Kleinschmidt, M.; Tatchen, J.; Weinkauff, R.; Marian, C. M., Excited States Of Thiophene: Ring Opening As Deactivation Mechanism. *Physical Chemistry Chemical Physics : PCCP* **2008**, 10 (3), 380-392.

164. De Melo, J. S.; Pina, J.; Burrows, H. D.; Di Paolo, R. E.; Macanita, A. L., Electronic Spectral And Photophysical Properties Of Some P-Phenylenevinylene Oligomers In Solution And Thin Films. *Chemical Physics* **2006**, *330* (3), 449-456.
165. Mathiyazhakan, M.; Yang, Y. X.; Liu, Y. B.; Zhu, C. G.; Liu, Q.; Ohl, C. D.; Tam, K. C.; Gao, Y.; Xu, C. J., Non-Invasive Controlled Release From Gold Nanoparticle Integrated Photo-Responsive Liposomes Through Pulse Laser Induced Microbubble Cavitation. *Colloids And Surfaces B, Biointerfaces* **2015**, *126*, 569-574.
166. Pang, Y. H.; Li, X. Y.; Shi, G. Y.; Wang, F.; Jin, L. T., Electrochromic Properties Of Poly(3-Chlorothiophene) Film Electrodeposited On A Nanoporous Tio(2) Surface Via A Room Temperature Ionic Liquid And Its Application In An Electrochromic Device. *Thin Solid Films* **2008**, *516* (18), 6512-6516.
167. Liu, J. H.; Mikhailov, I. A.; Osaka, I.; Masunov, A. E.; Mccullough, R. D.; Zhai, L., Insight Into How Molecular Structures Of Thiophene-Based Conjugated Polymers Affect Crystallization Behaviors. *Polymer* **2011**, *52* (10), 2302-2309.
168. Adam, G.; Pivrikas, A.; Ramil, A. M.; Tadesse, S.; Yohannes, T.; Sariciftci, N. S.; Egbe, D. A. M., Mobility And Photovoltaic Performance Studies On Polymer Blends: Effects Of Side Chains Volume Fraction. *Journal Of Materials Chemistry* **2011**, *21* (8), 2594-2600.
169. Massoumi, B.; Alipour, N.; Fathalipour, S.; Jaymand, M., Nanostructured Poly(2,2 '-Bithiophene-Co-3,4-Ethylenedioxythiophene): Synthesis, Characterization, And Properties. *High Performance Polymers* **2015**, *27* (2), 161-170.
170. Cha, S.; Ao, M.; Sung, W.; Moon, B.; Ahlstrom, B.; Johansson, P.; Ouchi, Y.; Kim, D., Structures Of Ionic Liquid-Water Mixtures Investigated By IR And NMR Spectroscopy. *Physical Chemistry Chemical Physics : PCCP* **2014**, *16* (20), 9591-601.
171. Ratcliff, E. L.; Bakus, R. C.; Welch, G. C.; Van Der Poll, T. S.; Garcia, A.; Cowan, S. R.; Macleod, B. A.; Ginley, D. S.; Bazan, G. C.; Olson, D. C., Formation Of Interfacial Traps Upon Surface Protonation In Small Molecule Solution Processed Bulk Heterojunctions Probed By Photoelectron Spectroscopy. *Journal of Materials Chemistry C* **2013**, *1* (39), 6223-6234.
172. Kurmaev, E. Z.; Shamin, S. N.; Galakhov, V. R.; Moewes, A.; Otsuka, T.; Koizume, S.; Endo, K.; Katz, H. E.; Bach, M.; Neumann, M.; Ederer, D. L.; Iwami, M., Electronic Structure Of Thiophenes And Phtalocyanines. *Physical Review B* **2001**, *64* (4).
173. Kim, H. J.; Bae, I. S.; Cho, S. J.; Boo, J. H.; Lee, B. C.; Heo, J.; Chung, I.; Hong, B., Synthesis And Characteristics Of NH₂-Functionalized Polymer Films To Align And Immobilize DNA Molecules. *Nanoscale Research Letters* **2012**, *7*, 30.
174. Hoff, O.; Bahr, S.; Himmerlich, M.; Krischok, S.; Schaefer, J. A.; Kempter, V., Electronic Structure Of The Surface Of The Ionic Liquid [EMIM][Tf(2)N] Studied By Metastable Impact Electron Spectroscopy (MIES), UPS, And XPS. *Langmuir* **2006**, *22* (17), 7120-3.
175. Greaves, T. L.; Drummond, C. J., Ionic Liquids As Amphiphile Self-Assembly Media. *Chemical Society Reviews* **2008**, *37* (8), 1709-1726.

176. Wang, M. L.; Gao, Y. Q.; Zhang, J. J.; Zhao, J. W., Highly Dispersed Carbon Nanotube In New Ionic Liquid-Graphene Oxides Aqueous Dispersions For Ultrasensitive Dopamine Detection. *Electrochimica Acta* **2015**, *155*, 236-243.
177. Baheti, A.; Lee, C. P.; Thomas, K. R.; Ho, K. C., Pyrene-Based Organic Dyes With Thiophene Containing Pi-Linkers For Dye-Sensitized Solar Cells: Optical, Electrochemical And Theoretical Investigations. *Physical Chemistry Chemical Physics : PCCP* **2011**, *13* (38), 17210-21.
178. Salzmann, S.; Kleinschmidt, M.; Tatchen, J.; Weinkauff, R.; Marian, C. M., Excited States Of Thiophene: Ring Opening As Deactivation Mechanism. *Physical Chemistry Chemical Physics : PCCP* **2008**, *10* (3), 380-92.
179. Reichardt, C., Empirical Parameters Of Solvent Polarity. In *Solvents And Solvent Effects In Organic Chemistry*, Wiley-VCH Verlag Gmbh & Co. Kga: **2002**, Pp 389-469.
180. Leclerc, M.; Dufresne, G.; Blondin, P.; Bouchard, J.; Belletete, M.; Durocher, G., Molecular Design Of Chromic Functionalized Conjugated Polymers. *Synthetic Metals* **2001**, *119* (1-3), 45-48.
181. Katz, M.; Poulsen, B. J., Absorption Of Drugs Through The Skin. In *Concepts In Biochemical Pharmacology: Part I*, Brodie, B. B.; Gillette, J. R.; Ackerman, H. S., Eds. Springer Berlin Heidelberg: Berlin, Heidelberg, **1971**, Pp 103-174.
182. Levy, S. B.; Marshall, B., Antibacterial Resistance Worldwide: Causes, Challenges And Responses. *Nature Medicine* **2004**, *10* (12 Suppl), S122-9.
183. Hajipour, M. J.; Fromm, K. M.; Ashkarran, A. A.; Jimenez De Aberasturi, D.; De Larramendi, I. R.; Rojo, T.; Serpooshan, V.; Parak, W. J.; Mahmoudi, M., Antibacterial Properties Of Nanoparticles. *Trends In Biotechnology* **2012**, *30* (10), 499-511.
184. Li, P.; Poon, Y. F.; Li, W.; Zhu, H. Y.; Yeap, S. H.; Cao, Y.; Qi, X.; Zhou, C.; Lamrani, M.; Beuerman, R. W.; Kang, E. T.; Mu, Y.; Li, C. M.; Chang, M. W.; Leong, S. S.; Chan-Park, M. B., A Polycationic Antimicrobial And Biocompatible Hydrogel With Microbe Membrane Suctioning Ability. *Nature Materials* **2011**, *10* (2), 149-56.
185. Wang, Y.; Jett, S. D.; Crum, J.; Schanze, K. S.; Chi, E. Y.; Whitten, D. G., Understanding The Dark And Light-Enhanced Bactericidal Action Of Cationic Conjugated Polyelectrolytes And Oligomers. *Langmuir* **2013**, *29* (2), 781-92.
186. Chernousova, S.; Epple, M., Silver As Antibacterial Agent: Ion, Nanoparticle, And Metal. *Angewandte Chemie-International Edition* **2013**, *52* (6), 1636-53.
187. Cataldo, F., *Medicinal Chemistry And Pharmacological Potential Of Fullerenes And Carbon Nanotubes*. Springer: New York, **2008**.
188. Wang, X.; Liu, X.; Han, H., Evaluation Of Antibacterial Effects Of Carbon Nanomaterials Against Copper-Resistant *Ralstonia Solanacearum*. *Colloids And Surfaces. B, Biointerfaces* **2013**, *103*, 136-42.

189. Sun, H. J.; Gao, N.; Dong, K.; Ren, J. S.; Qu, X. G., Graphene Quantum Dots-Band-Aids Used For Wound Disinfection. *ACS Nano* **2014**, *8* (6), 6202-6210.
190. Wilson, R.; Kumar, P.; Parashar, V.; Vilch  ze, C.; Veyron-Churlet, R.; Freundlich, J. S.; Barnes, S. W.; Walker, J. R.; Szymonifka, M. J.; Marchiano, E.; Shenai, S.; Colangeli, R.; Jacobs Jr, W. R.; Neiditch, M. B.; Kremer, L.; Alland, D., Antituberculosis Thiophenes Define A Requirement For Pks13 In Mycolic Acid Biosynthesis. *Nature Chemical Biology* **2013**, *9* (8), 499-506.
191. Cerrada, M. L.; Munoz-Bonilla, A.; Fernandez-Garcia, M., Chapter 15: Future Perspectives And Concluding Remarks. In *Polymeric Materials With Antimicrobial Activity: From Synthesis To Applications*, The Royal Society Of Chemistry: **2014**, Pp 387-405.
192. Fischer, E. R.; Hansen, B. T.; Nair, V.; Hoyt, F. H.; Dorward, D. W., *Scanning Electron Microscopy*. 2012/05/03 Ed.; **2012**; Vol. Chapter 2, P Unit 2B 2.
193. Nikaido, H., Multidrug Resistance In Bacteria. *Annual Review of Biochemistry* **2009**, *78*, 119-146.
194. Collignon, P., Resistant Escherichia Coli-We Are What We Eat. *Clinical Infectious Diseases* **2009**, *49* (2), 202-204.
195. Li, N.; Than, A.; Wang, X.; Xu, S.; Sun, L.; Duan, H.; Xu, C.; Chen, P., Ultrasensitive Profiling Of Metabolites Using Tyramine-Functionalized Graphene Quantum Dots. *ACS Nano* **2016**, *10* (3), 3622-9.
196. Sun, H.; Zhao, A.; Gao, N.; Li, K.; Ren, J.; Qu, X., Deciphering A Nanocarbon-Based Artificial Peroxidase: Chemical Identification Of The Catalytically Active And Substrate-Binding Sites On Graphene Quantum Dots. *Angewandte Chemie* **2015**, *54* (24), 7176-80.
197. Liu, M.; Li, B. X.; Cui, X., Anionic Polythiophene Derivative As Peroxidase Mimetics And Their Application For Detection Of Hydrogen Peroxide And Glucose. *Talanta* **2013**, *115*, 837-841.
198. Maleki Dizaj, S.; Mennati, A.; Jafari, S.; Khezri, K.; Adibkia, K., Antimicrobial Activity Of Carbon-Based Nanoparticles. *Advanced Pharmaceutical Bulletin* **2015**, *5* (1), 19-23.
199. Moehlenbrock, M. J.; Minteer, S. D., Extended Lifetime Biofuel Cells. *Chem. Soc. Rev.* **2008**, *37* (6), 1188-1196.
200. Cooney, M. J.; Svoboda, V.; Lau, C.; Martin, G.; Minteer, S. D., Enzyme Catalysed Biofuel Cells. *Energy & Environmental Science* **2008**, *1* (3), 320-337.
201. Yang, X. Y.; Tian, G.; Jiang, N.; Su, B. L., Immobilization Technology: A Sustainable Solution For Biofuel Cell Design. *Energy & Environmental Science* **2012**, *5* (2), 5540-5563.
202. Schroder, U., From In Vitro To In Vivo-Biofuel Cells Are Maturing. *Angewandte Chemie-International Edition* **2012**, *51* (30), 7370-7372.
203. Yoshino, S.; Miyake, T.; Yamada, T.; Hata, K.; Nishizawa, M., Molecularly Ordered Bioelectrocatalytic Composite Inside A Film Of Aligned Carbon Nanotubes. *Advanced Energy Materials* **2013**, *3* (1), 60-64.

204. Jahan, M.; Bao, Q.; Yang, J.-X.; Loh, K. P., Structure-Directing Role Of Graphene In The Synthesis Of Metal–Organic Framework Nanowire. *Journal Of The American Chemical Society* **2010**, *132* (41), 14487-14495.
205. Vashist, S. K.; Zheng, D.; Al-Rubeaan, K.; Luong, J. H. T.; Sheu, F. S., Advances In Carbon Nanotube Based Electrochemical Sensors For Bioanalytical Applications. *Biotechnology Advances* **2011**, *29* (2), 169-188.
206. Nardecchia, S.; Carriazo, D.; Ferrer, M. L.; Gutierrez, M. C.; Del Monte, F., Three Dimensional Macroporous Architectures And Aerogels Built Of Carbon Nanotubes And/Or Graphene: Synthesis And Applications. *Chemical Society Reviews* **2013**, *42* (2), 794-830.
207. Yan, Z.; Ma, L. L.; Zhu, Y.; Lahiri, I.; Hahm, M. G.; Liu, Z.; Yang, S. B.; Xiang, C. S.; Lu, W.; Peng, Z. W.; Sun, Z. Z.; Kittrell, C.; Lou, J.; Choi, W. B.; Ajayan, P. M.; Tour, J. M., Three-Dimensional Metal-Graphene-Nanotube Multifunctional Hybrid Materials. *ACS Nano* **2013**, *7* (1), 58-64.
208. Maiyalagan, T.; Dong, X. C.; Chen, P.; Wang, X., Electrodeposited Pt On Three-Dimensional Interconnected Graphene As A Free-Standing Electrode For Fuel Cell Application. *Journal Of Materials Chemistry* **2012**, *22* (12), 5286-5290.
209. Xi, F. N.; Zhao, D. J.; Wang, X. W.; Chen, P., Non-Enzymatic Detection Of Hydrogen Peroxide Using A Functionalized Three-Dimensional Graphene Electrode. *Electrochemistry Communications* **2013**, *26*, 81-84.
210. Dong, X. C.; Cao, Y. F.; Wang, J.; Chan-Park, M. B.; Wang, L. H.; Huang, W.; Chen, P., Hybrid Structure Of Zinc Oxide Nanorods And Three Dimensional Graphene Foam For Supercapacitor And Electrochemical Sensor Applications. *RSC Advances* **2012**, *2* (10), 4364-4369.
211. Zhao, M. Q.; Liu, X. F.; Zhang, Q.; Tian, G. L.; Huang, J. Q.; Zhu, W. C.; Wei, F., Graphene/Single-Walled Carbon Nanotube Hybrids: One-Step Catalytic Growth And Applications For High-Rate Li-S Batteries. *ACS Nano* **2012**, *6* (12), 10759-10769.
212. Lu, L. H.; Liu, J. H.; Hu, Y.; Zhang, Y. W.; Randriamahazaka, H.; Chen, W., Highly Stable Air Working Bimorph Actuator Based On A Graphene Nanosheet/Carbon Nanotube Hybrid Electrode. *Advanced Materials* **2012**, *24* (31), 4317-4321.
213. Zhang, D. S.; Yan, T. T.; Shi, L. Y.; Peng, Z.; Wen, X. R.; Zhang, J. P., Enhanced Capacitive Deionization Performance Of Graphene/Carbon Nanotube Composites. *Journal Of Materials Chemistry* **2012**, *22* (29), 14696-14704.
214. Harris, D. C., *Quantitative Chemical Analysis, 8th Ed*, W. H. Freeman And Company, New York, 2010, P. 298.
215. Shan, C. S.; Yang, H. F.; Song, J. F.; Han, D. X.; Ivaska, A.; Niu, L., Direct Electrochemistry Of Glucose Oxidase And Biosensing For Glucose Based On Graphene. *Analytical Chemistry* **2009**, *81* (6), 2378-2382.

216. Bao, S. J.; Li, C. M.; Zang, J. F.; Cui, X. Q.; Qiao, Y.; Guo, J., New Nanostructured Tio₂ For Direct Electrochemistry And Glucose Sensor Applications. *Advanced Functional Materials* **2008**, *18* (4), 591-599.
217. Guo, C. X.; Hu, F. P.; Lou, X. W.; Li, C. M., High-Performance Biofuel Cell Made With Hydrophilic Ordered Mesoporous Carbon As Electrode Material. *Journal Of Power Sources* **2010**, *195* (13), 4090-4097.
218. Goran, J. M.; Mantilla, S. M.; Stevenson, K. J., Influence Of Surface Adsorption On The Interfacial Electron Transfer Of Flavin Adenine Dinucleotide And Glucose Oxidase At Carbon Nanotube And Nitrogen-Doped Carbon Nanotube Electrodes. *Analytical Chemistry* **2013**, *85* (3), 1571-81.
219. Wang, Z. Y.; Liu, S. N.; Wu, P.; Cai, C. X., Detection Of Glucose Based On Direct Electron Transfer Reaction Of Glucose Oxidase Immobilized On Highly Ordered Polyaniline Nanotubes. *Analytical Chemistry* **2009**, *81* (4), 1638-1645.
220. Wen, D.; Xu, X. L.; Dong, S. J., A Single-Walled Carbon Nanohorn-Based Miniature Glucose/Air Biofuel Cell For Harvesting Energy From Soft Drinks. *Energy & Environmental Science* **2011**, *4* (4), 1358-1363.
221. Li, X. C.; Zhou, H. J.; Yu, P.; Su, L.; Ohsaka, T.; Mao, L. Q., A Miniature Glucose/O₂ Biofuel Cell With Single-Walled Carbon Nanotubes-Modified Carbon Fiber Microelectrodes As The Substrate. *Electrochemistry Communications* **2008**, *10* (6), 851-854.
222. Yan, Y. M.; Yehezkeli, O.; Willner, I., Integrated, Electrically Contacted NAD(P)(+)-Dependent Enzyme - Carbon Nanotube Electrodes For Biosensors And Biofuel Cell Applications. *Chemistry –A European Journal* **2007**, *13* (36), 10168-10175.
223. Laviron, E., Use Of Linear Potential Sweep Voltammetry And Of Ac Voltammetry For The Study Of The Surface Electrochemical Reaction Of Strongly Adsorbed Systems And Of Redox Modified Electrodes. *Journal Of Electroanalytical Chemistry* **1979**, *100* (1-2), 263-270.
224. Laviron, E., General Expression Of The Linear Potential Sweep Voltammogram In The Case Of Diffusionless Electrochemical Systems. *Journal Of Electroanalytical Chemistry* **1979**, *101* (1), 19-28.
225. Liu, S. Q.; Ju, H. X., Reagentless Glucose Biosensor Based On Direct Electron Transfer Of Glucose Oxidase Immobilized On Colloidal Gold Modified Carbon Paste Electrode. *Biosensors & Bioelectronics* **2003**, *19* (3), 177-183.
226. Kang, X. H.; Wang, J.; Wu, H.; Aksay, I. A.; Liu, J.; Lin, Y. H., Glucose Oxidase-Graphene-Chitosan Modified Electrode For Direct Electrochemistry And Glucose Sensing. *Biosensors & Bioelectronics* **2009**, *25* (4), 901-905.
227. Cai, C. X.; Chen, J., Direct Electron Transfer Of Glucose Oxidase Promoted By Carbon Nanotubes. *Analytical Biochemistry* **2004**, *332* (1), 75-83.

228. Deng, C. Y.; Chen, J. H.; Chen, X. L.; Mao, C. H.; Nie, L. H.; Yao, S. Z., Direct Electrochemistry Of Glucose Oxidase And Biosensing For Glucose Based On Boron-Doped Carbon Nanotubes Modified Electrode. *Biosensors & Bioelectronics* **2008**, *23* (8), 1272-1277.
229. Liu, X. Q.; Shi, L. H.; Niu, W. X.; Li, H. J.; Xu, G. B., Amperometric Glucose Biosensor Based On Single-Walled Carbon Nanohorns. *Biosensors & Bioelectronics* **2008**, *23* (12), 1887-1890.
230. Rusling, J. F.; Wang, B.; Yun, S.-E., Electrochemistry Of Redox Enzymes. In *Bioelectrochemistry*, John Wiley & Sons, Ltd: **2008**, Pp 39-85.
231. Razmi, H.; Mohammad-Rezaei, R., Graphene Quantum Dots As A New Substrate For Immobilization And Direct Electrochemistry Of Glucose Oxidase: Application To Sensitive Glucose Determination. *Biosensors & Bioelectronics* **2013**, *41*, 498-504.
232. Yang, Z.; Ren, Y.; Zhang, Y.; Li, J.; Li, H.; Hu, X. H.; Xu, Q., Nanoflake-Like SnS₂ Matrix For Glucose Biosensing Based On Direct Electrochemistry Of Glucose Oxidase. *Biosensors & Bioelectronics* **2011**, *26* (11), 4337-41.
233. Frascioni, M.; Boer, H.; Koivula, A.; Mazzei, F., Electrochemical Evaluation Of Electron Transfer Kinetics Of High And Low Redox Potential Laccases On Gold Electrode Surface. *Electrochimica Acta* **2010**, *56* (2), 817-827.
234. Ivnitski, D. M.; Khripin, C.; Luckarift, H. R.; Johnson, G. R.; Atanasov, P., Surface Characterization And Direct Bioelectrocatalysis Of Multicopper Oxidases. *Electrochimica Acta* **2010**, *55* (24), 7385-7393.
235. Klis, M.; Karbarz, M.; Stojek, Z.; Rogalski, J.; Bilewicz, R., Thermoresponsive Poly(N-Isopropylacrylamide) Gel For Immobilization Of Laccase On Indium Tin Oxide Electrodes. *Journal Of Physical Chemistry B* **2009**, *113* (17), 6062-6067.
236. Liu, Y.; Wang, M. K.; Zhao, F.; Liu, B. F.; Dong, S. J., A Low-Cost Biofuel Cell With Ph-Dependent Power Output Based On Porous Carbon As Matrix. *Chemistry - A European Journal* **2005**, *11* (17), 4970-4974.
237. Liu, Y.; Dong, S. J., A Biofuel Cell With Enhanced Power Output By Grape Juice. *Electrochemistry Communications* **2007**, *9* (7), 1423-1427.
238. Szamocki, R.; Flexer, V.; Levin, L.; Forchiasin, F.; Calvo, E. J., Oxygen Cathode Based On A Layer-By-Layer Self-Assembled Laccase And Osmium Redox Mediator. *Electrochimica Acta* **2009**, *54* (7), 1970-1977.
239. Pita, M.; Gutierrez-Sanchez, C.; Olea, D.; Velez, M.; Garcia-Diego, C.; Shleev, S.; Fernandez, V. M.; De Lacey, A. L., High Redox Potential Cathode Based On Laccase Covalently Attached To Gold Electrode. *The Journal Of Physical Chemistry C* **2011**, *115* (27), 13420-13428.
240. Lau, C.; Adkins, E. R.; Ramasamy, R. P.; Luckarift, H. R.; Johnson, G. R.; Atanasov, P., Design Of Carbon Nanotube-Based Gas-Diffusion Cathode For O₂ Reduction By Multicopper Oxidases. *Advanced Energy Materials* **2012**, *2* (1), 162-168.

241. Brunel, L.; Denele, J.; Servat, K.; Kokoh, K. B.; Jolival, C.; Innocent, C.; Cretin, M.; Rolland, M.; Tingry, S., Oxygen Transport Through Laccase Biocathodes For A Membrane-Less Glucose/O₂ Biofuel Cell. *Electrochemistry Communications* **2007**, *9* (2), 331-336.
242. Barton, S. C.; Gallaway, J.; Atanasov, P., Enzymatic Biofuel Cells For Implantable And Microscale Devices. *Chemical Reviews* **2004**, *104* (10), 4867-4886.
243. Sakai, H.; Nakagawa, T.; Tokita, Y.; Hatazawa, T.; Ikeda, T.; Tsujimura, S.; Kano, K., A High-Power Glucose/Oxygen Biofuel Cell Operating Under Quiescent Conditions. *Energy & Environmental Science* **2009**, *2* (1), 133-138.
244. Patel, P., The Pulse Of Pacemakers. *Scientific American* **2015**, *312* (1), 14-14.
245. Chung, K.; Mcallister, A.; Bilby, D.; Kim, B. G.; Kwon, M. S.; Kioupakis, E.; Kim, J., Designing Interchain And Intrachain Properties Of Conjugated Polymers For Latent Optical Information Encoding. *Chemical Science* **2015**, *6* (12), 6980-6985.
246. Alizadeh, N.; Akbarinejad, A.; Ghoorchian, A., Photophysical Diversity Of Water-Soluble Fluorescent Conjugated Polymers Induced By Surfactant Stabilizers For Rapid And Highly Selective Determination Of 2,4,6-Trinitrotoluene Traces. *ACS Applied Materials & Interfaces* **2016**, *8* (37), 24901-8.
247. Sharma, T.; Hu, Y.; Stoller, M.; Feldman, M.; Ruoff, R. S.; Ferrari, M.; Zhang, X. J., Mesoporous Silica As A Membrane For Ultra-Thin Implantable Direct Glucose Fuel Cells. *Lab On A Chip* **2011**, *11* (14), 2460-2465.